UNIVERSITY OF COPENHAGEN
FACULTY OF SCIENCE

PhD Thesis

FUSION-BASED QUANTUM PHOTONICS WITH QUANTUM EMITTERS

Carlos F. D. Faurby

December 2024

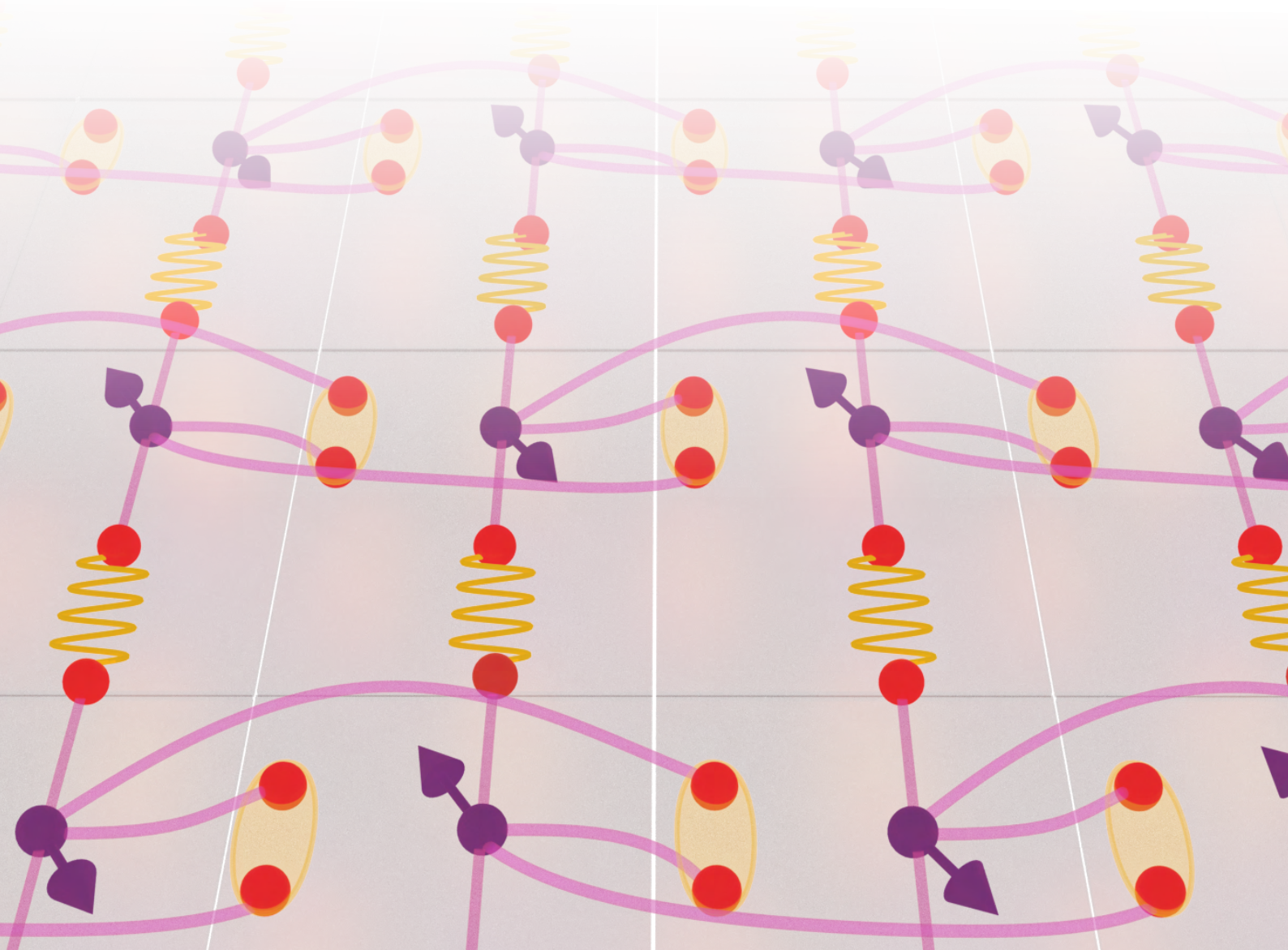

FUSION-BASED QUANTUM COMPUTING WITH QUANTUM EMITTERS AND PHOTONIC INTEGRATED CIRCUITS

Author	Carlos F. Duarte Faurby
Advisor	Prof. Peter Lodahl
Advisor	Assoc. Prof. Stefano Paesani

UNIVERSITY OF COPENHAGEN

Quantum Photonics
Center for Hybrid Quantum Networks (Hy-Q)
The Niels Bohr institute

This thesis has been submitted to
The PhD School of The Faculty of Science
University of Copenhagen
December 2024

Abstract

Photonic quantum computers have the unique potential to directly integrate a rapidly emerging technological platform: photonic microchips, with very promising qubit candidates: single photons. The fundamental lack of photon-photon interactions presents a challenge in practical implementations, but recent theoretical frameworks present a workaround, where the need of entangling operations is replaced by conducting single- and multi-photon measurements on already-entangled qubits. Fusion-based quantum computing is one such theoretical framework, which is of special interest due to its affordable hardware requirements.

This thesis presents four proof-of-principle experiments in quantum information processing, three of which present essential steps towards fusion-based quantum computing using quantum emitters and photonic integrated circuits.

We perform a first demonstration of a time-like fusion operation between two deterministically generated resource states. We employ a quantum dot emitter which through its spin generates entangled single photons. The photons are entangled to the quantum dot spin at different instances in time, and the fusion operation results in entanglement of the spin with itself at a different time. Our experiment suggests symmetry between space and time in fusion networks, and opens the possibility to new hardware-efficient architectures.

We proceed to showing the interface between single photons from a quantum dot and photonic integrated circuits (PICs). We demonstrate that single- and multi-photon operations can be performed on a microchip made of silicon nitride, a material platform suitable for large scale fabrication. We find that photonic indistinguishability is one of the main limiting factors in the fidelity of on-chip fusion operations.

We address this limitation by experimentally demonstrating that highly indistinguishable photons can be obtained through quantum interference between multiple photons and heralded detection on a subset of them. We call this phenomenon indistinguishability purification, and we find that its efficacy is independent on the distinguishability-inducing error source.

Finally we employ a large reprogrammable silicon PIC to successfully implement a method to replicate the ground state dynamics of different interacting spin systems. This task is hard to perform efficiently with classical algorithms, showing the power of quantum emitters and photonic integrated circuits for analog quantum simulation, suggesting that the technologies presented in this thesis also may have immediate applications.

Sammenfatning

Fotoniske kvantecomputere har en unik mulighed for direkte at integrere en fremstormende platform: "Fotoniske mikrochips", med meget lovende qubit-kandidater: "Enkelte fotoner". Den fundamentale mangel på foton-foton-interaktioner udgør en udfordring for praktiske implementeringer, men nye teoretiske udgangspunkter tilbyder en løsning, hvor behovet for entanglement-operationer erstattes af at udføre enkelt- og flerfotonmålinger på allerede entangled qubits. Fusionsbaseret kvantecomputering er et sådant teoretisk udgangspunkt, der er særligt interessant på grund af dets overkommelige hardwarekrav.

Denne afhandling præsenterer fire proof-of-principle-eksperimenter, der udgør væsentlige skridt mod Fusionsbaseret kvantecomputering, hvor enkeltfotoner produceret af kvanteudsendere og fotonisk integrerede kredsløb indlejret i mikrochips spiller en central rolle.

Vi udfører den første demonstration af en tidslignende fusionsoperation mellem to deterministiskt genererede ressource-tilstande. Vi anvender en kvantepunkt-udsender, der gennem sit spin genererer entanglede fotoner. Fotonerne er entanglede med kvantepunktets spin på forskellige tidspunkter, og fusion-operationen resulterer i entanglement af spinnet med sig selv på et andet tidspunkt. Vores eksperiment antyder at der findes symmetri mellem rum og tid i fusionsnetværker, og den åbner op for muligheden for nye hardware-effektive arkitekturer.

Derefter viser vi sammenføring mellem enkeltfotoner fra et kvantepunkt og fotoniske integrerede kredsløb (PIC'er). Vi demonstrerer, at enkelt- og flerfotonsoperationer kan udføres på en mikrochip lavet af silicium-nitrid, en materialeplatform egnet til storskala produktion. Vi finder, at fotonisk forskellighed er en af de vigtigste begrænsende faktorer for nøjagtigheden af fusion-operationer på chippen.

Vi adresserer denne begrænsning ved eksperimentelt at demonstrere, at højst enstartede fotoner kan opnås gennem kvanteinterferens mellem flere fotoner og varslet detektion på en delmængde af dem. Vi kalder dette fænomen ensartethedsrensning og finder, at dets effektivitet er uafhængig af den fejlkilde der inducerer forskelligheden.

Endelig anvender vi en stor programmerbar silicium-PIC til succesfuldt at implementere en metode til at gentage grundtilstandsdynamikken i forskellige interagerende spinsystemer. Denne opgave er svær at udføre effektivt med klassiske algoritmer, hvilket viser kraften i kvanteemittere og fotonisk integrerede kredsløb til analog kvantesimulering og antyder, at de teknologier, der præsenteres i denne afhandling, også har umiddelbare anvendelser.

Acknowledgements

Apart from myself, there are three main characters in the making of this thesis: Peter Lodahl, Stefano Paesani and Patrik Isene Sund. Peter as the main supervisor has chosen the direction and created some vital opportunities for me. Without his direction I would not have participated in the spin-fusion experiment nor gone to Vienna to perform the indistinguishability purification experiment. Stefano as the secondary supervisor is undoubtedly the mastermind behind the experiments listed in this thesis. His inputs were not only essential for the design of every single one of these experiments, but also for most of the simulations performed to understand them. And Patrik, who as my twin PhD student, also participated actively in every single one of my experiments, and the discussions with him were essential for the understanding of quantum physics that I have today. Without these three people, this thesis would look completely different, if even in existence, and I cannot thank them enough for their help.

All of my experiments where highly collaborative, and I could not have performed any of them on my own. Yijian Meng and Ming Lai Chan made the fusion experiment happen, and I am grateful to have had the chance to work with and learn from two of the world leading experts in quantum dot spin-photon entanglement. The silicon nitride experiment was performed together with Ying Wang and Fabian Ruf, whose knowledge in single-photon sources and photonic integrated circuits was essential for the making of this thesis. The indistinguishability purification experiment was performed at the University of Vienna, under the supervision of Juan Loredo and Philip Walther. I had the pleasure to work intensely in the laboratory with Lorenzo Carosini, whose skill and perseverance made it possible to perform the experiment and data analysis in the short ammount of time I was there. The last in this list is Alif Laila Muthali, who designed an amazing silicon chip at DTU and came to Copenhagen to perform the quantum simulation experiment together with Patrik and myself. To the people I just mentioned, thank you so much for making these experiments a reality. Thanks to Anders, Leonardo and Klaus who, even though they did not supervise me directly, helped me countless times providing great discussions and guidance.

A key element in the making of this thesis, is the joy experienced while this worked was performed. The joy of going to work with wonderful colleagues in an exciting social environment. This is largely due to the efforts of Teresa Klara Pfau and Kasper Hede Nielsen, who appart from being important friends to me, also have created many wonderful events together with me at the PhD and Postdoc network (NPN). Later additions to the NPN include Clara Henke and Pablo Martinez M., who also provided important emotional support in the final stages of this work. I also want to thank my bouldering crew: Teresa, Kasper, Xiang and Jakob, and my gym crew: Eric P., Rebecca, Shikai and Cassandra; all of whom apart from keeping me fit during these three years, also listened patiently to all of my excitement and complaints. I want to thank my great office mates: Sho, Eric L., Felix, Larissa and Atefeh, for keeping the spirits high at any moment, and to my non office mates: Aida, Celeste, Evi and

Marcus for visiting me constantly and taking me out for coffee, beers or just chatting. A special mention should go to Frederik, Dorte and Erika, who allowed me to spend countless hours working on my thesis instead of doing administratory work. At last thanks to my students: Søren, Andrew, Stefan and Nikos for trusting me with their valuable time and helping me both with theory and experiments.

Most importantly are the people who were there all along. Thanks to my parents for loving, guiding and supporting me to be the person I am, and thanks to my brother and sister for being there at every step of that process.

Unfortunately, this thesis is not long enough to express my gratitude and mention all the people who meant something to me during these three years. I did not mention every member of the Hy-Q research center by name, but I am certain that every single one of them mean something to me. My other scientific environment was also remarkable: thanks to the kind people in Vienna who took good care of me and made the time there for me truly enjoyable. Thanks to my friends outside of NBI for so many good moments and due relief from work.

For all your help, support and good times, I am truly grateful.

List of Publications

This thesis is based on the following publications, in which essential contributions were made by the author:

Journal Articles

1. Yijian Meng, Carlos F.D. Faurby, Ming Lai Chan, Patrik I. Sund, Zhe Liu, Ying Wang, Nikolai Bart, Andreas D. Wieck, Arne Ludwig, Anders S. Sørensen, Stefano Paesani, Peter Lodahl. **Photonic fusion of entangled resource states from a quantum emitter.** *arXiv preprint, arXiv:2312.09070.*. Dec 2023.

2. Ying Wang, Carlos F.D. Faurby, Fabian Ruf, Patrik I. Sund, Kasper H. Nielsen, Nicolas Volet, Martijn J. Heck, Nikolai Bart, Andreas D. Wieck, Arne Ludwig, Leonardo Midolo, Stefano Paesani, Peter Lodahl. **Deterministic photon source interfaced with a programmable silicon-nitride integrated circuit.** DOI: *npj Quantum Information. 9(1):94.*. Sep 2025

3. Carlos F.D. Faurby, Lorenzo Carosini, Huan Cao, Patrik I. Sund, Lena M. Hansen, Francesco Giorgino, Andrew B. Villadsen, Stefan N. van Den Hoven, Peter Lodahl, Stefano Paesani, Juan C. Loredo, Philip Walther. **Purifying photon indistinguishability through quantum interference.** *Physical review letters. 19;133(3):033604.* Jul 2024

4. Alif Laila Muthali, Patrik I. Sund, Carlos F.D. Faurby, Cagin Ekici, Jeremy C. Adcock, Jasper Glindemann, Stefano Paesani, YunHong Ding. **Photonic quantum simulation of disordered spin systems on a programmable silicon chip.** *In preparation.*

Conference Papers

1. Carlos F.D. Faurby, Ying Wang, Stefano Paesani, Fabian Ruf, Nicolas Volet, Martijn J.R. Heck, Andreas D. Wieck, Arne Ludwig, Leonardo Midolo, Peter

Lodahl. **Quantum-Dot Single-Photon Sources Processed on Silicon-Nitride Integrated Circuits** *CLEO: Fundamental Science*, San Jose-California, 2023

2. Fabian Ruf, Carlos FD Faurby, Stefano Paesani, Ying Wang, Lars Nielsen, Leonardo Midolo, Nicolas Volet, Martijn Heck. **Fast All-Optical Switches in Si3N4 Photonic Integrated Circuits for Single-Photon Routing.** *SPIE Optics+Photonics*, San Diego-California, 2022

Other Publications

In the duration of this work, the author also contributed to the following publication which is not discussed in this thesis

1. Beatrice Da Lio, Carlos F.D. Faurby, Xiaoyan Zhou, Ming Lai Chan, Ravitej Uppu, Henri Thyrrestrup, Sven Scholz, Andreas D. Wieck, Arne Ludwig, Peter Lodahl, Leonardo Midolo **A Pure and Indistinguishable Single-Photon Source at Telecommunication Wavelength** *Advanced Quantum Technologies.* May 2022.

Scientific Outreach

The author also contributed to the following scientific outreach article

1. Carlos F.D. Faurby, Peter Lodahl **En kvantecomputer baseret på lys** *Kvant, Tidskrift for Fysik og Astronomi.* December 2023

Thesis statement

Some of the text and figures presented in this thesis are reproduced from articles and preprints based on the work described in this thesis. This applies especially to experimental setup descriptions and experimental results, where the wording used in these manuscripts is essential for an accurate description of the experiments.

The reproduced figures are specified and a due reference is added on the figure text. The reproduced text is preceded by a statement in *Italic* script at the beginning of the section where it appears.

- **Chapter 2** has Figure 2.3.2(a) reproduced from the following article where the author did not contribute

  Le Jeannic, H., Tiranov, A., Carolan, J., Ramos, T., Wang, Y., Appel, M.H., Scholz, S., Wieck, A.D., Ludwig, A., Rotenberg, N. and Midolo, L., 2022. Dynamical photon–photon interaction mediated by a quantum emitter. *Nature Physics*, 18(10), pp.1191-1195.

  And Figure 2.3.2(b) similarly reproduced from the following article

  Knill, E., Laflamme, R. and Milburn, G.J., 2001. A scheme for efficient quantum computation with linear optics. *Nature*, 409(6816), pp.46-52.

- **Chapter 3** Is based on the following preprint

  Meng, Y., Faurby, C.F., Chan, M.L., Sund, P.I., Liu, Z., Wang, Y., Bart, N., Wieck, A.D., Ludwig, A., Midolo, L. and Sørensen, A.S., 2023. Photonic fusion of entangled resource states from a quantum emitter. *arXiv preprint arXiv:2312.09070.*

  The experimental setup and result sections along with their figures are reproduced with minor changes from this preprint.

- **Chapter 4** Is based on the following published article

Wang, Y., Faurby, C.F., Ruf, F., Sund, P.I., Nielsen, K., Volet, N., Heck, M.J., Bart, N., Wieck, A.D., Ludwig, A. and Midolo, L., 2023. Deterministic photon source interfaced with a programmable silicon-nitride integrated circuit. *npj Quantum Information*, 9(1), p.94.

Some of the figures and the experimental results section are reproduced with minor adjustments from this article.

- **Chapter 5** Is partially based on the following published article

Faurby, C.F., Carosini, L., Cao, H., Sund, P.I., Hansen, L.M., Giorgino, F., Villadsen, A.B., Van Den Hoven, S.N., Lodahl, P., Paesani, S. and Loredo, J.C., 2024. Purifying photon indistinguishability through quantum interference. *Physical review letters*, 133(3), p.033604.

The figures and description of experimental results of the space-domain experiment are reproduced with minor adjustments from this article.

Contents

Chapter 1

Introduction

The concept of a quantum computer, first proposed by Richard Feynman, refers to a machine that leverages the complexities of quantum mechanics to solve problems that are intractable for classical computers [1, 2]. This idea has generated high expectations and driven substantial investments in the research and development of the underlying technologies. While quantum computers already exist, the current challenge lies in scaling them to the sizes and complexities necessary to address problems beyond the reach of classical computing. It remains uncertain which fundamental technological platform will ultimately prove to be the most suitable for achieving this goal.

Light, as electromagnetic waves, plays a crucial role in physics and technology. Understanding and controlling light has enabled significant advancements in the photonics industry, such as the development of lasers and the global internet. The quantum mechanical description of light reveals its potential for even more applications. Light is composed of photons, indivisible quanta of light that exhibit both particle and wave characteristics. Photons may hold the potential to address some of today's major technological challenges, such as enabling the construction of a sufficiently large quantum computer capable of solving complex problems relevant to our society.

There are two main approaches to quantum information processing with light. The first is continuous-variable based, which usually relies on squeezed light sources, where classical light acquires quantum properties by propagating through non-linear materials [3, 4, 5, 6, 7]. The second is discrete-variable based, where single photons are used as qubits, which is the focus of this thesis. Single photon sources can be categorized into two fundamental classes based on their photon emission characteristics. The first class is heralded single-photon sources, where a light pulse goes through a non-linear crystal generating a squeezed state of light. If the pulse has a low power, the two-photon component of the light will be dominant, resulting effectively in a photon pair being emitted. [8]. The two photons are sent into two separate paths, where a detector is included in one of the paths. Every time the detector clicks, there is with certainty a single-photon on the free path. The second class is quantum emitters, where a quantum two-level system is excited with a laser such that it decays by emitting a single photon. Heralded single-photon sources exhibit many advantages over

quantum emitters, like room-temperature operation and high indistinguishability of their emitted photons [9]. Conversely, the fundamental nature of heralded sources is intrinsically probabilistic. A low pulse power has a low chance of resulting in a photon pair, but a high pulse power results in increased probability of generation of higher photon-number states, decreasing the multi-photon component of the emitted photons. Quantum emitters do not exhibit this trade-off between brightness and purity, as a single photon can in principle be deterministically generated by the right pulse excitation. This fundamental difference gives quantum emitters an edge in future technologies where scalability and high count rates are key for the successful production of large scale quantum information processing systems.

Quantum emitters are two level systems and as such can be realized in many platforms. Some examples are color centers in diamonds [10, 11], organic molecules [12], trapped atoms [13], and quantum dots [14]. Among these, quantum dots in semiconductor environments have gained special attention due to the high interference visibility between emitted photons and capability to interfere photons emitted at very different times [15, 16, 17]. They are promising candidates as single-photon sources for large scale quantum information processing, and will be the object of our study of this thesis.

Processing of single photons generated from a quantum emitter is typically performed through free-space optics. This has been extremely useful for research purposes, where a multitude of applications have been shown [18, 19, 20]. However, free space optics require large optical tables even for small-scale proof-of-principle experiments and are not suitable for mass fabrication. The solution lies in classical information science, where advancements in telecommunications technologies have driven significant development and mass production of microchips capable of containing and processing light. These microchips are known as photonic integrated circuits (PIC). A central challenge in developing scalable photonic quantum hardware is to realize high-quality single-photon sources and interface them with advanced photonic integrated circuits. This interface will play a central role in this thesis, as we present different material platforms and evaluate their performance on simple quantum computing and quantum simulation tasks.

Given a set of qubits, an initial approach to universal quantum computing has two requirements: execution of any single-qubit operation, and excecution of the entangling operation between two qubits, commonly referred to as a CNOT gate. Photons do not interact directly with each other, making it challenging to perform CNOT gates or any other entangling operations with them. However, it is possible to generate entangled photons previous to any operations being performed. If we can implement a quantum computing approach that only requires operations on already-produced entangled photons, photonic quantum computing will be within reach. Fusion-based quantum computation is an example of such an approach. It requires the generation of sets of entangled photons and the application of certain measurement operations between them called fusion operations. In this thesis we will take experimental steps towards the realization of fusion-based quantum computing operations, first in bulk

linear optics and then realizing them on photonic integrated circuits.

The thesis is structured as follows:

- **Chapter 2** describes the basic theory regarding the physics of single photons. We will describe the basic physics of how QDs emit single photons, and the mathematical framework required to describe interference and entanglement between them.
- **Chapter 3** gives a closer introduction to fusion-based quantum computation and the requirements to implement it in practice. We describe a proof-of-principle experiment implementing a simple fusion-based operation. The operation involves a fusion of two resource states generated at different instances in time and results in entanglement of an emitter with its past self.
- **Chapter 4** takes a deep look at the interface between QD single-photon sources and integrated circuits. We present an experiment where different quantum interference operations are implemented with a modular approach connecting a QD single photon source and a PIC in silicon nitride. We test the performance of an on-chip fusion circuit by evaluating its ability to generate post-selected entangled states.
- **Chapter 5** proposes a method to further improve the indistinguishability of single photons generated from a QD, essential for achieving higher fidelities in fusion-based quantum computing operations.
- **Chapter 6** provides further exploration of the applications of photonic integrated circuits. We provide an algorithm that employs a photonic circuit to find the ground state dynamics of interacting spin system and a proof of principle experiment where some of these dynamics are observed.

Chapter 2

Single-photon Basics

In this chapter we give a brief introduction to how single photons are generated and how they interfere with each other on photonic interferometers.

2.1 Single-photon generation

2.1.1 Quantum dots

Quantum dots (QDs) are artificial atoms made up of thousands of real atoms confined in a specific region in space [21]. We will be placing our focus on epitaxial quantum dots, which are semiconductor islands that spontaneously appear when two materials of different lattice constant are grown next to each other in order to reduce the strain [22]. The name epitaxial comes from the growth technique used to deposit thin films of material on top of each other which is called molecular beam epitaxy [23]. A well developed material combination for epitaxial quantum dots is that of GaAs and InAs, where islands of InAs as shown in Figure 2.1.1(a) form to relieve the strain from the contact with the GaAs. A picture of a quantum dot obtained from a tunnelling electron microscope is presented in Figure 2.1.1(b), showing that these quantum dots are around 10 nm in size [14].

QDs interact with light by trapping electrons and holes from their surrounding semiconductor environment, but if no engineering of their surroundings is made, it is highly unlikely for carriers to be trapped inside them. In order to achieve electrical control of the QD, a capacitor-like material structure design is used [24]. This material layer illustrated in Figure 2.1.1(c). The top and bottom layers consist of a p and an n-doped layer of GaAs, which together with the intrinsic GaAs layers in between form a p-i-n junction. The p and n layers are put in contact with electrical wires leading to a bias voltage V_{bias}, which creates an electric field in between the layers. The electric field shifts the energy levels of the QDs through the Stark effect. The $Al_{0.3}Ga_{0.7}As$ layer is known as the sacrificial layer, which is removed during the fabrication of nano-structures in the platform in order for them to be suspended with air on both sides. When growing the layer of InAs on top of the i-GaAs layer only a thin layer of a

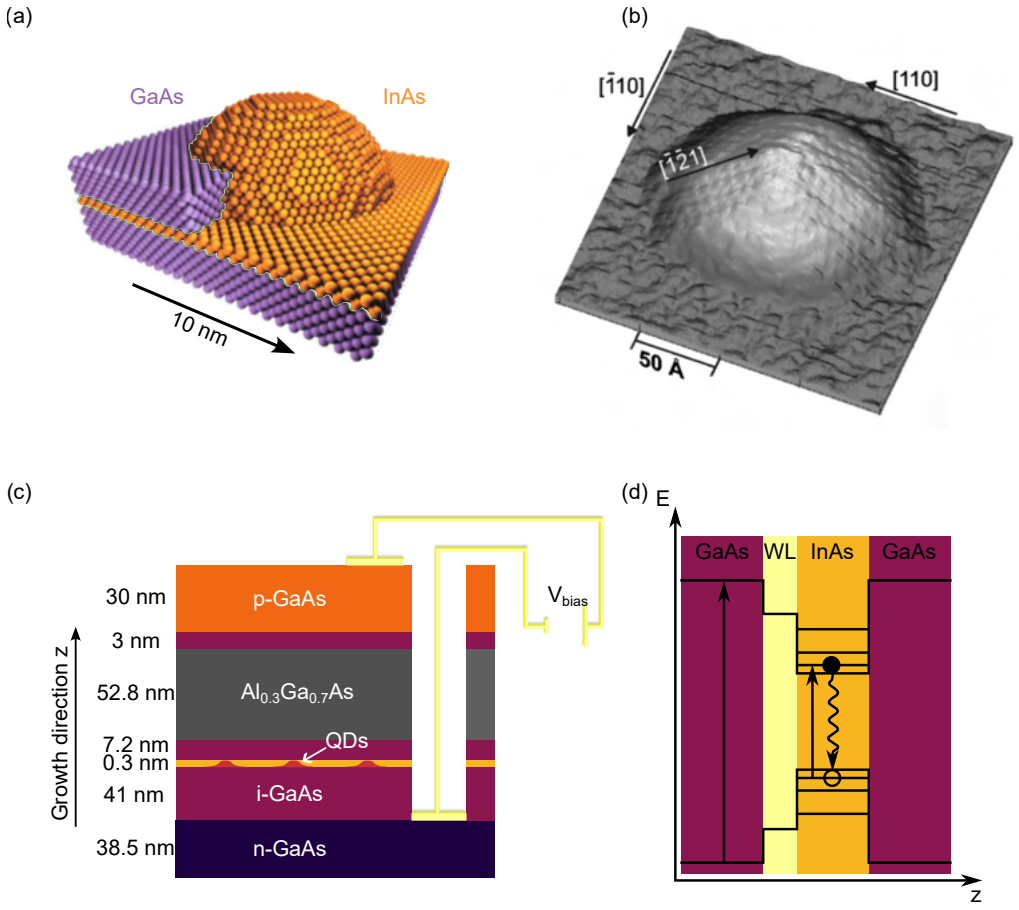

Figure 2.1.1: (a) Depiction of a InGaAs quantum dot showing that it is made of a multitude of individual atoms. (b) Scanning tunneling-microscope image of a quantum dot. [25] (c) Material layers used in our QD wafers. (d) Diagram of the energy levels in the vicinity of the quantum dots. [26]

few atoms can form before the difference in tension results in the formation of QDs. This thin layer is known as the wetting layer and has a thickness of about 0.3 nm. We show an expanded view of the layers around the QD in Figure 2.1.1(d), where the wetting layer (WL) is shown separately from the InAs layer of atoms belonging to the QD. In the same figure we show the energy level structure for electrons (top) and holes (bottom) in the material platform. It can be observed that the minimum energy difference lies at the spot where the QD is located, which is what allows for the trapping of electrons and holes inside it. The black arrow on the left denotes above-band excitation, where an electron-hole pair is created on the GaAs material layer and recombines within the QD.

QD decay schemes

The recombination of an electron an a hole inside a QD results in emission of a single photon. The QD can be populated with different electron-hole configurations depending on the applied bias voltage and the light that it is being excited with. We show the lowest energy states and their usual denominations in Figure 2.1.2(a). There are many different transitions that can be used for single-photon generation and for entanglement generation. We will explain the two transitions that are relevant for this thesis. Generation of single-photons is usually achieved through the neutral exciton,

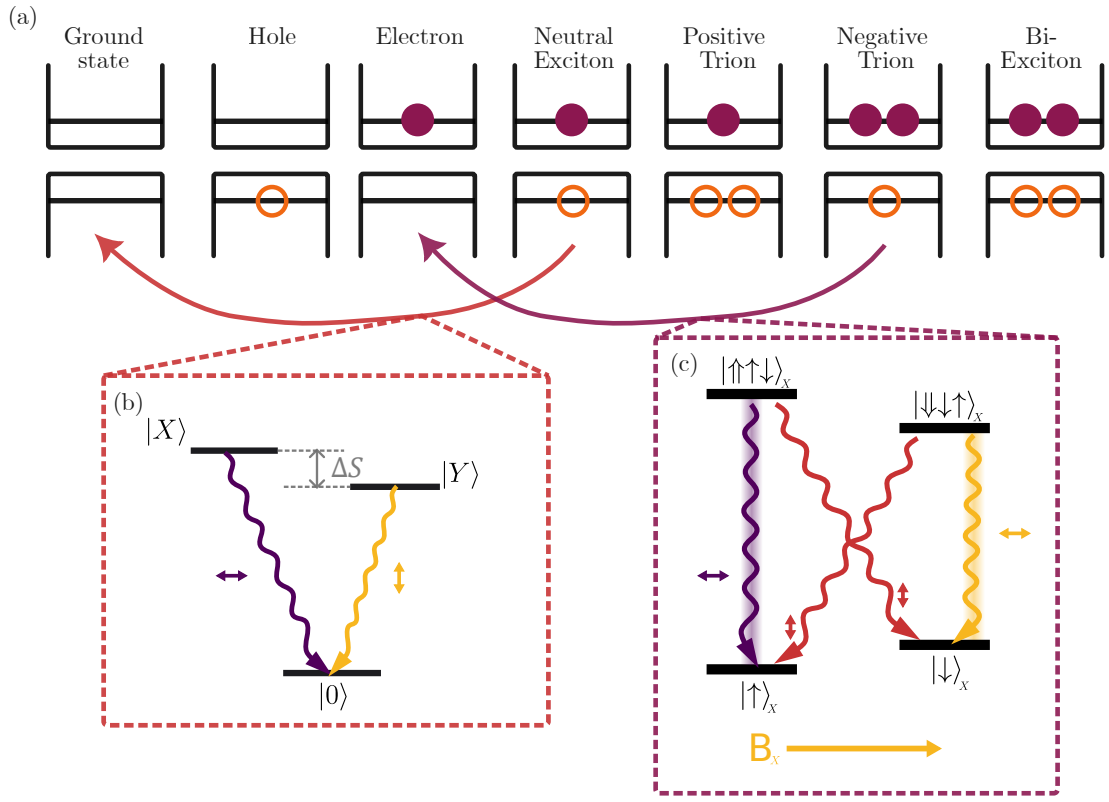

Figure 2.1.2: (a) Lowest quantum dot excited states and their denominations. (b) Fine structure splitting of the neutral exciton, which gives rise to two dipoles that can decay to the ground state with opposite linear polarizations. (c) Illustration of a negative trion to electron transition when exposed to a magnetic field in the Voigt geometry.

which decays to the ground state emitting a single photon. Rabi-oscillations between these two states can also be achieved through interaction with a pump laser. The electron and the hole in the Neutral exciton both have spins, if the wave-functions of the electron and the spin do not overlap perfectly, their spins interact magnetically giving rise to a fine-structure splitting of the state. The overlap would be perfect if the QD was completely symmetrical, but due to fabrication strain, the QD will typically

be elongated in one dimension, making the overlap imperfect. The splitting creates two different dipoles, we call them X and Y dipoles and are defined as

$$|X\rangle = \frac{|\Uparrow\downarrow\rangle - |\Downarrow\uparrow\rangle}{\sqrt{2}}, \qquad |Y\rangle = \frac{|\Uparrow\downarrow\rangle + |\Downarrow\uparrow\rangle}{\sqrt{2}}, \tag{2.1.1}$$

where simple arrows denote the electron spin, while double arrows denote the hole spin. The couplings to the ground state of the two dipoles have opposite linear polarizations as illustrated in Figure 2.1.2(b).

Generation of entangled-single photons can be achieved through the transition going from the negative trion to the electron or from the positive trion to the hole. This is because we can induce Zeeman splitting of either the electron or the hole by applying a magnetic field, giving different ground state levels useful for addressing individual transitions. In this thesis we make use of the transition going from negative trion to electron, and we apply a magnetic field in the Voigt geometry (more details in Chapter 3). The energy levels arising in this scenario are illustrated in Figure 2.1.2(c). We note that all the states are given in the x-basis, such that for example $|\uparrow\rangle_x = (|\uparrow\rangle + |\downarrow\rangle)/\sqrt{2}$, which makes all of the transitions have linear polarization.

More details regarding excitons and biexcitons transitions can be found in [26]. More details about trion transitions can be found in [27, 28].

2.1.2 Confinement and extraction of light

In order for a photon to be used for specific means, it has to be collected with near unity efficiency to enable deterministic delivery to its intended destination.

We use 2-dimensional photonic crystal waveguides (PCWs) to confine the light emitted from the QDs. Our PCWs are composed of a 2D array of holes which forbids on-chip light propagation. Removing a row in the hole array allows for light propagation in the empty section. If a quantum dot is located on the empty section, as illustrated in Figure 2.1.3(a), its emitted photons will propagate on the PCW. Our devices are designed such that there is air surrounding the GaAs layers. The refractive index difference between air and GaAs is high, confining the photons along the z-dimension. The structures are suspended using tethers such that they do not fall down into the empty region.

The single photons are transferred from the PCW to a nano-beam waveguide as these exhibits slightly lower propagation losses. At the end of the nano-beam waveguide there is a shallow edge grating (SEG) that couples the light out of the chip. This is all illustrated is Figure 2.1.3(b), where the tethers that hold the structures suspended also can be seen. The devices are fabricated on a wafer full of randomly distributed QDs, meaning that the QDs can be anywhere within the device. Some of the QDs will be within the propagation-capable region, emitting photons that will follow the path of the waveguide. The density of the QDs is such that it is highly

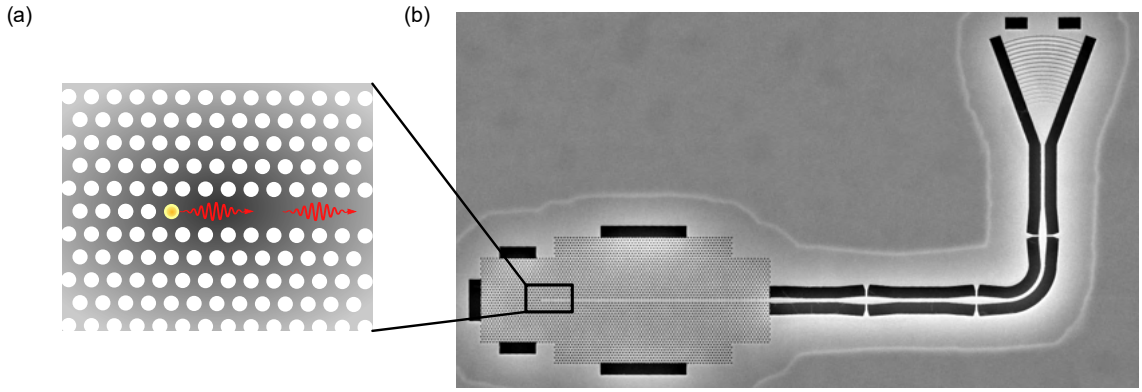

Figure 2.1.3: (a) Quantum dot in the center of a photonic crystal waveguide (PCW). The photons can only propagate in the direction dictated by the waveguide. The QD is not to scale. (b) SEM image of the full PCW device. The structure is suspended and kept in place using tethers (in black). The light is coupled off-place through the shallow edge grating at the end of the structure.

likely to find multiple useful QDs within a device, but highly unlikely that one laser spot will resonantly excite multiple dots simultaneously.

Our PCWs not only confine the light emitted from the QD but also change the emission properties of the two-level system. As the local-density of states is lower within the PCW than in free space, the interaction of the QD dipole with the surrounding electromagnetic field is diminished, increasing the lifetime of the optical transition. This is known as Purcell enhancement. The closer the wavelength of a QD is to the bandedge of the PCW, the more Purcell enhancement it experiences [29]. A high Purcell enhancement allows for higher emission rate of the QD, which in the long run means that it can be excited more frequently, getting more photons out per time unit. A high Purcell enhancement also means a low lifetime, which decreases the ammount of time that the electron-hole pair can interact with phonons in the semiconductor environment. As we will see in Chapter 5, low phonon interaction allows for a higher indistinguishability of the emitted photons.

Quality of single photons

When judging deterministic single photon sources, there are three metrics that are used to determine their quality, as they are essential for multi-photon experiments and quantum information processing.

Efficiency. The efficiency of a single photon source is defined as the probability of having a fiber-coupled photon per excitation laser pulse. This quantity is more descriptive than the brightness of the source, which is the raw count rate of emitted photons, as the total losses of a multi-photon experiment increase exponentially with the number of photons.

Purity. The purity of a source describes the probability of having multi-photon

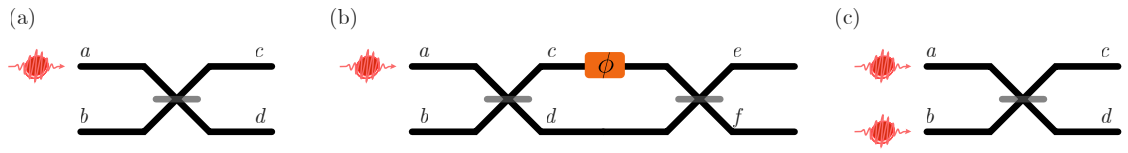

Figure 2.2.1: (a) Photon scattering on a beam splitter. (b) Photon scattering on a Mach-Zender interferometer. (c) Two-photon interference on a beam splitter.

components in the emitted pulses, which should ideally only have a single-photon component. It is quantified by the autocorrelation function $g^{(2)}(0)$, which is measured on a Hanbury-Brown and Twiss experiment. High purity of single photons is essential not only for multi-photon experiments but also for quantum communication experiments which only require single photons.

Indistinguishability. The indistinguishability of a single-photon source describes how likely two photons from the source are to interfere with each other. It is quantified by the Hong-Ou-Mandel (HOM) visibility, also known simply as the indistinguishability, which is obtained by performing a HOM interference experiment. A note of caution should be made as in certain literature the HOM visibility is the square of the indistinguishability, but in other literature they are equal to each other. In this thesis we take the convention where they are equal to each other.

2.2 Single-photon interference

In this section we describe the mathematical framework used to predict the outcome of various single-photon interference experiments.

We start by describing the interference of a photon with itself. We define a photon as the excitation of a mode a on the electromagnetic vacuum

$$|1_a\rangle = a_a^\dagger |0\rangle \ , \tag{2.2.1}$$

where the creation operator $a^\dagger$ satisfies the commutation relations

$$\begin{aligned} \left[a_i, a_j^\dagger\right] &= \delta_{ij} \, , \\ [a_i, a_j] = 0 \left[a_i^\dagger, a_j^\dagger\right] \ . \end{aligned} \tag{2.2.2}$$

These commutator relations are essential and should always be satisfied after propagation through an optical element. Enforcing this condition on a photon going through a beam splitter (BS) gives the transformation

$$\begin{aligned} a_a^\dagger |0\rangle &\to \frac{1}{\sqrt{2}} \left(a_c^\dagger + a_d^\dagger\right) |0\rangle \\ a_b^\dagger |0\rangle &\to \frac{1}{\sqrt{2}} \left(a_c^\dagger - a_d^\dagger\right) |0\rangle \ , \end{aligned} \tag{2.2.3}$$

with a, b, c and d being the modes introduced in Figure 2.2.1(a). We observe that the photon enters in a superposition of being in both output paths simultaneously. A measurement of the photon would though collapse it to be only on one arm with a probability of 50% for each arm. This fact, that a single photon going through a BS will result in coincidence counts at two output detectors, is the principle behind the Hanbury-Brown and Twiss experiment.

Similarly the commutator relations require for a photon going through a phase-shifter giving a phase ϕ to transform as

$$a_a^\dagger |0\rangle \to e^{i\phi} a_a^\dagger |0\rangle \ , \tag{2.2.4}$$

which is an overall phase for the wave-function that becomes irrelevant when calculating probabilities. On the other hand, if the photon interferes with itself, it becomes relevant. As an example, we examine scattering of a single photon through a Mach-Zender interferometer (MZI), illustrated in Figure 2.2.1(b).

$$\begin{aligned} a_a^\dagger |0\rangle &\to \frac{1}{\sqrt{2}} \left(a_c^\dagger + a_d^\dagger\right) |0\rangle \to \frac{1}{\sqrt{2}} \left(e^{i\phi} a_c^\dagger + a_d^\dagger\right) |0\rangle \\ &\to \frac{1}{2} \left(e^{i\phi} \left(a_e^\dagger + a_f^\dagger\right) + \left(a_e^\dagger - a_f^\dagger\right)\right) |0\rangle = e^{i\phi/2} \left(\cos(\phi) a_e^\dagger - \sin(\phi) a_f^\dagger\right) |0\rangle \ . \end{aligned} \tag{2.2.5}$$

Here we see that the photon interferes constructively or destructively with itself depending on the phase.

Next we explore what happens when two photons interfere with each other at a beam splitter, as illustrated in Figure 2.2.1(c). It follows from eq. 2.2.3 that

$$a_a^\dagger a_b^\dagger |0\rangle \to \frac{1}{2} \left(a_c^\dagger + a_d^\dagger\right) \left(a_c^\dagger - a_d^\dagger\right) |0\rangle = \frac{1}{2} \left(a_c^{\dagger 2} + a_d^{\dagger 2}\right) |0\rangle \ , \tag{2.2.6}$$

where the cross terms cancel if the photons are completely indistinguishable, allowing only for the two photon components. This means that two photons interfering perfectly on a beam splitter will bunch, such that if a detector pair is placed at the output paths, coincidences will never be measured. This is known as the Hong-Ou-Mandel (HOM) effect.

It should be noted that any phase added to any of the input photons will become an external phase and thus not affect the outcome of the experiment. Phases are thus only relevant when single photons interfere with themselves.

The framework introduced can describe any photonic interferometer composed of phaseshifters and beam-splitters. We call those linear interferometers, as the phases induced by the BSs and the phaseshifters are linear in the number of photons and can be computed individually from each other. It is also the case that any linear operation for a set of photons can be performed using only BSs, and phaseshifters, as it can be proven that any unitary matrix operation can be replicated with these components [30]. Thus the introduced framework is enough to compute the outcome of any linear photon scattering event. This is, assuming the photons are indistinguishable. If the photons are distinguishable the framework needs to be expanded.

We now introduce the methods described in [31] to compute scattering of distinguishable photons. *This description and the one in the next subsection is adapted with minor adjustments from [32].*

For this model we define a photon as having a wavepacket in the form of

$$a_i^\dagger \equiv \int_{-\infty}^{\infty} f_i^*(t) a_i^\dagger(t) dt \,, \tag{2.2.7}$$

where $f_i^*(t)$ is a normalized function and $a_i^\dagger(t)$ is the creation operator for photon i in mode a with commutator relations

$$\left[\hat{a}_i(t), b_j^\dagger(t')\right] = \delta_{ab}\delta(t-t') \,. \tag{2.2.8}$$

We turn our attention to distinguishability of photons emitted by a quantum dot. QDs are subject to spectral diffusion, which is a shift in the resonance frequency due to electric fields in the environment, and they are subject to pure dephasing, which is a fast dephasing process mainly caused by interaction with phonons. Solving Schrödingers equation for the system a the quantum dot pertubed by a slow frequency detuning, Δ_i, and rapidly varying fluctuations giving rise to a random phase $\phi_i(t)$, one can determine the expression for the wavepacket function to be [31]:

$$f_i(t, t_0) = \begin{cases} \sqrt{\gamma} e^{-\frac{\gamma}{2}(t-t_0)} e^{-i(\Delta_i(t-t_0)+\phi_i(t,t_0))}, & t \geq t_0 \\ 0, & t < t_0 \end{cases} \,, \tag{2.2.9}$$

where γ denotes the decay rate of the emitter. The expectation value of the overlap between wavepackets from two different photons can then be calculated. If we assume that the photons come from the same source and thus $\Delta_i = 0$, since for quantum dots the time-separation between two consecutive photons is much lower than the spectral diffusion rate [16]. The overlap is then

$$\left| \int_{-\infty}^{\infty} f_i^*(t) f_j(t) dt \right|^2 \equiv \langle |\alpha_{ij}|^2 \rangle = \frac{\gamma}{\gamma + 2\gamma_d} \,, \tag{2.2.10}$$

with γ_d being the pure dephasing rate of the emitter.

Using this formalism, two photons interfering through a BS will have coincidence probability

$$P_{cc} = \frac{1 - \langle |\alpha_{ij}|^2 \rangle}{2} \,, \tag{2.2.11}$$

suggesting that the quantity $\langle |\alpha_{ij}|^2 \rangle$ is analogous to the intrinsic indistinguishability of the photons.

2.2.1 Permanents in multiphoton interference

If we want to compute the scattering of many photons in many modes, the formalism introduced above quickly becomes impractical. We now introduce a formalism that is

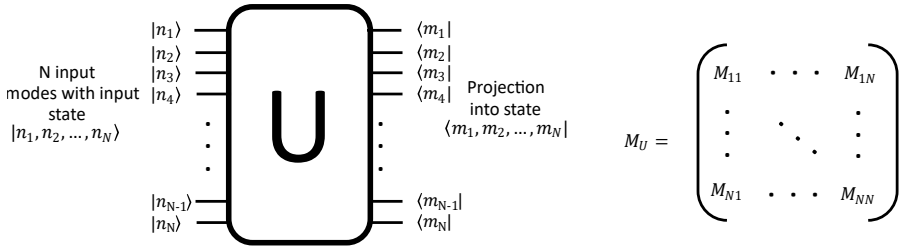

Figure 2.2.2: A linear circuit induces a unitary state evolution U, resulting in a transfer matrix M_U. Figure reproduced from [32]

equally complex to calculate, but has the advantage that it can easily be implemented on computer code.

We start by a brief summary of the permanent model used to calculate the evolution of any state through a linear circuit inducing a unitary transformation in the case of perfectly distinguishable photons as proposed by [33]. A generic circuit is depicted in Fig. 2.2.2, where N input modes in the state $|m_1, m_2, ..., m_N\rangle$ go through the circuit and are projected into the state $|n_1, n_2, ..., n_N\rangle$. The evolution U has a unique transfer matrix M_U. We wish to find an expression for the probability of having the described final state given an input state and all the elements of the transfer matrix.

We will introduce the following notation to extract the relevant elements of the transfer matrix for a given input-output configuration:

$$B = M[(1^1, 2^1, 3^1)|(1^0, 2^2, 3^1)] = \begin{pmatrix} M_{12} & M_{12} & M_{13} \\ M_{22} & M_{22} & M_{23} \\ M_{32} & M_{32} & M_{33} \end{pmatrix} . \tag{2.2.12}$$

The amplitude for a given input-output configuration can then be calculated by

$$\langle n_1, n_2, ..., n_N| \, U \, |m_1, m_2, ..., m_N\rangle = \frac{\mathrm{Perm}(B)}{\sqrt{\prod_i n_i!}\sqrt{\prod_j m_j!}} \tag{2.2.13}$$

with Perm being an abbreviation for the matrix permanent and

$$\begin{aligned} B &= M_U[\Omega'|\Omega] \, , \\ \Omega &= (1^{n_1}, 2^{n_2}, ..., N^{n_N}) \, , \\ \Omega' &= (1^{m_1}, 2^{m_2}, ..., N^{m_N}) \, . \end{aligned} \tag{2.2.14}$$

Next we consider what happens when the photons are partially distinguishable as described in [34]. For this we define the mode assignment list $idx = (d_1, d_2, ..., d_N)$ which has a separate element for every photon in the input state. Using this we can define the distinguishability matrix

$$S_{j,k} = \left\langle \psi_{d_j} \middle| \psi_{d_k} \right\rangle \, , \tag{2.2.15}$$

which is a hermitian n by n matrix, with $S_{j,j} = 1$. If $S = I$ we have completely distinguishable photons, and if $S_{j,k} = 1$ for all j,k we have ideal boson sampling.

Next we define the 3 dimensional tensor

$$W_{k,l,j} = B_{kj} B^*_{lj} S_{lk} \tag{2.2.16}$$

and its permanent

$$\mathrm{Perm}(W) = \sum_{(\sigma,\rho)\epsilon S_n} \prod_{j=1}^{n} W_{\sigma_j,\rho_j,j} \tag{2.2.17}$$

The probability amplitude for a given input-ouput configuration using partially distinguishable photons is then computed using eq. 2.2.13 but inserting the permanent from eq. 2.2.17 instead of $Perm(B)$.

2.3 Single-photon entanglement

2.3.1 Basics of quantum entanglement

Quantum entanglement is a core principle in quantum mechanics, essential both in the early years for the understanding of the theory, and in modern times as it is the cornerstone of many quantum information applications. The generation and characterization of entanglement will constitute a central focus of this thesis. We will therefore begin by presenting the fundamental theoretical framework of entanglement.

Two particles are said to be entangled if their joint wave-function cannot be factorized into a product of the individual wave-functions. It is important to mention that entanglement is not necessarily a two particle phenomenon and it can happen between an arbitrarily large number of particles. Nonetheless, we begin by studying the simplest case, which is two-particle entanglement.

We consider two particles, both of which can be described by the orthogonal basis $|\uparrow\rangle$ or $|\downarrow\rangle$, with quantum states denoted Ψ_1 and Ψ_2. For two-particle states, there are 4 possible maximally entangled states, also known as Bell states, which are the following

$$\begin{aligned}
\left|\Phi^+\right\rangle &= \frac{1}{\sqrt{2}}(|\uparrow_1\uparrow_2\rangle + |\downarrow_1\downarrow_2\rangle)\,, \\
\left|\Phi^-\right\rangle &= \frac{1}{\sqrt{2}}(|\uparrow_1\uparrow_2\rangle - |\downarrow_1\downarrow_2\rangle)\,, \\
\left|\Psi^+\right\rangle &= \frac{1}{\sqrt{2}}(|\uparrow_1\downarrow_2\rangle + |\downarrow_1\uparrow_2\rangle)\,, \\
\left|\Psi^-\right\rangle &= \frac{1}{\sqrt{2}}(|\uparrow_1\downarrow_2\rangle - |\downarrow_1\uparrow_2\rangle)\,,
\end{aligned} \tag{2.3.1}$$

which are all superpositions of two-particle wave-functions and not separable into a product of Ψ_1 and Ψ_2. Furthermore they have the property that a measurement on any of the particles immediately reveals the state of the other particle, independently

of spatial separation between the particles, suggesting that quantum entanglement is a non-local phenomenon [35].

It should be noticed, that two particles which classically have 50% probability of being in the state $|\uparrow_1\downarrow_2\rangle$ and 50% chance of being in the state $|\downarrow_1\uparrow_2\rangle$ would exhibit the same behavior when measured as the entangled state $|\Phi^+\rangle$. One may thus be led to assume that the entanglement and subsequent wave-function collapse are unnecessary for predicting the measurement outcomes. This is though only true as long as the measurement is done in the original basis, which we will call the z-basis. Going to an orthogonal basis, like for example the x-basis, the states transform as $|\uparrow_z\rangle = \frac{1}{\sqrt{2}}(|\uparrow_x\rangle + |\downarrow_x\rangle)$ and $|\downarrow_z\rangle = \frac{1}{\sqrt{2}}(|\uparrow_x\rangle - |\downarrow_x\rangle)$, and the entangled state becomes

$$\left|\Psi_z^+\right\rangle = \frac{1}{\sqrt{2}}(|\uparrow_{1z}\downarrow_{2z}\rangle + |\downarrow_{1z}\uparrow_{2z}\rangle) = \frac{1}{\sqrt{2}}(|\uparrow_{1x}\uparrow_{2x}\rangle - |\downarrow_{1x}\downarrow_{2x}\rangle) = \left|\Phi_x^-\right\rangle , \tag{2.3.2}$$

which remains an entangled state. The difference is then that in the x-basis, a measurement of an entangled state yields correlated outcomes, while for classically mixed states the correlation only happens in the computational basis.

When changing basis the bell states transform as follows

Z	X	Y
Φ^+	Φ^+	Φ^-
Φ^-	Ψ^+	Ψ^+
Ψ^+	Φ^-	Φ^+
Ψ^-	Ψ^-	Ψ^-

Bell states have been the basis of innumerable discussions about the completeness of quantum mechanics as a a means to describe multi-particle states. In 1964 Bell [36] proposed an experiment that could determine whether quantum mechanics was non-local or just in need of extra hidden variables. In his experiment he proposed an inequality that if breached, quantum mechanics should be considered as a non-local theory. This inequality could be breached as the result of repeated experiments and statistical analysis. In 1990 Greenberger, Horne and Zeilinger proposed a similar experiment but with three and four particle entangled states instead of Bell states. In their proposition no statistical analysis was required as the completeness of quantum mechanics was directly dependent of the inmediate n-particle correlations. The states used in this proof are now known as GHZ states and have the form

$$|GHZ\rangle^N = |0\rangle^{\otimes N} + |1\rangle^{\otimes N} . \tag{2.3.3}$$

Graph states

In modern days entangled states are no longer used to discuss the nature of physical reality but as the basis of many quantum information applications. The term graph states is used to talk about bigger entangled states, and they are described as the eigenstates of a set of operators called the generators. The number of generators for

a given graph state is equal to the number of qubits in the state. The generator corresponding to the i^{th} qubit of the state can be written as follows:

$$G_i = x_i \prod_{k \epsilon \mathcal{N}} z_k \tag{2.3.4}$$

Where x_n and z_n represent the Pauli operators applied on the n^{th} qubit of the graph, and $\mathcal{N}$ represents the qubits that are connected to the i^{th} qubit. An example of a graph state and its stabilizers is given in Figure 2.3.1. All generators have eigenvalue +1 on

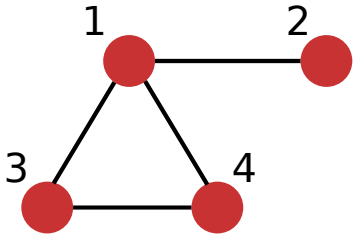

$$G_1 = x_1 z_2 z_3 z_4$$
$$G_2 = z_1 x_2 \mathbb{1}_3 \mathbb{1}_4$$
$$G_3 = z_1 \mathbb{1}_2 x_3 z_4$$
$$G_4 = z_1 \mathbb{1}_2 z_3 x_4$$

Figure 2.3.1: (a) Example of a graph state with its corresponding generators. (b) Unit cell of a Raussendorf lattice graph state.

the graph state $|\psi_G\rangle$ and commute with each other. Another important concept when talking about graph states is the concept of stabilizers, which are all the operators which have eigenvalue +1 on the given graph state. Stabilizers can be constructed as products of the generators, and as thus commute with each other.

On experimental applications there will be errors on the qubits like bit-flips of phase-flips. On graph states these would manifest as a change of parity on some of the stabilizers. If the error is a bit flip on qubit i, the state becomes $x_i |\psi_G\rangle$, and all of the generators with a z_i operation will anti-commute with the new x_i, giving them an eigenvalue of -1. As a example, in the graph state of Figure 2.3.1, a bit flip on qubit 2 would flip the eigenvalues of the generators G_1 and G_3. Also, a phase-flip on qubit i will result in a negative eigenvalue of the generator G_i.

Graph states are specially useful for quantum computation. A specific graph state known as the cluster state is essential for measurement-based quantum computation as we will describe in Chapter 3.

2.3.2 Photonic entanglement

The capability to generate entangled photons has been established for over fifty years, primarily through the use of spontaneous parametric down-conversion (SPDC) sources [8]. Recent quantum-emitter based approaches have also achieved generation of entangled photons [37], which we will be exploring in detail in Chapter 3. On the other hand, entangling single photons once they have been generated is a challenging task as it cannot be performed through linear optics alone. Entanglement requires interaction between photons, which is by nature a non-linear phenomenon.

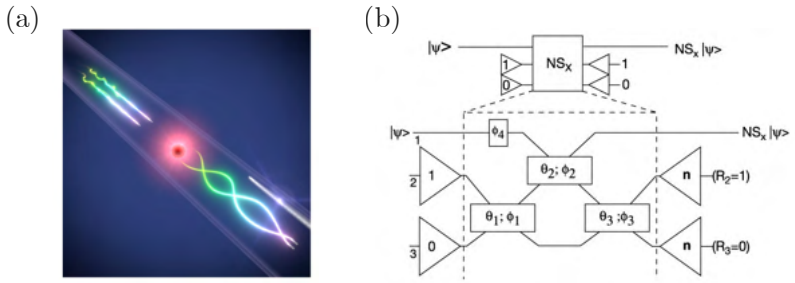

Figure 2.3.2: (a) Photon-photon interaction mediated by a quantum emitter. Figure reproduced from [38] (b) Example of a measurement-based non-linear phase-shift. An ancillary photon interferes with an unknown state of light. If the right detector pattern is detected, a non-linear phase that depends on the MZI reflectivities θ_i and external phase values ϕ_i is applied. Figure reproduced from [39]

In order to achieve non-linear operations with single photons, two approaches have been explored.

Quantum emitters mediated. Two-photon interactions can be achieved by interaction with a third party. Making single-photons interact with a quantum emitter induces non-linear phases on the photons. This phenomenon is the focus of recent studies [38, 40], and reprogrammable non-linear interferometers have been recently demonstrated [41]. Nonetheless, entanglement of single photons is yet to be achieved through these means. An artistic illustration of an emitter-mediated photon-photon interaction is shown in Figure 2.3.2(a). Photon-photon interaction through quantum emitters has the advantage that it can be achieved deterministically, but it is still to be determined what the efficiency and the range of non-linear phases that can be produced with it are.

Measurement based. Non-linearites can also be achieved through measurements, where ancillary photons are introduced in photonic interferometers and subsequently measured uppon. This results in operations that are non-linear in the number of photons. Photonic entanglement has been achieved through this method, with entanglement generation of up to three photons [19]. We will be discussing interferometer architectures that give rise to measurement-based entanglement in Chapter 4. An example of a measurement based non-linearity is shown in Figure 2.3.2(b), where an ancillary photon is interfered with an unknown state of light $|\psi\rangle$. If the ancillary photon is detected in mode 2, then the gate is succesful and a non-linear phase is applied [39]. The specifics of the non-linear phase depend on the values set for the MZIs and phaseshifters in the interferometer. Measurement based non-linearities are convenient as they only require detectors and linear-photonic interferometers, but they are probabilistic and require ancillary photons, increasing the hardware requirements for any operation that necessitates entanglement.

Chapter 3

Spin Fusion

In this chapter we describe our experiment implementing a fusion operation between two entangled resource states generated with a quantum-dot spin.

Statement of work

The work described in this chapter was performed in close collaboration with Yijian Meng and Ming Lai Chan under the supervision of Peter Lodahl. The spin-photon entanglement platform was operated mostly by Yijian Meng. The data analysis was performed by Yijian Meng and Ming Lai Chan as well as the error simulation analysis. The author of this thesis contributed to this project by building the free space fusion gate and the fiber-delay setup. Anders Sørensen and Stefano Paesani provided support with the theory and understanding of the experiment.

The work described in this chapter resulted in a manuscript specified in [42]. Some of the figures as well as the description of the experimental setup and the results were adapted with minor adjustments from this manuscript.

3.1 Introduction

As discussed in the introduction of the this thesis, a promising protocol for implementing quantum computing with photons is fusion-based quantum computation, which is a form of measurement-based quantum computation (MBQC).

Photons have the challenge that they do not interact with each other, making it hard to perform entanglement operations. It is though possible to generate entangled photons through different methods, and with some of these it is even possible to deterministically generate large entangled states. Photons on the other hand are easy to measure and easy to control. This has led to the pursue of quantum computing approaches that make use of the advantages of the photonic platform, where MBQC is one of them, also known as one-way quantum computing[43, 44, 45, 46].

The standard protocol for MBQC relies on creating a cluster state, which is a large entangled state where the qubits are arranged in a grid pattern[47]. A qubit

circuit with multiple operations can be mapped to measurements on a cluster state. In the mapping, a column of entangled qubits corresponds to the physical qubits in the circuit. Qubits along the horizontal direction correspond to time propagation among the physical qubits. Any single qubit operation can be recreated through measurements along different directions of the Bloch sphere where the orientation of future measurements depends on the results obtained in the past, an operation denominated as feedforward. This is depicted in Figure 3.1.1(a). CNOT operations can be recreated as shown in Figure 3.1.1(b), where two rows of qubits and the row connecting them are measured in the X basis. We illustrate the mapping between a regular quantum circuit and its correspondent scheme in MBQC in Figure 3.1.1 (c).

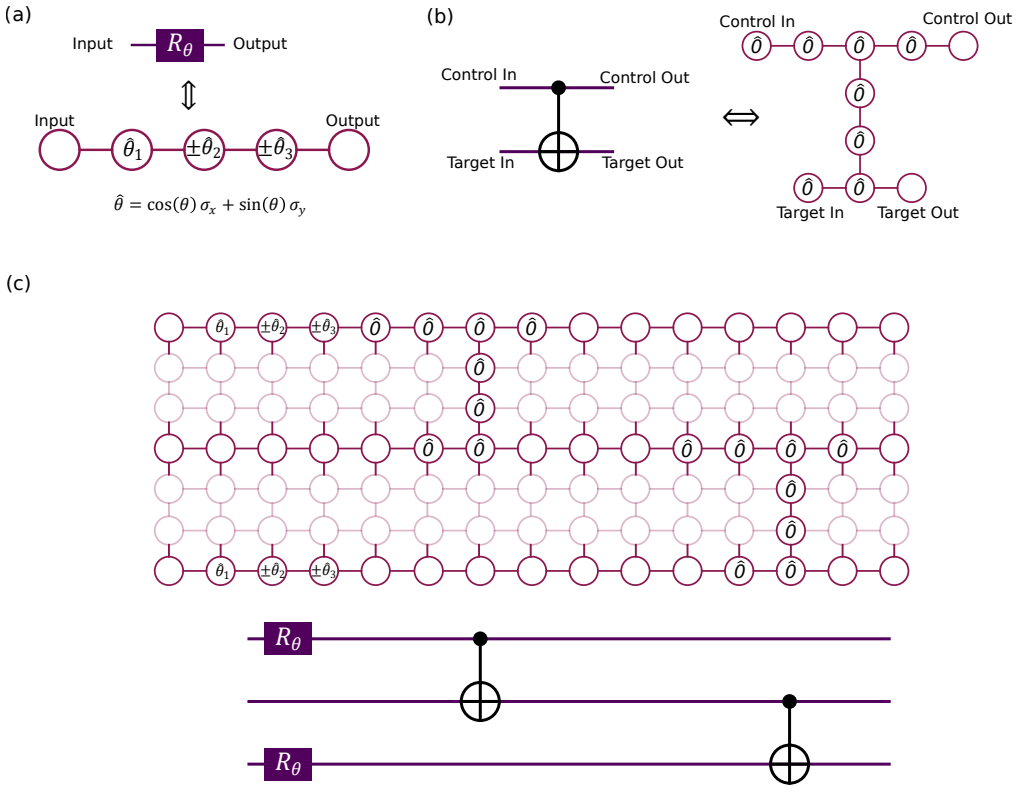

Figure 3.1.1: (a) Single qubit operations are equivalent to measurements in the XY plane of the bloch sphere and feedforward operations depending on previous measurement results. (b) CNOT operations are equivalent to measurements in the X basis of two rows of qubits and a column connecting them. (c) Example of a mapping between a qubit picture quantum circuit and its equivalent computation in a cluster state based MBQC protocol.

The challenge with the MBQC protocol described above is that it requires a very large cluster state in at least 2-dimensions. Protocols to generate cluster states are prone to losses and infidelities, so the success probability for a cluster state decreases

exponentially with the size, making it unfeasible for large scale quantum computations.

Fusion based quantum computation (FBQC) is a different paradigm within MBQC, which instead of requiring a large scale cluster state, relies on small scale entangled resource states[48]. The main difference lies in FBQC including two-qubit measurements, whereas MBQC only makes use of single-qubit measurements. The two-qubit measurements are also called fusions and they are typically applied across resource states in order to generate interconnectivity as illustrated in Figure 3.1.2.

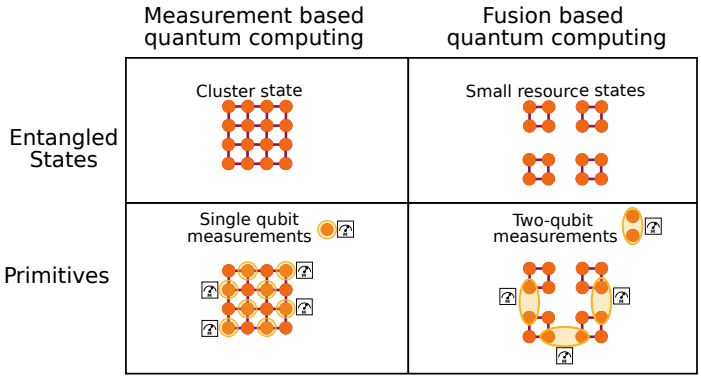

Figure 3.1.2: The original proposal for MBQC was to take a large entangled state called the cluster state as the basis and make use of single qubit measurements as the primitive to replicate quantum computing operations. In FBQC only small resource states are required, but instead of single qubit measurements it uases two-qubit measurements, also known as fusions, as its primitive.

3.2 Theory

3.2.1 Fusion

A fusion is a 2-qubit measurement between qubits that are part of larger entangled states. For dual-rail encoded qubits a fusion is performed using the circuit illustrated in Figure 3.2.1(a). After the circuit the two-photons are measured. The outcome of the measurement will determine whether the fusion was successful, where the success probability in the circuit shown is 50%. A successful fusion heralds entanglement between the resource states that the qubits were connected to, while a failed fusion leaves the states unconnected. The other side of fusion is that it is a two-qubit measurement, meaning that information about the measured qubits is always gained. In the case of a succesful fusion, the outcomes of the X_aX_b and the Z_aZ_b operators are obtained simultaneously, while in the case of a failure only Z_aZ_b are obtained, as illustrated in Figure 3.2.1(b). This information can be used in a similar way as information from single-qubit measurements in MBQC.

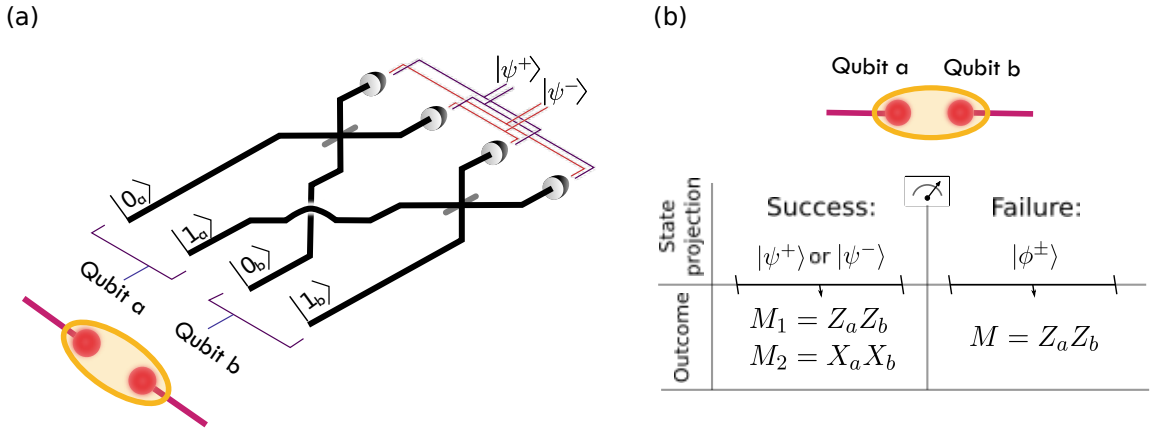

Figure 3.2.1: (a) Fusion circuit in dual rail enconding. Two photonic qubits belonging to larger resource states are interfered in a way that they can herald entanglement between the two resource states. The detection pattern of the photons determines which state is heralded. (b) There are also some detector patterns that do not herald entanglement, these are fusion failure results. In a succesful fusion both the ZZ and the XX information of the qubit pair is obtained, while in a failure only the ZZ is obtained. Figure adapted from [42].

For time bin encoded qubits as shown in Figure 3.2.2(a), a fusion operation can be achieved by simply letting the two qubits interfere on a BS as shown in Figure 3.2.2(b). A successful fusion is obtained when the photons arrive simultaneously in both detectors, as this erases the information of where the photons came from. A succesful fusion can herald the entangled state ψ^+ or ψ^- depending on whether the detection happened on the early or the late time-bin. This is illustrated in Figure 3.2.2(c).

3.2.2 Entanglement generation

Deterministic generation of entangled resource states is essential for the implementation of FBQC. Recent advancements have made it possible to achieve across different platforms and implementations [49, 50, 51]. We use semicondutor quantum dots (QDs) in order to achieve this. In the following subsection we will briefly describe the procedure for entangled resource generation as implemented by Meng et al. [37]. Quantum dots (QDs) in photonic-crystal waveguides (PCWs) act as two level emitters suitable for high quality single-photon sources. The carrier in the QD has a spin, which after adding an in-plane magnetic field (see Figure 3.2.3(a)) creates Zeeman-splitting of the energy levels, resulting in a four level system as shown in Figure 3.2.3(b). The polarization of the diagonal transitions is the opposite as the polarization of the vertical transitions. Since the quantum dot is embedded on a PCW, there is one polarization suppressed by the waveguide and one that is enhanced. For the sample we use for

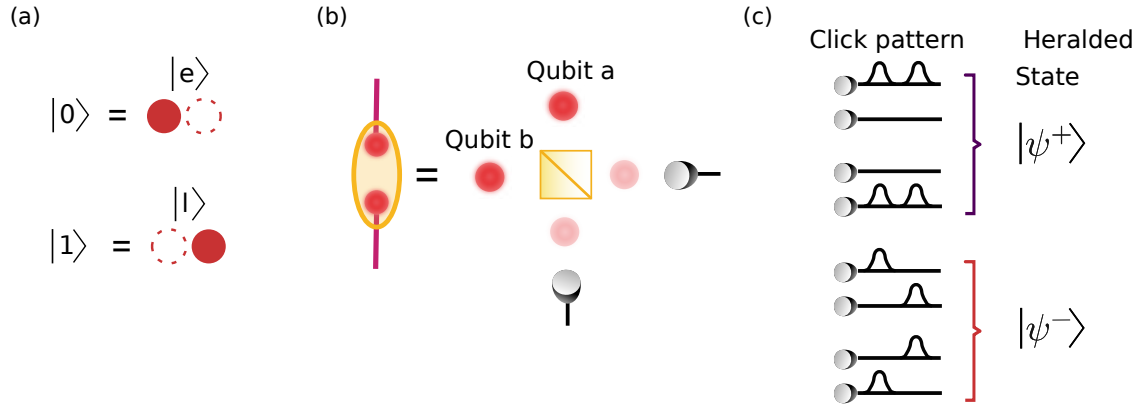

Figure 3.2.2: (a) Time bin encoding of single photons (b) A fusion in time bin enconding can be implemented by having both photons arrive simultaneously at a beam splitter such that the early and late time bins each interfere perfectly. (c) Detector patterns corresponding to succesful fusions in a time-bin enconded fusion experiment. Fusion failure happens when photons bunch into the same time-bin.

this experiment it is the diagonal transitions that are enhanced. The decay rate of the vertical transitions compared to the decay rate of the diagonal transitions is quantified by the cyclicity of the system. In our system we characterized the cyclicity to be [37]

$$C \equiv \frac{\gamma_x}{\gamma_y} = 36 \pm 3\,. \tag{3.2.1}$$

A high cyclicity allows for an efficient initialization procedure where the QD spin can deterministically be set to be in the $|\uparrow\rangle$ state. The procedure is depicted in Figure 3.2.4(a). A pump laser with the frequency of the transition $|\Downarrow\downarrow\uparrow\rangle \rightarrow |\downarrow\rangle$, which we denote Ω_p, is set to continuously drive the system. Because of the fast diagonal decay rate the system will eventually decay into the $|\uparrow\rangle$ state. The characteristic time we can expect the spin to stay at one state is given by the spin flip time T_1, which for our system is in the hundreds of microseconds [37], meaning that we can confidently assume the spin state to be $|\uparrow\rangle$ after initialization for the duration of our experiment.

In order to use the QD as a single photon source we exploit the high decay rate of the transition $|\Uparrow\uparrow\downarrow\rangle \rightarrow |\downarrow\rangle$, such that we excite it using a pulsed laser with optimized pulse duration and intensity to perform a π Rabi oscillation of the transition. The same transition can be used for readout of the spin state. If the spin is in the $|\downarrow\rangle$ state, repeated excitation of this transition will lead to fluorescence which can be measured on a single photon detector. For this we use another pump laser denoted as Ω_e as depicted in Figure 3.2.4(b).

In order to create coherent oscillations between the two spin-ground states we use a third laser, which we denote as the Raman laser Ω_r. This laser is a continuous wave laser that is modulated using an EOM. The modulation creates sidebands as depicted in the left of Figure 3.2.4(c). The two sidebands create Rabi oscillations

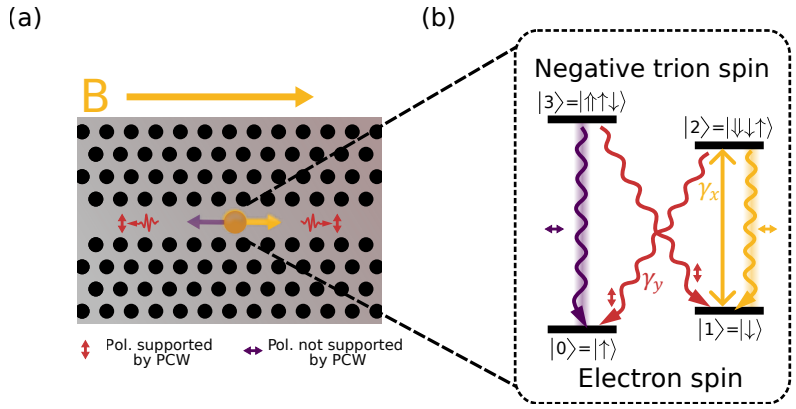

Figure 3.2.3: (a) A QD in a PCW interacts with an external magnetic field B through its spin. (b) Four level-system arising due to the Zeeman splitting of the spin. The diagonal transition have opposite polarization compared to the vertical transitions. In our case only the polarization of the diagonal transitions is enhanced by the waveguide.

between the spin ground states via a shared virtual excited state. The polarization of the driving laser determines if it is the diagonal or the vertical transitions that will be driven. In our case we set the driving laser to have circular polarization, such that it alternates between driving all the four transitions as depicted in the right of figure 3.2.4(c). This alternation results in the spin oscillating coherently between the two ground states. The time we can expect the spin to remain in a given coherent superposition is characterized by the spin coherence time T_2, which for our system is in the order of hundreds of nanoseconds [37].

The spin of a QD electron interacts not only with the external magnetic field but also with the magnetic field of all the nuclear spins in the semiconductor environment. The resulting magneting field from all the nuclear spins is denoted as the Overhauser field, and it induces dephasing by shifting the energy states of the spin transitions. In the left of Figure 3.2.4(d) we depict the electron spin being affected by the nuclear spin bath. It should be noted that the interaction goes both ways, meaning that the state of the nuclear spin ensemble can be controlled through the electron spin [52]. This correspondence can be exploited to narrow the range of states of the nuclear ensemble through interaction with the electron spin, a process which we call nuclear spin narrowing or nuclear spin cooling.

In order to perform nuclear spin narrowing we drive the electron spin simultaneously with Ω_r and Ω_p. The procedure works because the splitting of the energy levels between different microstates of the nuclear ensemble is larger when the electron is in the $|\downarrow\rangle$ state than in the $|\uparrow\rangle$ state, as depicted on the right of Figure 3.2.4(d), where we show Δ_b being larger than Δ_a. If this difference was not there, driving with the Ω_r laser would have the same oscillation strength for going up in the I_z ladder than for going down. But because of the difference, there is a central microstate with collective spin I_z where all microstates with higher spin number would oscillate down the

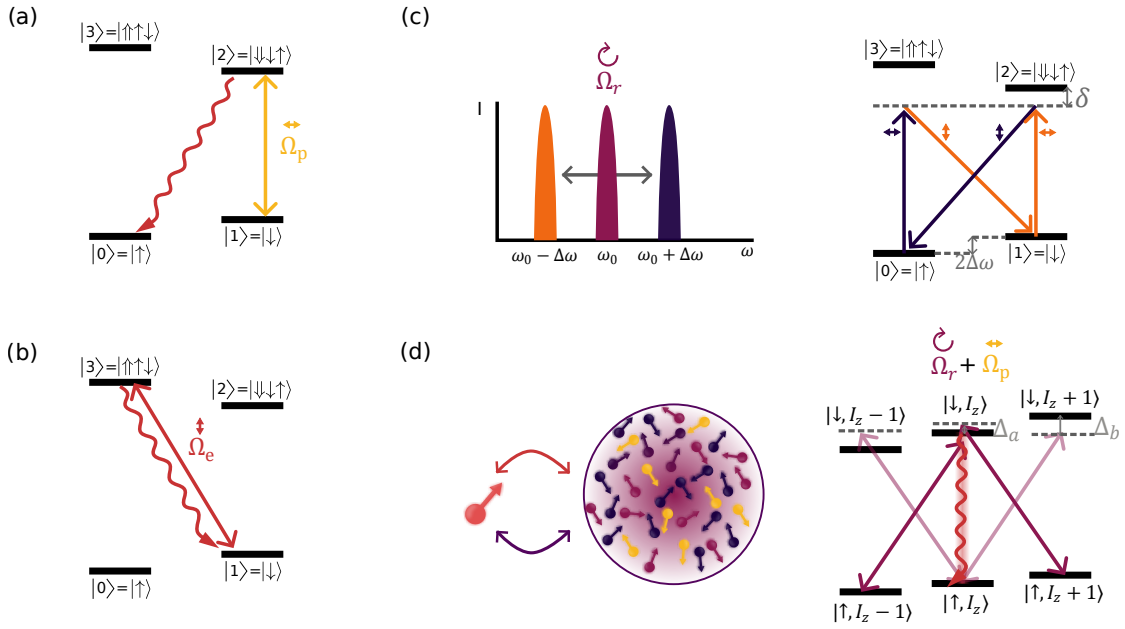

Figure 3.2.4: (a) Initialization of a spin qubit to make sure that it is in the state $|\uparrow\rangle$. (b) Readout procedure which makes use of the diagonal transition. This is the same transition used for photon emission. (c) Procedure to create coherent oscillations between the two spin states. It is based on a modulated laser with circular polarization. Its side bands drive the spin system coherently between its two ground states. (d) Nuclear spin narrowing relying on the interaction between the electron and the nuclear spins. Combining the Raman and the initialization laser results in a process that makes one spin microstate much more likely than all the others.

ladder, and all microstates with lower spin humber will oscillate up the ladder. If we simultaneously add a pump laser that makes the spin constantly decay from an $|\downarrow\rangle$ state to a $|\uparrow\rangle$ state, the spin ensemble is bound to drift towards the central microstate $|I_z\rangle$. Through this procedure, the spread of spin states on the nuclear spin ensemble is bound to be reduced, which in turn reduces the amount of magnetic fields generating dephasing on the electron spin. This procedure increases the spin dephasing time T_2^* from ~ 2 ns to 33(3) ns [37].

The aforementioned processes are combined to create spin-photon entanglement according to the following scheme:

- Nuclear spin narrowing proceeded by optical pumping on $|1\rangle \leftrightarrow |2\rangle$ to initialize in $|0\rangle$.
- Rotation pulse to prepare the spin in $|\psi\rangle = (|0\rangle + |1\rangle)/\sqrt{2}$.
- Early excitation pulse is applied.
- Ground states are flipped.
- Late excitation is applied.

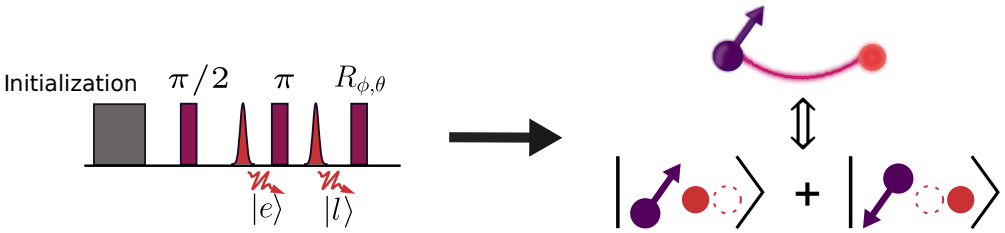

Figure 3.2.5: A pulse sequence as depicted on the left results in deterministic entanglement between the state of the spin and its emitted photon in time-bin enconding.

The spin-photon entanglement process is illustrated in Figure 3.2.5, where the laser pulse sequence is shown. With this sequence, the spin-photon system acquires the state $\left|\psi_{sp}^{-}\right\rangle = (|\uparrow e\rangle - |\downarrow l\rangle)/\sqrt{2}$.

3.2.3 Entanglement fusion

We propose a proof of principle experiment showcasing the fusion of entangled resource states from a QD spin. The process is illustrated in Figure 3.2.6(a) where fusion is used to achieve entanglement of two different quantum dot spins.

The procedure begins with creating two independent spin-photon entangled states, which we denote a and b. The photons are enconded in the time-bin basis, where the

eigenstates are denoted as early $|e\rangle$ or late $|l\rangle$. The joint wavefunction can be written as

$$|\psi_{ab}\rangle = \frac{1}{2}(|0\rangle_a |e_a\rangle - |1\rangle_a |l_a\rangle) \otimes (|0\rangle_b |e_b\rangle - |1\rangle_b |l_b\rangle), \tag{3.2.2}$$

The fusion gate consists of a BS where the two early and late pulses arrive simultaneously. We use a and b to also denote the two input paths of the BS. The state then evolves to

$$|\psi_{cd}\rangle = \frac{1}{4}(|0_a\rangle (|e_c\rangle + i|e_d\rangle) - |1_a\rangle (|l_c\rangle + i|l_d\rangle)) \otimes (|0_b\rangle (i|e_c\rangle + |e_d\rangle) - |1_b\rangle (i|l_c\rangle + |l_d\rangle)), \tag{3.2.3}$$

The state can be written as

$$\begin{aligned} |\psi_{cd}\rangle = \frac{1}{4}(& |0_a 0_b\rangle (i\sqrt{2}|e_c e_c\rangle + i\sqrt{2}|e_d e_d\rangle) \\ & - |0_a 1_b\rangle (i|e_c l_c\rangle + |e_c l_d\rangle - |e_d l_c\rangle + i|e_d l_d\rangle) \\ & - |1_a 0_b\rangle (i|e_c l_c\rangle + |e_d l_c\rangle - |e_c l_d\rangle + i|e_d l_d\rangle) \\ & + |1_a 1_b\rangle (i\sqrt{2}|l_c l_c\rangle + i\sqrt{2}|l_d l_d\rangle)). \end{aligned} \tag{3.2.4}$$

Detecting the two photons in different time-bins heralds the spin-spin state: $\psi_\pm = |0_a 1_b\rangle \pm |1_a 0_b\rangle$:

$$\langle e_c l_d |\psi_{cd}\rangle = \langle e_d l_c |\psi_{cd}\rangle = |\psi_-\rangle \tag{3.2.5}$$

$$\langle e_c l_c |\psi_{cd}\rangle = \langle e_d l_d |\psi_{cd}\rangle = i|\psi_+\rangle . \tag{3.2.6}$$

Here we assume photons in the two resource states a and b are indistinguishable. The probability of heralding ψ_- or ψ_+ is 25%, giving a total fusion success probability of 50%. An important note is that events where indistinguishable photons arrive at the same time-bin but at different detectors are prohibited by the Hong-Ou-Mandel effect. Imperfect indistinguishability would give rise to these events, which projects the state into a mixed state of $\rho(\phi_\pm) = |0_a 0_b\rangle \langle 0_a 0_b| + |1_a 1_b\rangle \langle 1_a 1_b|$.

This process showcases the simplest fusion experiment that can be realized with our platform. Increasing the size of the resource states and the number of emitters opens the path to various FBQC photonic architectures which are suited to the different hardware platforms and optimized for high error thresholds[53, 54, 55, 56].

Interfering entangled photons from multiple quantum dots is a technological challenge yet to be achieved, which makes it unsuitable for a proof of principle experiment. Fusion can though still be showcased through a slightly different experiment, one where instead of generating entanglement between two spins at separate spatial locations, we generate entanglement between a single spin and itself at a different time.

The process is illustrated in figure 3.2.6(b). A QD spin is entangled to a time-bin encoded photon which is sent into an optical delay line. The same spin is reinitialized at a later time and similarly entangled to a second photon. A fusion measurement

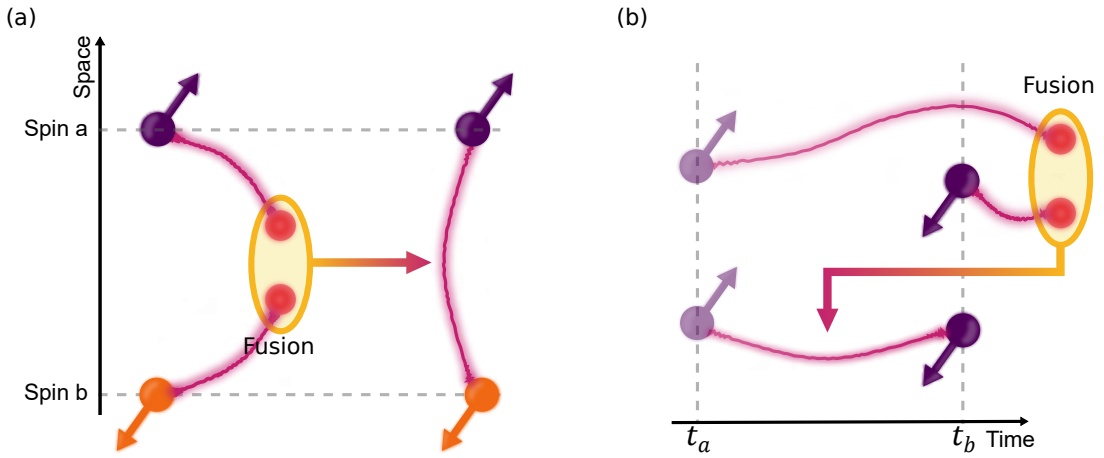

Figure 3.2.6: (a) Fusion in space. A fusion operation between two resource states consisting of two spin each entangled to a different photon result in entanglement between the two spins. (b) Fusion in time. A fusion operation between two resource states consisting of a single spin entangled in two instances in time to two different photons result in entanglement of the spin with itself at the two time instances.

is then performed on both photons, which if successful heralds entanglement between the spin at the two instances in time.

The meaning of entanglement at two instances in time is that upon a successful fusion, any two measurements of the spin at the two specified time instances would exhibit the same correlations of taking the same set of measurements on two spatially separated spins that are entangled. An objection may be made, that the first measurement of the spin would collapse the entanglement between it and the first photon, but it should be noted that a successful fusion deletes the information about which photon corresponds to which spin-time instance, such that coherence can be retrieved like in a quantum eraser experiment.

An important point to be made, is that time-like spin fusion can become an important resource for fusion based quantum computation and not only a proof of principle experiment as we originally expected it to be. The fact that any two measurements to be applied on the time-entangled spin are indistinguishable from any two measurements to be taken on spatially entangled spins means that time-like entanglement can be an equally valid resource for FBQC.

We illustrate our vision in Figure 3.2.7, where resource states generated from different spins are employed to create fusion measurements both with different spins and with themselves at different instances in time. Including the time dimension on a fusion network can have multiple advantages. First it decreases the hardware requirements with respect to the physical number of emitters needed for a given computation[57]. Secondly it may increase the fidelity of the computation as emitters being fused with themselves suffer fewer repercussions due to a generally higher photon indistinguishability between same emitters than between different emitters.

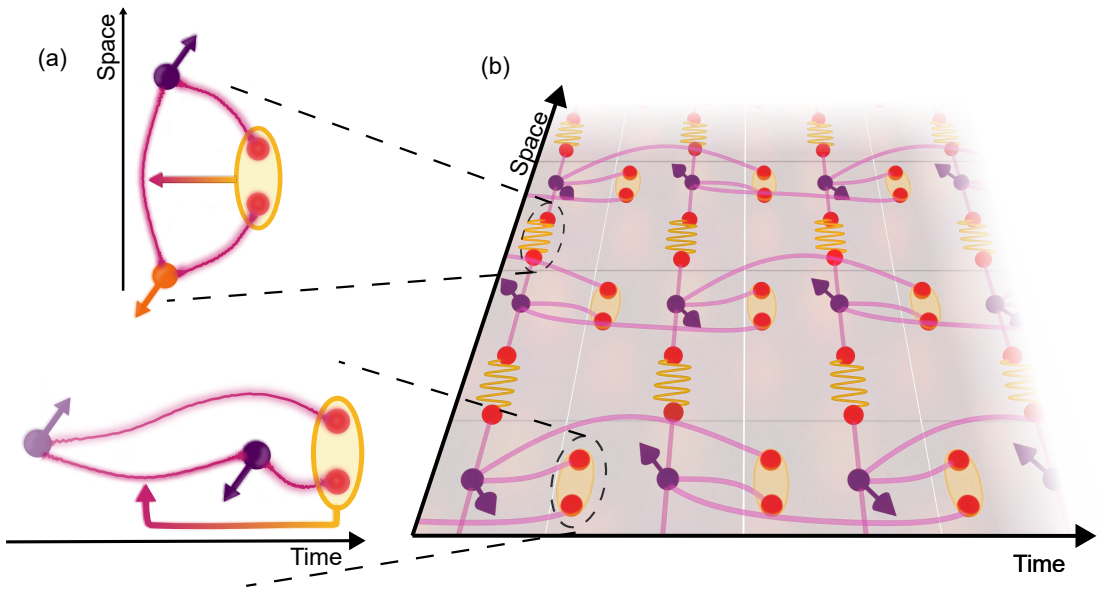

Figure 3.2.7: Fusion network in space and time. Using time-like fusions allows to use time as a dimension in FBQC, significantly reducing the ammount of spins required for a given computation.

On the other hand, the time dimension is not as accessible as the spatial dimensions in a computation, and it may place some limitations on which error correction codes can be used with this architecture. This is a topic that requires further theoretical research in order to be fully understood.

3.3 Experimental setup

A great portion of the text and figures in this section are adapted with minor adjustments from [42]

The experimental setup is outlined in Figure 3.3.1(a,b). It consists of a resource state generation platform, an active delay line and a fusion-gate platform.

The resource state generator is implemented using a spin-photon interface as explained in the previous section. We employ an InGaAs QD that is embedded in a GaAs photonic crystal waveguide (PCW) (see electron microscope image in Figure 3.3.1 (b)). The QD possesses an optical transition at 947.86 nm which is driven resonantly with a laser (Ω_e) for deterministic generation of single photons (yellow excitation in Fig. 3.3.1 (a,b)) with a near-unity collection efficiency into the PCW [58]. The QD is deterministically charged with a single electron spin through a bias voltage and we apply an external magnetic field of 4 T along $+y$ direction (Voigt geometry) to access the two Zeeman spin ground states $|\downarrow\rangle$ and $|\uparrow\rangle$, see Figure 3.3.1(b). Coherent Rabi spin rotations are implemented by driving the QD with an off-resonant Raman

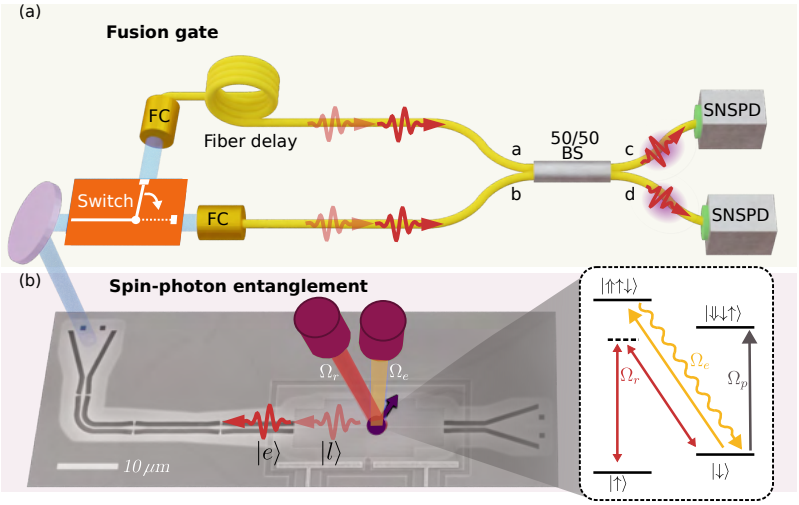

Figure 3.3.1: (a) Fusion gate employed in our experiment. An active switch alternates such that every first photon is sent to a fiber delay and every second photon is sent directly to a fiber beam splitter where they arrive simultaneously. The final part of the gate consists of detection using superconducting-nanowire single-photon detectors (SNSPDs). (b) Spin-photon entanglement generation platform. A QD spin emits photons in a photonic crystal waveguide. The photons make up qubits in time-bin enconding and are entangled to the QD spin through clever use of the driving laser fields. Figure adapted from [42]

laser, which is a bichromatic laser Ω_r. The central frequency of the laser is centered at $\delta = 650$ GHz red-detuning from the optical transition in order to avoid optical excitation or emission from the QD. In advance, the spin coherence time is increased by mitigating the nuclear spin noise bath by implementing optical cooling at the start of each experimental round [37, 52].

The protocol proceeds by implementing the Lindner-Rudolph protocol for spin-photon entanglement [59] as described in the previous section. The photonic qubit is defined by the time bin of the photon, and the spin qubit is defined by the natural orientation of the spin along the direction of the magnetic field. The pulse sequence is shown in Figure 3.4.1(a) and is repeated after 300 ns to generate two separate resource states for the fusion experiment. Including a spin-echo reshaping π-pulse inside the pulse sequence ensures that the protocol is robust towards spin dephasing [60]. Following the nuclear spin narrowing pulse, we perform spin initialization, which consists of resonantly exciting the optical transition with a laser pulse (Ω_p), ensuring that the spin is in the state $|\uparrow\rangle$ at the beginning of the experiment. We then apply the spin-photon entanglement sequence explained in the previous section. Subsequently, the spin state is read out by 200 ns of optical pumping of the diagonal transition $|\downarrow\rangle \rightarrow |\Uparrow\uparrow\downarrow\rangle$, see Figure 3.3.1(b). This procedure leads to photon emission if the spin is in the state $|\downarrow\rangle \equiv |1\rangle$, leading to measuring the spin state in the computational (Pauli Z) basis. To measure the spin state in other Pauli bases, we use a rotating pulse $R_{\phi,\theta}$ at the end

of the resource state generation sequence by using Ω_r. We use two angles on the bloch sphere to specify the basis that is being measured. The angle θ, which describes the direction in the XZ plane, is experimentally determined by the pulse area from the Raman laser. The angle ϕ, which corresponds to the direction in the XY plane, is in turn determined by the phase of the EOM signal used to modulate the Raman laser [61]. The spin is then reinitialized to generate a second resource state and is read out a second time.

The fusion experiment initially generates two separate spin-photon entangled resource states at different instances of time t_a and t_b ($t_b - t_a = 300$ ns), i.e. $|\psi^-\rangle(t_i) = (|0_i\rangle|e_i\rangle - |1_i\rangle|l_i\rangle)/\sqrt{2}$, $i = a, b$. Here the qubit state $|0\rangle$ ($|1\rangle$) corresponds to the $|\uparrow\rangle$ ($|\downarrow\rangle$) spin state, and $|e\rangle$ ($|l\rangle$) denotes the emitted photon occupying the early (late) time-bin. Subsequently, the first photon (labeled a) and the spin readout signal are routed with an electro-optic switch to a single-mode fiber delay matching the 300 ns time difference between the two resource state generation times. The second photon is routed to a single-mode fiber without implementing a delay, resulting in both time-bin photonic qubits arriving simultaneously at a balanced fiber beam splitter (BS), as shown in Figure 3.3.1(a). Photon detection on the output modes is implemented via superconducting-nanowire single-photon detectors (SNSPDs) that resolve the early and late photon arrival times. In this circuit, the two early components $|e_a\rangle$ and $|e_b\rangle$ of the two time-bin qubits interfere at the BS, and the same is the case for the late components $|l_a\rangle$ and $|l_b\rangle$. By identifying $|e_i\rangle$ ($|l_i\rangle$) with $|0_i\rangle$ ($|1_i\rangle$) as the computational state of each time-bin photonic qubit, the implemented scheme corresponds to a time-bin implementation of the photonic fusion circuit in Figure 3.2.1(a). Labelling the two output modes of the BS as c and d (see Fig. 3.3.1(a), the successful fusion outcomes correspond to measuring the two photons in the detection patterns $|e_c l_d\rangle$ and $|e_d l_c\rangle$ for a Bell state projection into ψ^-, and $|e_c l_c\rangle$ and $|e_d l_d\rangle$ for projecting into ψ^+. The remaining detection patterns are associated with fusion failure, i.e. projection of the joint state of the two photons into the subspace spanned by the Bell states $\phi^\pm$.

3.4 Results

A great portion of the text and figures in this section are adapted with minor adjustments from [42] On this experiment we perform a fusion between two photons entangled to a QD spin at different times t_a and t_b and measure the state of the spin at those times in order to probe correlations. Since we collect any light from the QD on the PCW and this is subsequently connected to the fusion gate, the light from the spin readout and the actual photons used for the experiment are measured on the same detector at different times. This means that a successful measurement requires four detector clicks, two from the photons and at least one from each time-instance of the spin. We process the signal from the detector using a time tagger, which is a device that records the arrival times of the electrical signals from the detectors and triggers. Time taggers are usually also equipped to create histograms and correlation measurements of the recorded signals in ream time. An example of a histogram made

from the signal acquired on the time tagger after multiple runs of the experiment is shown on Figure 3.4.1, where we specify what the different signals corrrespond to. It can be observed that the early and late photon pulses for both runs of the experiment arrive at the same time, while the readout signals arrive at separate times in order to be able to distinguish them from each other. From the time tagger signal we proceed

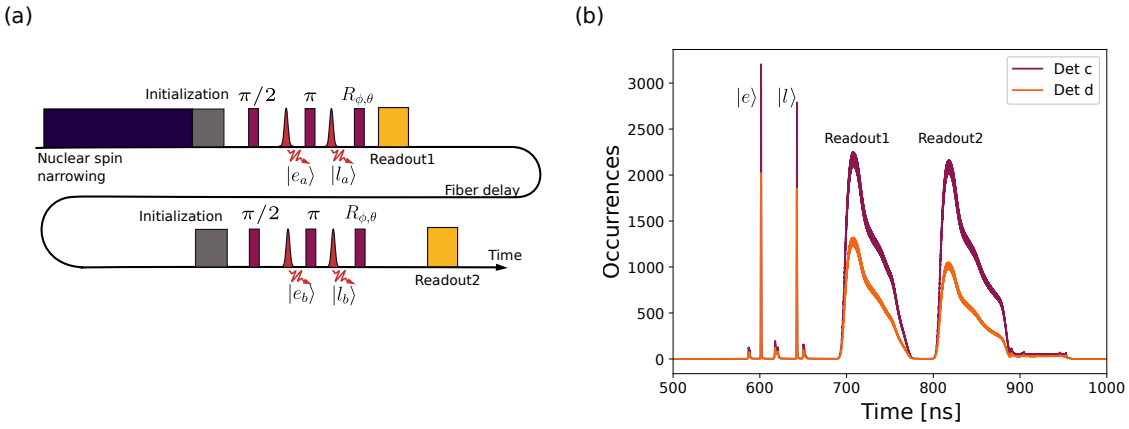

Figure 3.4.1: (a) Pulse sequence of all the lasers used throughout the experiment. (b) Raw histogram of the data obtained on the time-tagger connected to the SNSPDs. Due to the active delay, the arrival time of the first and the second photons overlap with each other and are thus not distinguishable on the histogram. The readouts on the other hand were engineered such that they arrive at different times and can be told apart from each other.

to analyze the data by selecting events where we observed a successful fusion, which depending on the detector pattern should project the state into ψ^+ or ψ^- of the spin at two instances in time. We perform data analysis to verify that those are indeed the generated states. The proper way to verify a multi-qubit state is through state tomography, where the two qubits are measured in all possible basis combinations. This requires a lengthy measurement which would have been challenging with the coincidence rates described above. Instead we directly measure the fidelity of the states through their relevant stabilizers.

The states $\psi^{\pm}$ are stabilized by the joint Pauli operators $-ZZ$, $\pm XX$, and $\pm YY$, which means they are eigenstates with eigenvalue $+1$ for their respective operator [62]. Based on this we take qubit measurements in the basis pairs ZZ, XX and YY in order to evaluate the states. In every basis there are 4 possible 2-qubit configurations, $|\uparrow_a\uparrow_b\rangle$, $|\downarrow_a\uparrow_b\rangle$, $|\uparrow_a\downarrow_b\rangle$, $|\downarrow_a\downarrow_b\rangle$. The state ψ^- remains unchanged when projected with the XX and YY Pauli operators, while the state ψ^+ behaves as the state ϕ^- when projected with XX and as ϕ^+ when projected with the YY operator. Our experiment proceeds to measure through all the 4 configurations for each basis pair, giving a total of 12 different measurement settings per run. We sample through many runs of the experiment over multiple days of integration time in order to decrease the statistical

uncertainty of our measurements.

The measured correlations between the spin qubits for the ZZ, XX, and YY Pauli operators conditioned on successful fusion outcomes $\psi^{\pm}$ are shown in Figure 3.4.2(a). These measurements can be used to calculate the fidelity with the target state by comparing the overlap according to the equation

$$\begin{aligned}\mathcal{F}^{+} &= Tr\left\{\rho_{exp}\left|\psi^{+}\right\rangle\left\langle\psi^{+}\right|\right\} \\ &= Tr\left\{\frac{\rho_{exp}\mathbb{1} - \rho_{exp}ZZ + \rho_{exp}XX + \rho_{exp}YY}{4}\right\} = \frac{1 - \langle ZZ\rangle + \langle XX\rangle + \langle YY\rangle}{4},\end{aligned} \tag{3.4.1}$$

and similarly

$$\mathcal{F}^{-} = \frac{1 - \langle ZZ\rangle - \langle XX\rangle - \langle YY\rangle}{4}, \tag{3.4.2}$$

where we calculate the expectation values as

$$\langle ZZ\rangle = \frac{(N_{0,0} + N_{1,1} - N_{1,0} - N_{0,1})}{(N_{0,0} + N_{1,1} + N_{1,0} + N_{0,1})}, \tag{3.4.3}$$

$$\langle XX\rangle = \frac{(N_{+,+} + N_{-,-} - N_{+,-} - N_{-,+})}{(N_{+,+} + N_{-,-} + N_{+,-} + N_{-,+})}, \tag{3.4.4}$$

$$\langle YY\rangle = \frac{(N_{+_i,+_i} + N_{-_i,-_i} - N_{+_i,-_i} - N_{-_i,+_i})}{(N_{+_i,+_i} + N_{-_i,-_i} + N_{+_i,-_i} + N_{-_i,+_i})}. \tag{3.4.5}$$

We find $\mathcal{F} = 0.59(3)$ when conditioning on the fusion outcome ψ^{+} and $\mathcal{F} = 0.58(3)$ when conditioning on ψ^{-}. Both cases are significantly above the 50% bound, indicating genuine spin qubit entanglement. Upon fusion failure ($\phi^{\pm}$ projection), the ZZ fusion outcome is still obtained but the XX and YY outcomes are erased. This results in the generation of perfect correlations between the spin qubits only in the ZZ basis (with expectation value $+1$), but no correlations in the XX and YY bases. Thus the ZZ measurement is only affected by classical error sources, but the XX and YY measurements are sentitive to the spin-photon entanglement quality. An important metric to benchmark the functionality of fusion operations in a network is the noise rate of the fusion outcomes, i.e., the rate with which the erroneous results are obtained in the parity checks [63]. Due to the correspondence between the fusion outcome and the joint spin state described above, the error rates in a Pauli operator associated with a fusion outcome can be probed by analyzing the error rates in the same operator but on the spin qubits. Note, however, that estimating fusion error rates through the spin states introduces additional imperfections due to noises (e.g. rotation and readout errors) in the spin system. The obtained error rates should therefore be considered upper bounds on the intrinsic performance of the photonic fusion gate. Expectation values for the ZZ, XX, and YY spin operators conditioned on the successful fusion outcomes $\psi^{\pm}$ are reported in Figure 3.4.2(b).

For the ψ^{+} fusions, the corresponding error rates are 18(3)%, 31(2)%, and 33(2)% for ZZ, XX, and YY, respectively, and conditioning on ψ^{-} leads to 19(2)%, 33(2)%,

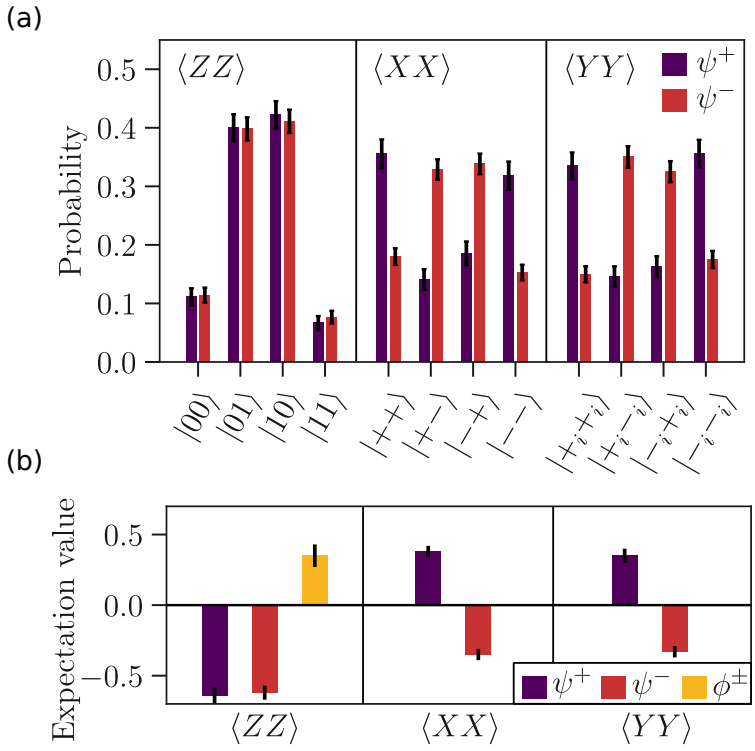

Figure 3.4.2: (a) Histogram representing the probability of the spin to be on different states at the two measurement time instances conditioned on a succesful herald click pattern on the detectors. (b) Expectation value calculated from the measured results in the different bases. Figure reproduced from [42].

33(2)%. In the same figure, we also report the ZZ expectation value conditioned on the fusion failure outcome $\phi^{\pm}$, obtained from detection patterns with both photons detected in either the early or the late time bin. The XX and YY operators are erased in this failure case and thus not reported. These events have a higher contribution from residual background photons, resulting in a higher ZZ error rate of 32(4)%.

In the appendix for this chapter we report an analysis of physical mechanisms that contribute to the error rates. We show that a large portion of the noise budget is expected to arise from spin noise and excitation of transitions different from the desired ones.

At the current state of our experiment, the collection efficiency of the emitted photons is of about 1%, which is the probability of an excitation pulse resulting in a click on our detectors. This is a severe limitation for our experiment making the data acquisition require multiple days in order to achieve statistically significant results. This limitation also made it impossible for us to explore fusion of larger resource states, even though they can be readily generated using the spin-photon entanglement protocol described here [37]. Nonetheless, this is not a fundamental limitation of our platform, as

much higher collection efficiencies have been achieved [64], and recent advancements in heterogeneous integration between the resource state generation platform in GaAs and fusion-capable photonic integrated circuits in SiN [65] suggest negligible coupling loses between the two platforms. We will be exploring the idea of using photonic integrated circuits for fusion in depth in the next chapter.

It is also possible to extract the indistinguishability of the emitted photons from the data collected in our experiment. If the photons were completely indistinguishable we would expect no coincidence counts on the detectors on the same time bin due to the Hong-Ou-Mandel (HOM) effect [66]. We can thus compare the same-time-bin coincidences to the different-time-bin coincidences in order to extract the indistinguishability of the photons. We calculate the HOM visibility according to the equation

$$V_{\mathrm{HOM}} = 1 - \frac{P_{\mathrm{same}}}{P_{\mathrm{diff}}}\,, \tag{3.4.6}$$

for which we achieve a HOM visibility of 67%. This is quite a low visibility, specially since the same setup achieved a visibility above 80% for photons emitted subsequently [37]. This suggests that the delay line was not perfectly adjusted, causing extra distinguishability. A proper alignment of the delay line is required to ensure perfect temporal overlap of the two early (late) pulses, which can be done through classical visibility measurement using a picosecond pulsed laser. Nevertheless, since the heralding of spin entangled states only requires photons that arrive on different time bins (as illustrated in Figure 3.2.2(c)), we do not expect photonic indistinguishability to have a considerable effect on the fidelity of the generated entangled state. Routes to further improvement of the experimental performance have been discussed in detail in Ref. [37].

3.5 Concluding remarks and outlook

In this chapter we demonstrated a first proof of principle experiment showcasing the fusion of two deterministically generated resource states from a solid state emitter. We explore a novel approach to fusion operations where instead of fusing resource states from spatially distributed emitters we use time-multiplexing of the same emitter, resulting in what we call time-like fusion. A fusion of this type has the curious consequence that it heralds an entangled state of the emitter with itself at a different time.

We generate the time-entangled Bell states $\psi^{\pm}$ of a QD spin with itself at a separate instance in time. By measuring the state of the spin at the two different time instances upon a successful fusion we can evaluate the state that is generated. We measure fidelities that are at least three standard deviations above the classical limit for both of the Bell states. Given that we observe with high certainty the correlations proper for a Bell state, we evaluate that we succesfully executed a time-like fusion.

Time-like fusion operations path the way to including the time-dimension in fusion based quantum computation, a trick that can significantly reduce the number of

emitters required for a given computation.

Future directions from this work could be the construction of larger time-like fusion networks and the employment of ancillary entangled states to decrease the fusion-error rate. All of these directions require high efficiency of the photon emission and collection process, and their up-scaling requires interface with increasingly complex photonic circuits in order to realize the necessary fusion operations. In the next chapter we will describe our advances on increasing the efficiency of our single photon emitters, and routes to perform complex quantum information processing through photonic integrated circuits.

Chapter 4

Integrated Photonics Fusion

In this chapter we present our work with Silicon Nitride photonic integrated circuits and describe how we used them for a path-encoded fusion experiment.

Statement of work

The experimental work described in this section was performed in close collaboration with Ying Wang and Stefano Paesani. The design and fabrication of the silicon nitride chip was conducted by Fabian Ruf and his colleagues from Aarhus university. Ying Wang fabricated and operated the QD single-photon source. Patrik Sund and Kasper Nielsen built the two-mode demultiplexer. Stefano Paesani created the code used for some of the data analysis. The author of this thesis was responsible for characterizing and operating the photonic integrated circuits and setting the experiment together. The work described in this chapter resulted in a manuscript specified in [64]. Some of the figures as well as the description of the experiment were adapted with adjustments from that manuscript.

4.1 Introduction

In the previous chapter we described a method to perform fusion-based quantum computing using a quantum dot (QD) spin and free-space optics. A different approach to fusion based quantum computing is one where the QD is only used to produce single photons [67, 68] but does not participate in any of the subsequent operations. A pure photonic quantum computer can be built by applying linear and non-linear entangling operations to single photon states [69, 70, 71]. One promising route for applying these operations is to use photonic integrated circuits (PICs) to create any type of linear operations, and combine them with measurement based non-linearities for the entangling operations. In this chapter we modularly interface a deterministic single photon source, with PICs and single-photon detectors using fibers, showcasing some of the essential building blocks for photonic quantum computing.

(a)

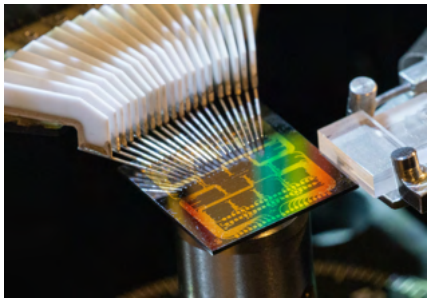

(b)

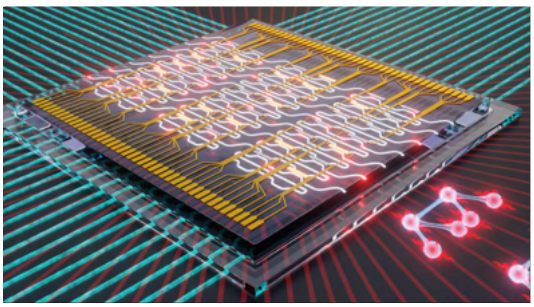

Figure 4.1.1: (a) Photonic chip interfaced with electrical contacts and optical fiber array. Photo taken by Julian C. Robinson-Tait and published in [64]. (b) Example of a large PIC with multiple electrical contacts and waveguides, capable of creating multi-photon entangled states. Figure reproduced from [17].

4.1.1 Photonic-integrated circuits

Optical components

PICs are defined as devices containing two or more functioning optical components integrated on a chip. They are widely used for technological applications within classical information ranging from telecommunications to ultra-fast information processing [72, 73, 74, 75, 76]. A photo of a photonic microchip is shown in Figure 4.1.1(a) and an example of a large PIC is shown in (b).

A universal interferometer can be constructed out of only three components: waveguides, phaseshifters and 50:50 beam splitters (BSs). Waveguides are easily implemented by a defined geometry confining optical modes.

Phaseshifters can be implemented in different ways. The way we employ for the work described in this thesis makes use of the thermo-optic effect, where a local heating of the material induces a refractive index change in the waveguides, resulting in a phase change.

Relying on the thermo-optic effect is slow and excludes cryostatic compatibility. An alternative is to use the electro-optic effect, which is present in certain material platforms, to allow for fast modulation and cryostatic compatibility.

BSs can be implemented on-chip by using directional couplers, which consist of waveguides that are brought very close to each other, such that the electric field is evanescently coupled between the two. The splitting ratio can be controlled depending on the interaction length of the waveguides.

Optical platforms

The field of integrated photonics is new compared to for example the field of integrated electronics, and there is no standardized material platform used to fabricate photonic microchips, as different materials have different advantages and disadvantages.

Silicon nitride (SiN) is a material platform which is compatible with complementary metal–oxide–semiconductor (CMOS) processes, which is the technology used for fabrication of semi-conductor integrated circuits. Its fabrication can therefore make use of the many advancements provided by the electronics industry, allowing for efficient and scalable fabrication of complex PICs. In SiN PICs, ultra low loss propagation [77], and compatibility with and multitude of optical components [78, 79] have been shown. SiN is particularly suitable for interface with QDs as its transparency region includes near-infrared wavelengths from 900 nm and above. For these reasons we choose SiN as a platform to conduct first proof-of-principle experiments of interface between QDs and PICs, which is the main focus of this chapter.

It is important to mention that in chapter 6 we showcase an experiment based on a slightly different material platform, that of silicon-on-insulator (SOI) [80]. This platform is also CMOS compatible and has the advantage that its higher refractive index allows for waveguides bends with a lower radius, making the footprint of photonic circuits lower. Its disadvantage is that it is not transparent at our QD wavelengths, requiring frequency conversion. A weakness of both of these platforms is their lack of electro-optic effect, which makes fast modulation on them challenging to accomplish.

Platform integration

Given that different optical platforms exhibit very different advantages and disadvantages in their applications on photonic quantum information processing, it may be advantageous to use multiple platforms simultaneously.

In this thesis we make use of modular integration, where different building blocks are interconnected through optical fibers. This approach has the advantage that the different building blocks do not need to be temperature compatible as it allows for different platforms operating at different temperatures. The disadvantage is that coupling in and out of a chip leads to losses, limiting the efficiency of the setup. In this chapter we present a modular experiment, where a GaAs chip generates single photons in a cryostat, which are coupled off-chip and transported through optical fibers to a SiN PIC [17].

Another way to integrate multiple platforms is through on-chip heterogeneous integration, where various building blocks on different materials are fabricated on a single chip, minimizing coupling losses between the blocks. As efficient quantum computing requires minimizing system losses, such an approach is imperative for future quantum photonic technologies. There are already multiple advances in integrating GaAs and SiN PICs [81, 82, 83, 84], suggesting that the experiment described in this chapter may be executed on heterogeneously integrated platforms in the near future.

4.1.2 Single-photon operation with PICs

Even though PIC technologies are rapidly advancing, their interface with single photons is not yet well established. We now present some simple experiments that are

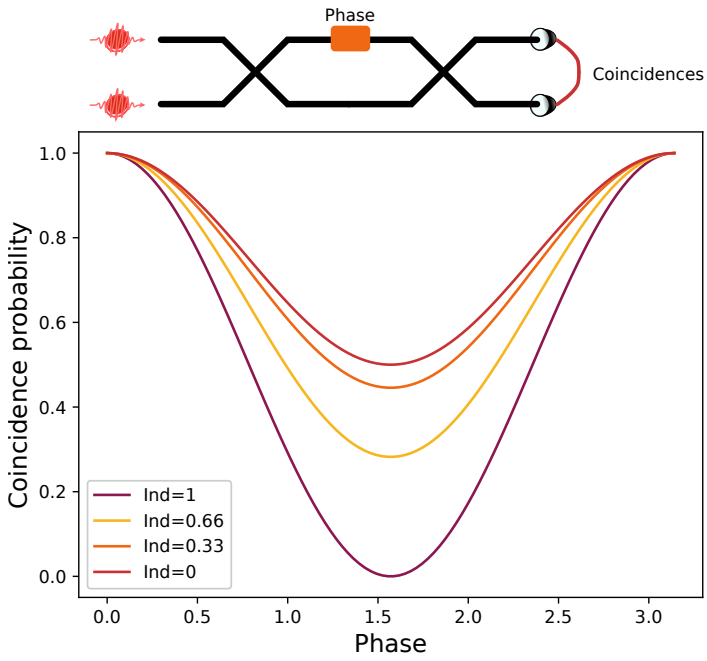

Figure 4.1.2: Simulation of a phase scan on a MZI can for different photonic indistinguishabilities. This measurement can be used to probe the indistinguishability of single photons and thus constitutes a simple way to make an on-chip HOM experiment. The visibility of the curve is directly proportional to the indistinguishability of the photons.

compatible with our PIC in order to test the suitability of the platform for quantum information processing.

On chip quantum interference. Hong-Ou-Mandel (HOM) interference [66], is the simplest form of quantum interference, where two indistinguishable photons interfere on a BS. It serves as a foundational principle for photonic quantum computing and is thus an essential first step for on-chip quantum information processing. A method to evaluate the degree of on-chip HOM interference is shown in Figure 4.1.2, which makes use of an MZI interferometer consisting of two 50/50 beamsplitters with a phaseshifter in the between. The two outputs intensity correlation is simulated as a function of the phase various for different input photon distinguishabilities, which correspond to different curves in Figure 4.1.2. The maximal visibility is achieved for the input photons of fully indistinguishable, and the actual indistinguishability of the photons can be extracted from the visibility of the curves[85].

Probabilistic Bell-state. More complex experiments can be realized by extending the PICs with more modes. For example, a 4 modes PIC can be used to generate post-selected entanglement states. The interferometer required for such an experiment is illustrated in Figure 4.1.3(a). Two photons sent into the first and third input arm of the interferometer will exhibit a superposition that if post-selected in the qubit basis

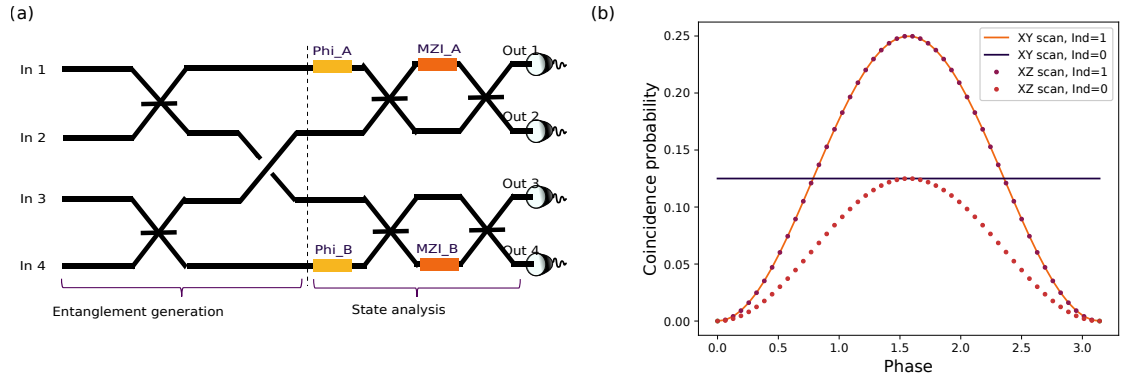

Figure 4.1.3: (a) A PIC designed for a probabilistic Bell-state generation experiment. Four modes are used to encode two qubits with one photon in each mode pair. The first half generates an entangled state if outcomes that do not form qubits are thrown away. The second half is used to analyze the state by measuring each qubit in all possible basis depending on the phase given to the phaseshifters. (b) Expected measurement results for different bases of a Bell-state $|\psi^-\rangle$. The Y axis is the probability of getting the state $|00\rangle$, which corresponds to coincidences in detectors 1 and 3.

(one photon in each mode pair) will be equivalent to a Bell state of entangled qubits in path encoding. This will happen with a success probability of 50%. In a proof of principle experiment the generated state has to be verified, which can be done by adding a universal 2-mode gate at the end of each qubit, which facilitates measurement in any desired basis.

The post-selected entangled state depends on the specific phase-shift implemented by the BSs. In our case we generate the state ψ^+. The expected coincidence probability for the outcome $|00\rangle$ in different basises and for different indistinguishabilities are illustrated in Figure 4.1.3(b).

Heralded entanglement generation The scheme described above has the disadvantage that it is probabilistic, such that failures cannot be corrected. The ideal is to generate entanglement deterministically, however, this is not feasible with linear optics alone, as it necessitates direct photon-photon interactions. A compromise can be realized by using measurement-based non-linearities, which enable the probabilistic generation of the entangled states in a heralded manner. Heralded entanglement generation of N photons happens by interfering $2N$ photons in a linear interferometer with $4N$ modes and taking measurements on a subset of them.

The interferometer required to generate a heralded Bell state is shown in Figure 4.1.4(a), where interference of 4 photons and a detection of two of them heralds a state that depends on the detector click pattern. The scheme has a success probability of 1/8. An proof of principle experiment to test this scheme should a universal unitary on the two output qubits in order to verify the generated state, as shown in Figure 4.1.4(a).

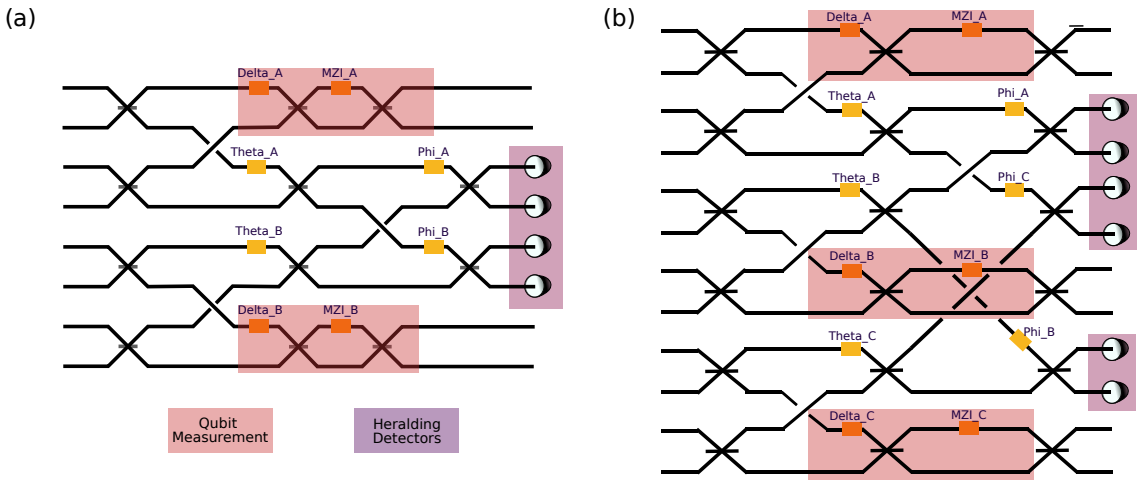

Figure 4.1.4: (a) Photonic circuit for a heralded Bell-state generation. Four photons are sent, one on each mode pair at the input. One click on each of the mode pairs at the center of the interferometer heralds entanglement betweent he two remaining photons. The red areas are for qubit analysis of the generated state. The phases Theta and Phi can be used to control which Bell state will be generated. (b) Photonic circuit for a heralded 3-photon GHZ state generation. Six photons are sent, one on each mode pair at the input. In this case there is only one acceptable state to generate, so photons have to click on the upper output of each heralding mode pair and the phases Theta and Phi are set to zero.

Similarly a 3 photon GHZ state can be generated using the interferometer shown in Figure 4.1.4(b), with a success probability of 1/128. The success probability is lower both because of the size of the interferometer but also because there is only one state that we are interested in. The generated state can similarly be analyzed through quantum state tomography by taking simultaneous single-qubit measurements.

Bosonic suppression laws The HOM effect predicts that if two indistinguishable photons interfere on a BS, the photons will always bunch on either side of the BS. In other words, the state that would result in coincidences between the two output modes of the BS is effectively suppressed. In this case there are two photons in two modes, but the experiment can be generalized for n photons in m modes whenever a discrete Fourier transform is applied (DFT), for which certain input and output combinations will show suppression and others will show enhancement. This is called the bosonic suppression laws.

A DFT of size m is a unitary transformation characterized by the following matrix

$$U_{l,q}^{Fou} = \frac{1}{\sqrt{m}} \exp\left(i\frac{2\pi(l-1)(q-1)}{m}\right), \tag{4.1.1}$$

which corresponds to an interferometer having m modes which has the property that any single photon going into one of the inputs, will have an equal probability of going

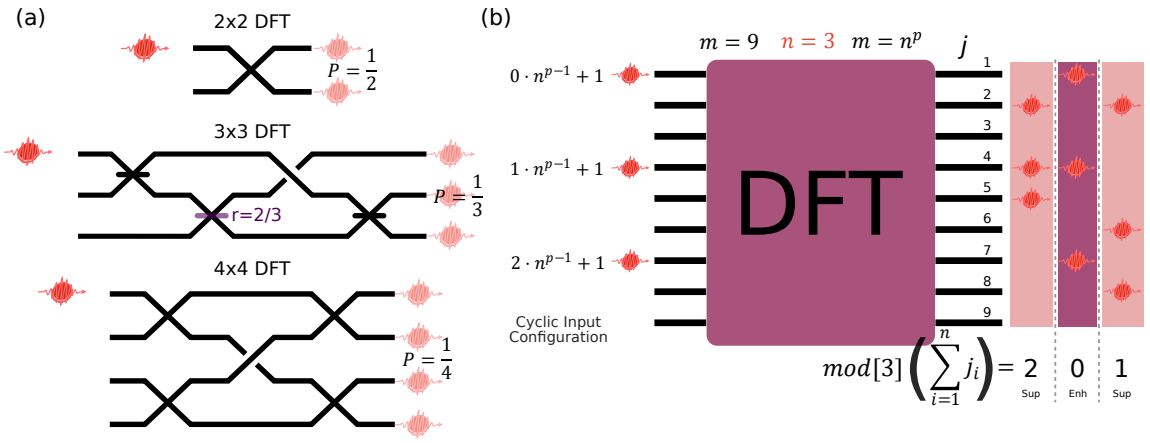

Figure 4.1.5: (a) Illustration of discrete Fourier transform (DFT) interferometers. (b) Example of bosonic suppression laws for an interferometer with 3 photons in 9 modes. Given a cyclic input configuration there will be certain output combinations that will be suppresed such that no coincidences will be detected in them.

out of any of the outputs. Examples of DFT interferometers of size 2,3 and 4 are illustrated in Figure 4.1.5(a).

Let us consider a DFT interferometer of size m used for an n photon experiment such that $m = n^p$ where p is an integer greater than 1. We define a cyclic input configuration as the following

$$j_{cyc} = (1, n^{p-1} + 1, 2n^{p-1} + 1, \ldots, (n-1)n^{p-1} + 1)\,. \tag{4.1.2}$$

The bosonic suppression laws state that whenever a cyclic input configuration of single photons is fed into a DFT interferometer, there will be suppression in the mode conbinations $j_1, j_2, \ldots, j_n$ that fulfill the following condition

$$\mathrm{mod}[n]\left(\sum_{i=1}^{n} j_i\right) \neq 0\,, \tag{4.1.3}$$

and enhancement anywhere else [86]. An example case for $m = 9$ with $n = 3$ is illustrated in Figure 4.1.5(b), where two examples of a suppresed mode combination are shown (highlighted in red) together with an example of an enhanced combination (highlighted in purple). This type of circuit finds broad use in photonic quantum information processing [87, 88, 89, 90, 91].

4.2 Experimental setup

Our experimental setup consists of a QD SPS which generates a stream of single photons. The photons route into pairs of simultaneous photons using a free space

demultiplexer. The photon-pairs are processed on a SiN PIC, after which they are detected using superconducting-nanowire single-photon detectors (SNSPDs). This is illustrated on Figure 4.2.1, where the modular nature of our approach becomes clear.

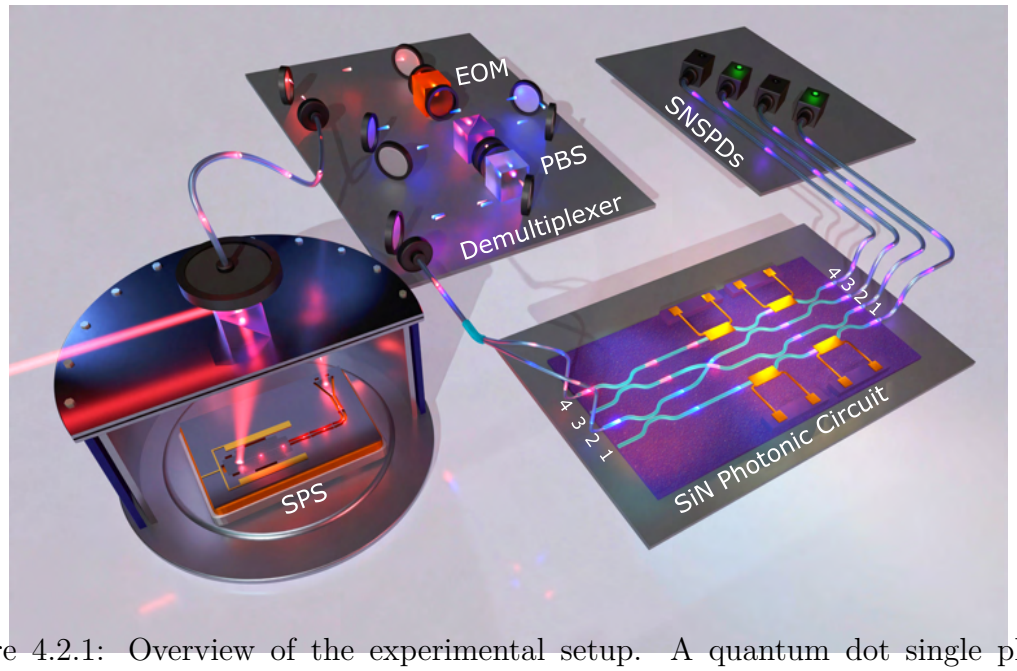

Figure 4.2.1: Overview of the experimental setup. A quantum dot single photon source (SPS) is used to generate single photons from a cryostat. They are demmultiplexed in to two simultaneous photons using a free space electro-optic modulator (EOM) and optics. The photons interfere in a SiN PIC to create probabilistic entanglement. The entanglement is verified by measuring the photons in different basis using superconducting-nanowire single-photon detectors (SNSPDs). Figure reproduced from [64].

4.2.1 Single Photon Source

The single photon source is generated using solid-state quantum emitter of self-assembled InAs QD, which is grown using molecular beam epitaxy (MBE) method. Figure 4.2.2 displays the material structure where a distributed-Bragg reflector (DBR) mirror, a sacrificial layer (SL) and photonic membrane (MB) sequentially deposited on a GaAs substrate from bottom to top. The QDs are illustrated as purple domes in figure 4.2.2 inserted in the middle of the MB. To quench the free charge noise imposing on the QD in this type of the solid state platform, a p-i-n heterostructure designed to implement the electrical gate [92, 93].

To control light-matter interactions and define the direction of emitted photons, an integrated photonic circuit, as illustrated in Figure 4.2.3 (a), is utilized for single-photon generation. The photonic crystal waveguide (PCW) is designed to engineer the optical mode density for the quantum dot (QD)[94], while the shallow etched grating

(SEG) directs the emitted photons from the chip into free space in a predetermined direction, ensuring high collection efficiency. This fabrication is realized via a soft-mask-based technique, where a polymer is used to create the mask necessary for the etching of photonic structures [95].

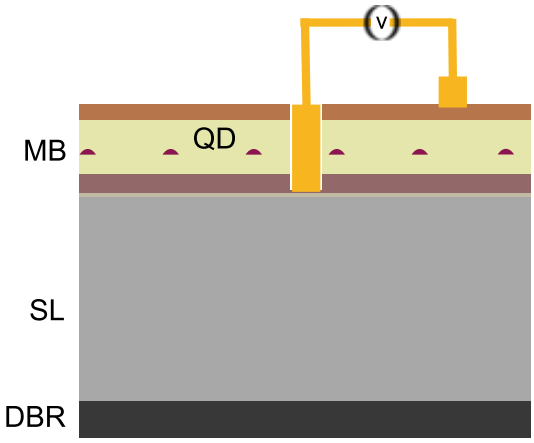

Figure 4.2.2: Layout of the materials in the platform and placement of the Ohmic contacts for electrical tuning of the QD. Figure reproduced from the suplementary material of [64].

A first step when characterizing our photonic devices is to place them on a PCB and test their electrical response through the wiring in the cryostat. The I-V curve of our p-i-n diode is reported in Figure 4.2.3(b) [96], which follows the expected behavior for a p-i-n junction, showing a vanishing low current at low voltages. For voltages above a threshold bias ($\simeq$ 0.8 V) the current increases exponentially. The range of bias voltages that activate neutral excitons, highlighted in red in Figure 4.2.3(b), corresponds to a current of a few μA.

Neutral exciton characterization

For this source we use the neutral exciton of the QD, given that their fast decay rate is suitable for SPS operation. More information about the different decay schemes of a QD can be found in Chapter 2. The single-sided PCW used to obtain single photons is shown in Figure 4.2.3 (a), QDs are targeted in the slow-light region [16] (highlighted by purple). In this region the closer the QD emission frequency is to the bandedge, the stronger the light-matter interaction becomes [29, 14]. The slow-light region width is 15 μm, which ensures enough area to find ideal QDs candidates. The QD we employed in this experiment is spatially located approximately at the center of the PCW along the propagation direction. The distance between the excitation spot and the collection SEG is around 60 μm, as can be observed in Figure 4.2.3(a).

The resonance condition for exciting a QD with a laser depends on the frequency of the laser and the bias voltage applied to the p-i-n junction. For a given voltage within

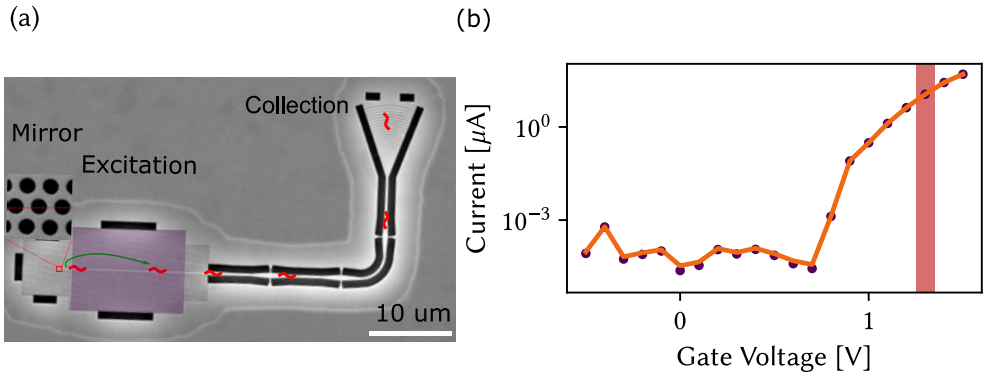

Figure 4.2.3: (a) Scanning electron microscope (SEM) image of the photonic crystal waveguide where one side is terminated by a row of holes shown in the zoomed-in SEM image. (b) The p-i-n diode behavior when applying an external DC bias at the cryogenic temperature of 1.6 K. The orange area is the bias required for the population of the neutral exciton. The corresponding currents are in the range of approximately 1-10 μA. Figure adapted from [64].

the activating region, it is always possible to find a laser wavelength that excites the dot. To find this region and its corresponding wavelengths, we perform a charge plateau measurement, and the results can be seen in Figure 4.2.4(a).

The signal-to-noise ratio (SNR) of single photons to scattered laser noise serves as a metric to evaluate the extent of laser noise pollution, highly useful for alignment of the excitation laser to the QD. The SNR is measured by switching on and off the applied voltage in the presence of the excitation laser. It can have slight variations depending on the wavelength of the laser, and after optimization of the beam spot it can be measured together with the charge plateau measurement as shown in Figure 4.2.4(b). We observed an SNR as high as 10^4, which we achieved by optimizing the excitation beam spot position and polarization. It is also made possible thanks to the significant distance between the excitation and collection spots, which reduces the scattered laser light into the collection. With an SNR as high as the one we observed, we can assume that most of the multi-photon component in the QD comes from re-excitation of the quantum dot during a pulse.

There are two lines in both Figures 4.2.4(a) and (b). These correspond the two different dipoles of the neutral exciton which arise due to fine structure splitting. A cut at a frequency of Figure 4.2.4(a) gives data as shown in Figure 4.2.4 (c), where the separation in frequency between the dipoles is $5.88\,GHz$, and we can observe from the count rate that the left dipole coupling slightly better to the PCW than the right one. We optimized the excitation pulse length using a 4f grating system [26] to effectively stretch the length of the pulses from ≈ 5 ps to about ≈ 30 ps.

The left and right dipoles are orthogonally polarized and as such it is possible to selectively populate them by tuning the laser polarization. We measured the lifetime of the left dipole by comparing the arrival time of single photons to a trigger signal

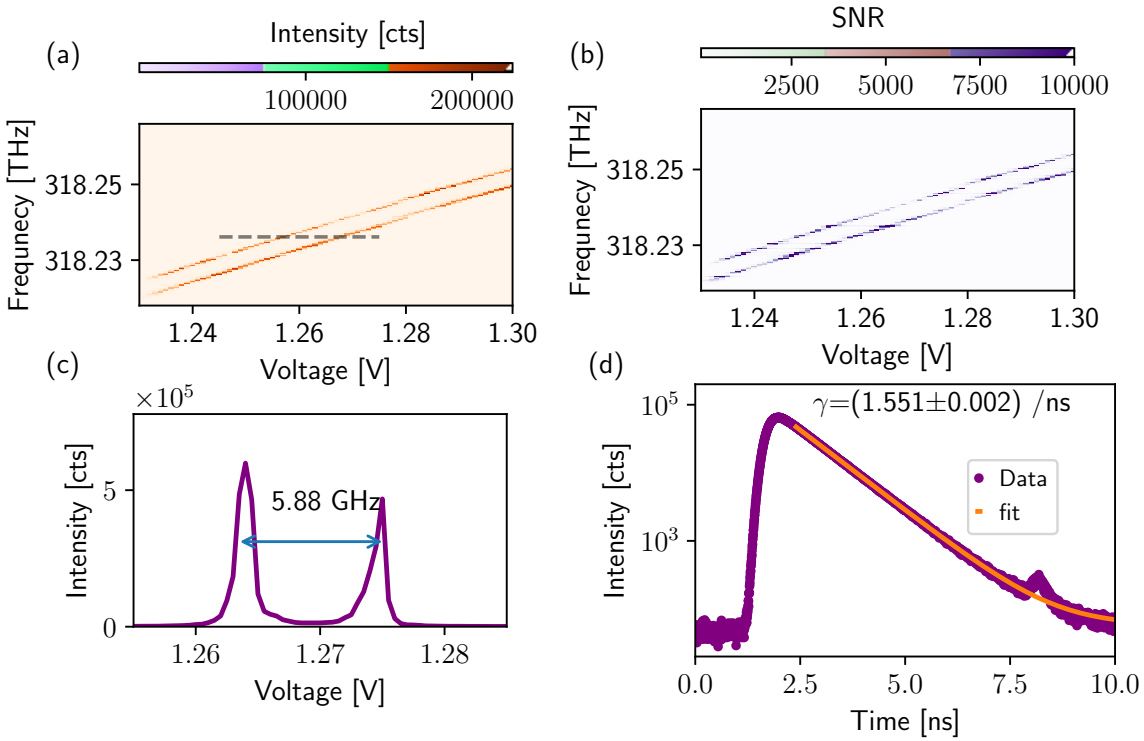

Figure 4.2.4: (a) Resonant pumping of the neutral exciton with a weak continuous-wave tunable diode laser. The two bright lines represent charge plateaus arising from the fine structure splitting of the neutral exciton. (b) The signal-to-noise ratio (SNR) measured in the charge plateaus. (c) The spectrum along the black dash line cut area in (a) is plotted to observe the fine structure splitting, measured to be ≈5.88 GHz. (d) Lifetime measurement performed on the right dipole in plot (c). The background signal is also shown (light green curve). The fitting model is a single exponential function deconvolved with the instrument response function of the setup. Figure reproduced from the supplementary material of [64].

using a time-tagger. A single exponential decay with no beatings in the curve is observed as shown in Figure 4.2.4 . This indicates that the fine structure splitting is large enough to enable us to populate the single dipoles individually. We fit an exponentially decaying function to the obtained curve (orange line in Figure 4.2.4(d)). The decay rate of the neutral exciton was measured to be (1.551 ± 0.002) /ns, which corresponds to a lifetime of 644 ± 1 ns.

Efficiency

For excitation we use a pulsed laser with a repetition rate of 72.6 MHz. To measure the efficiency of the source we compare the count-rate measured on an avalanche photodetector (APD) to the laser repetition rate, where the detection efficiency of the APD has been previously characterized.

We perform a Rabi-oscillation measurement by varying the pump power as shown in Figure 4.2.5(a). The curve saturates at a count rate of 15.6 MHz, resulting in an efficiency of 21.5%. This efficiency is mainly limited by the not fully optimized fiber coupling of the mode generated by the SEG and by the sub-optimal efficiency of the fiber-coupled etalon used for phononic-sideband filtering, both of which can be readily improved further. Nonetheless, the source efficiency we report is so far the highest on planar GaAs nanostructures [16]. This high efficiency makes it possible to integrate the source with the SiN PIC.

Purity

The purity of the SPS is evaluated by a $g^2(0)$ measured in a Hanbury-Brown and Twiss (HBT) setup where a stream of single photons is sent to a 50:50 beam-splitter and registered in single-photon detectors. The SNSPDs produce electrical signals that are processed by a time-tagger, which performs a two-detector correlation measurement. The intensity correlation histogram is seen in Figure 4.2.5 (b), which shows multiple peaks at long time scales. The many peaks are higher in the center and fall down to a constant value outside the central protuberance. This indicates the blinking of the exciton on the decay process, where the quantum dot sometimes decays into a non-radiative state, which takes time to recombine. Integrating the area of the peaks and comparing them as a function of time gives the plot in Figure 4.2.5(c), where it can be seen that after a time of $5.3\mu s$ the effect of blinking is gone. But it was a small effect to begin with, only increasing the area in the center by maximally $\approx 2\%$ compared to the long-time value.

To measure the purity of the source, we analyze the same measurement at short time scales. As shown in Figure 4.2.5 (d), a strong anti-bunched central peak is measured for zero-delay at short time scales. We estimate $g^2(0)$ as the normalization of the central peak integrated counts with respect to the large-time peaks to get a value of

$$g^2(0) = (0.8 \pm 0.1)\% \,. \tag{4.2.1}$$

The low $g^2(0)$ value of our SPS can be attributed to the vanishing laser leakage and weak two-photon emission probability. As described above, the signal-to-noise ratio can reach 1000 at π pulse excitation. This suggests the leaked laser contribution to $g^2(0)$ is less than 0.1%.

Indistinguishability

The indistinguishability is characterized via a free-space Hong-Ou-Mandel setup as shown in Figure 4.2.6(a). A PBS combined with a set of waveplates are used to split the beam into two beams of equal intensity. One of the beams is coupled to a fiber delay that delays the photons by one time bin. The other arm is connected to a polarization controller that is used to correct for any polarization drifts on the two fibers. The polarization is calibrated using a classical light source of the same wavelength and

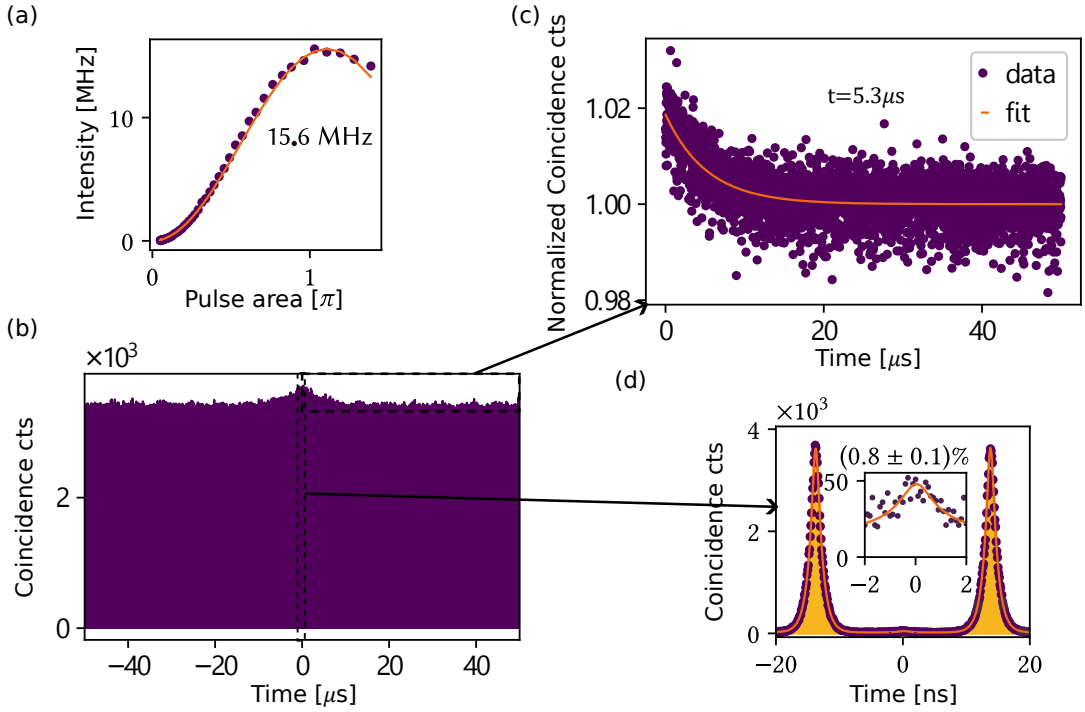

Figure 4.2.5: (a)Plot of Rabi oscillations for a QD excited with increasing pump power, resulting in a broader pulse area. From the peak intensity we extract the maximal count rate of 15.6 MHz. (b) $g^{(2)}$ correlation in long time scale. A peak appears in the center of the correlation histogram arising from the multi-photon emission contribution, this is due to blinking. (c) Integrated coincidence counts under each pulse area. Single exponential fit gives a blinking time of a few μs and a magnitude of 2%. (d) $g^{(2)}$ correlation in short time scale. The $g^{(2)}(0)$ value can be extracted from the area of the central peak as shown on the inset above. Figure adapted from [64].

adjusting the controllers until the interference fringes are minimized. A motorized waveplate is introduced in free space in order to make the photons have the same polarization (co-polarized) or orthogonal polarizations (cross-polarized). At the end a correlation measurement between the two output ports similar to the one done for the purity measurement is performed. The correlation histograms of co-polarization and cross-polarization are recorded separately to test the quantum interference in the indistinguishable and distinguishable cases, respectively. The central peaks in both cases are plotted in Figure 4.2.6(b). The raw indistinguishability is calculated as

$$V_{raw} = (A_{\text{cross}} - A_{\text{co}})/A_{\text{cross}}\,. \tag{4.2.2}$$

. Here A_{cross} and A_{co} are the ratios of the central peak area (after the fit) to the long-time peak area for the cross and co-polarization histograms, respectively. To get the intrinsic value of the indistinguishability, the raw value is calibrated with the HOM

setup imperfection

$$V_{intrinsic} = \frac{(R^2 + T^2)}{2RT} \frac{1}{(1-\epsilon)^2} V_{raw} \,. \tag{4.2.3}$$

Here, two imperfections of the HOM setup are accounted for. A slightly imbalanced BS goes into the equation by setting the measured values of R and T, and a spatial interference offset can be measured with classical light and expressed through ϵ.

We recorded an intrinsic Hong-Ou-Mandel (HOM) interference of subsequently emitted photons of

$$V_{\mathrm{HOM}} = (94.5 \pm 1.7)\% \,, \tag{4.2.4}$$

as shown in Figure 4.2.6(b). The HOM visibility value reported is corrected only with the factor of the HOM setup imperfection. A common correction to perform is that caused by the multiphoton component. Since the SNR was approximately 1000, we consider the multi-photon component to be negligible and did not correct for it. It is also important to notice that the multi-photon component will affect the interference output in photonic interferometers and should therefore also by principle not be corrected.

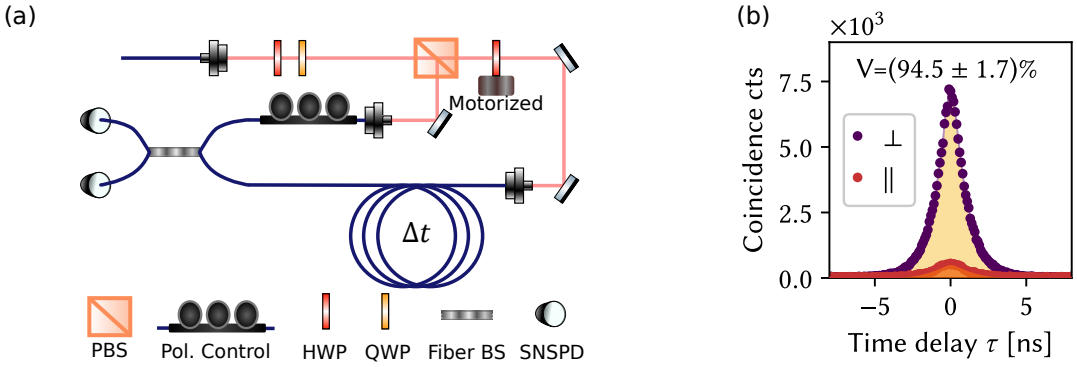

Figure 4.2.6: (a) Free space setup to measure HOM. The motorrized HWP switches between identity and orthogonal polarization of one of the arms in order to compare the photons to the completely distinguishable case. (b) Coincidence measurement result in the distinguishable and indistinguishable cases. The HOM visibility V is extracted from the ratio between the two cases. Figure adapted from [64].

Next generation of sources

Even though our source achieved extremely high values for purity and indistinguishability, there is a lot of improvement left to do on the efficiency of the source. As discussed previously, the efficiency can be readily improved by using a different etalon and its coupling to the fiber.

The current etalon is placed on a separate table and accessed through a fiber coupling. Its resonance frequency is tuned thermally. We have since learned that a

better alternative to thermal tuning is angle tuning, where the etalon is placed directly on the beam path of the collection and its angle with respect to the beam determines its resonance frequency. This way the tuning happens faster and we can avoid an extra fiber coupling. We have measured transmissions of up to 92 % using this method.

The current overlap between the mode comming out of the SEG and the mode of the collection fiber has not been optimized, giving a fiber coupling efficiency of only 60%. By adding cylindrical lenses that can make the beam shape circular instead of elongated, we expect the fiber coupling efficiency to increase up to 95%. The suggested new optical setup is shown in Figure 4.2.7(a), where the suggested cylindrical lenses are shown.

Another improvement lies in the transmission of the objective lens used to focus the light into the sample. Currently we use a double-lense objective, which gives a clear picture of the sample making it easier to work with, but at the cost of having a transmission efficiency of 82 %. We have a single mode objective available that has a transmission efficiency of 95 %.

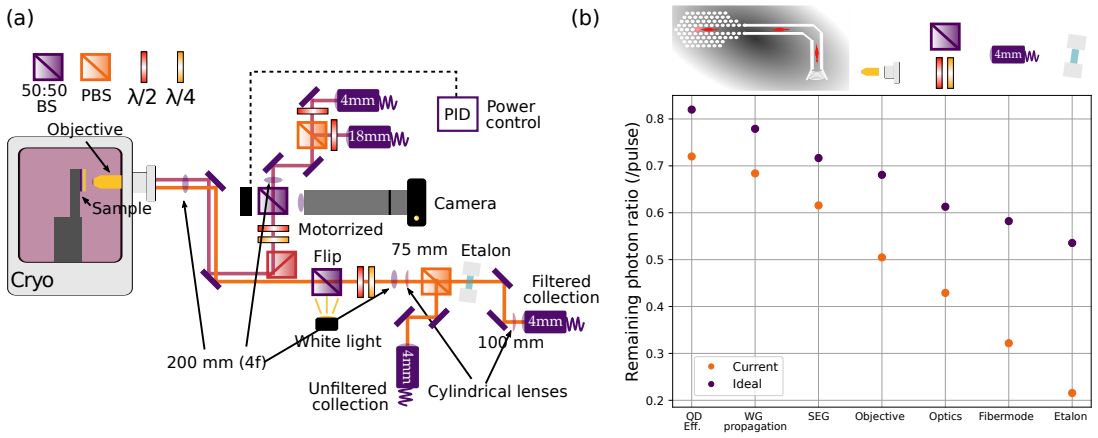

Figure 4.2.7: (a) Optics for excitation and collection of future single photon sources. Some small changes have been made compared to [26], including eliptical lenses, single mode objective and a small cubic mirror (red colored) to differentiate excitation and collection. (b) Probability of a photon surviving after different stages of the collection optics.

Figure 4.2.7(b) shows a plot of the efficiency of the current setup compared to the ideal setup proposed here. The first data-point starts at 82 % for the ideal one since that is the efficiency we estimate after non-radiative decays and decays into the zero-phonon line [26]. The current configuration has an end efficiency of 21.5%, while we expect the ideal configuration to have 54%.

4.2.2 Silicon Nitride Chip

The text in this subsection is adapted from [64].

The photon-emitter platform is optically interfaced to the PIC through optical fibers, as shown in Figure 4.2.1.

Low-loss interferometers are implemented on the SiN platform, with Si_3N_4 waveguides with a rectangular cross-section measuring 100 nm in thickness and 1000 nm in width, enclosed by a SiO_2 cladding. The light from optical fibers is coupled to the chip using a fiber array, through a technique known as butt coupling, where the fiber array is horizontally interfaced with the chip (angle of zero) as shown in Figure 4.2.8. A high coupling efficiency is achieved through the use of waveguide tapers, which are triangular formations with a broad-side width of 50 μm that narrows down to the width of the waveguides of 1 μm. To develop photonic circuitry compatible with the QD

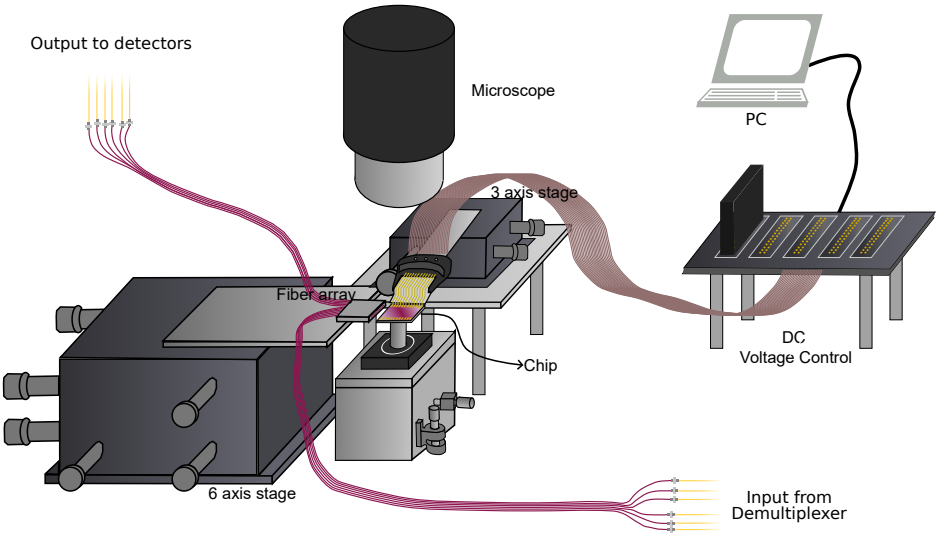

Figure 4.2.8: Illustration of the PICs coupling station configuration

source, we designed and optimized components required for programmable photonic quantum circuits tailored to the QD emission wavelength of 940 nm, and in particular directional couplers for low-loss 50:50 beamsplitters. To create photonic circuits compatible with the QD source, we designed and optimized PIC components specifically tailored to the QD emission wavelength, with a focus on directional couplers for low-loss 50:50 beam splitters. Our chip contained structures for preliminary characterization like waveguides of multiple lengths and directional couplers with distinct coupling lengths. The main structures on our chip where those implementing the four-mode circuit shown in Figure 4.2.1 and the 8 and 12 mode circuits shown in Figure 4.1.4 and in the appendix for this chapter. Using the cut-back method [97], the propagation loss in the single-mode SiN waveguides at the QD emission wavelength was estimated to be approximately 0.3 dB/cm. The total coupling losses to the photonic integrated circuit (PIC) were measured to range from 4.25 to 7 dB at this wavelength. These sub-optimal values are partially attributed to the fabricated devices being optimized for a wavelength other than the target, where losses were significantly reduced

to about 2 dB. This issue can be mitigated by fine-tuning the taper width at the facet.

The phaseshifters in the chip are controlled electrically through a DC current which is generated through contact with a multi-port probe as illustrated in Figure 4.2.8. There is one channel for every phase shifter and additional channels for shared ground connections. The layer with the metal contacts is above the layer with the waveguides such that no consideration needs to be paid to them overlapping or to scratching the waveguides.

We characterized the reflectivity of the directional couplers in the PIC. The most reliable method to do such characterization is to send classical light into one of the MZIs. By scanning the internal phase the output signal will oscillate. The reflectivity of the beam-splitters is in this case proportional to the visibility of the oscillations measured on a powermeter. The extrapolated reflectivities for structures with different parameters are shown in Figure 4.2.9 as a function of the input wavelength. It can be observed that none of the parameter combinations resulted in reflectivities close to the ideal of 50 %, meaning that in a best case scenario we were dealing with 62:38 BSs on the chip.

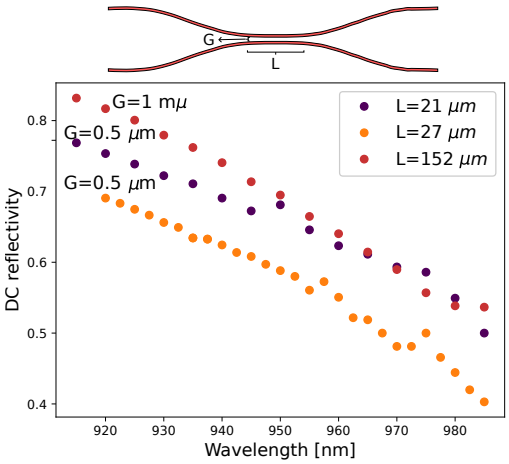

Figure 4.2.9: Reflectivity of the directional couplers as a function of the wavelength for different parameters.

4.2.3 Other components

Demultiplexer

To perform multi-photon on-chip experiments, we add a free-space demultiplexer setup, as shown in Figure 4.2.10(a). The setup uses an electro-optic modulator (EOM) as the active component. An EOM changes the polarization of the photons through the pockels effect, which induces birefringence on a material by applying a strong electric field to it. The EOM changes the polarization of every second photon. After a

PBS this results in every second photon going into a free space delay line, such that it then arrives again at the PBS simultaneously with the next photon in the stream, which is directly transmitted. The two photons are the separated by a second PBS and coupled into different fibers. This effectively results into separating two temporal modes into two spatial ones, yielding simultaneous photons pairs at two different input modes of the PIC. For demultiplexing higher numbers of photons we use a separate

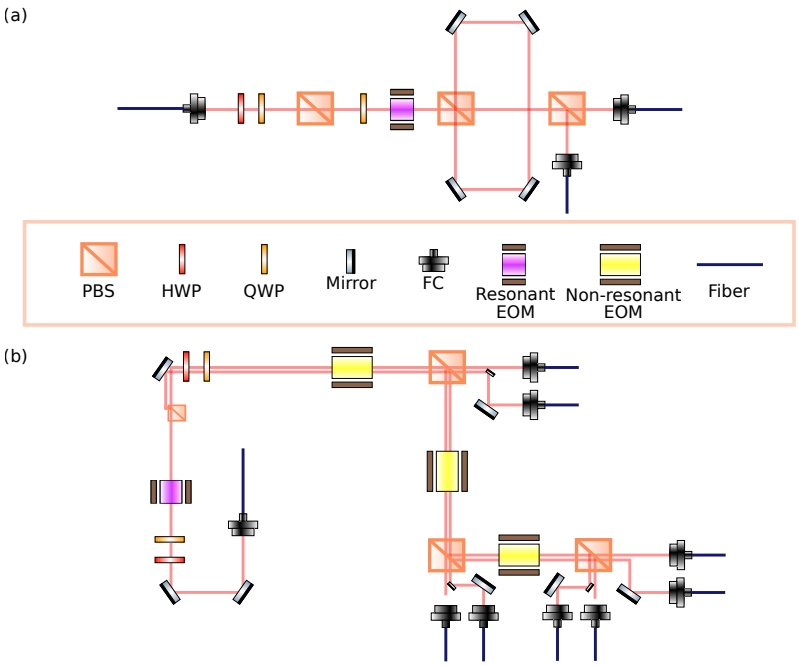

Figure 4.2.10: (a) Two mode demultiplexer. The resonant electro-optic modulator (EOM) sends every second photon into a delay line (b) 8 mode demultiplexer which also serves as a 4 mode demultiplexer if the first resonant EOM is removed.

setup which uses non-resonant EOMs. The advantages of using non-resonant EOMs lies in their freedom of programability, but at the cost of a lower repetition rate. In the case of our EOMs their maximal repetition rate was of 1 MHz. Comparing this laser repetition rates close to 80 MHz means that photons have to be collected into trains of about 20 photons per duty cycle (depending on the specific repetition rate of the laser), which would then have to be delayed on fiber delays 20 times longer than for the case where every photon is modulated individually. A setup with 3 non-resonant EOMs as shown in Figure 4.2.10(b) can serve as a 4 mode demultiplexer. The EOMs are synchronized using a fast-programmable-gate array (FPGA), which is connected to a trigger signal comming directly from the laser. The setup can be readily upgraded to be an 8 mode demultiplexer by adding a resonant EOM that shifts every second photon into a different path, also shown in Figure 4.2.10(b).

4.2.4 Setup losses

Here we report the estimated losses in our experimental setup. The experiment operates at a 72.6 MHz rate, dictated by the pulse repetition rate of the excitation laser. The photon count rate detected on the SNSPDs after propagation through all components of the setup ranged between 40 kHz and 10 kHz, depending on the output mode of the chip. Based on these measurements, we estimate total system losses to be between 32 and 36 dB, with contributions from various components detailed below.

The transmission efficiency through the two-mode demultiplexer was measured at 25% after manual optimization of the polarization. However, due to polarization drifts of the single photons during data collection, the average transmission over an hour-long experiment dropped to approximately 20%, corresponding to 7 dB of losses. Additionally, a lossy connection following the etalon, which could not be replaced during the experiment, introduced an extra 5.9 dB of losses before transmitting photons from the SPS to the demultiplexer.

We can estimate the insertion losses on the chip by measuring the throughput on simple and short test-structures. We measured the transmission to be of about 15%, since this include both the in- and out-coupling losses we estimate the insertion loss to be 4.25 dB per facet. However, these are ideal cases were we only had to couple one input and output of the fiber array. We expect the losses to be slightly higher when coupling multiple modes simultaneously. We can establish an upper bound for the coupling losses by consider the channel with the worst transmission in our interferometer after phase optimization. We estimate this upper bound to be 7 dB. Coupling of light to the chip can therefore account for 8.5 to 14 dB of the total losses.

We characterized the efficiency of our SNSPDs at at previous point and found that most detectors had efficiencies of around 80%. Since the different modules of our experiment are located at different laboratories we also experience losses due to the fibers connecting in between them, and we estimate these losses to be 1-2 dB per photon in total. Adding our losses together we obtain a lower bound of 30 dB and an upper bound of 37 dB, which are in agreement with the loss expected from direct measurement of the count rate. We summarize our losses in Table 4.1.

Table 4.1: Estimated optical losses for the different elements in the experimental setup

Component	Expected loss
Source setup	6.7 dB
Off-chip interfaces	5.9 dB
Two-mode demultiplexer	7 dB
SiN chip	8.5 to 14 dB
Fibers	1 to 2 dB
SNSPDs	1 dB
Total expected losses	30 to 36 dB
Total measured losses	32 to 36 dB

4.3 Multi-photon experiments

In this section we present experimental results obtained with the single photon source combined with the SiN chip, which is the experimental setup shown in Figure 4.2.1.

4.3.1 On-chip purity and indistinguishability

To characterize the quality of the PIC, we perform measurements that directly depend on the purity and indistinguishability of the emitted single photons.

In order to characterize the purity we simulate an HBT experiment on our PIC by choosing an isolated MZI and setting its phase to $\pi/2$ so that it will act like a 50:50 BS. The $g^{(2)}(0)$ is measured by recording coincidences between the two outputs normalized by coincidences between different pulses, as shown in Figure 4.3.1(a), obtaining a purity of 99.6%, which is comparable with the free-space value. The $g^2(0)$ on-chip calculation model is slightly different from the corresponding one in free space. We normalized the central peak area counts to the average of all of the side peak areas instead of only considering large-time peaks. This is because the on-chip intensity correlation measurement operated in a shorter time bin. Furthermore, the on-chip correlation histogram has a low count rate which also fluctuates due to the polarization instability of the setup and has a high uncertainty under integration times of 30 minutes. The $g^2(0)$ measured from free-space HBT setup is (0.8 ± 0.1) % at π pulse excitation, while $g^2(0) = (0.4 \pm 0.2)\%$ is obtained from the on-chip measurement. We include the

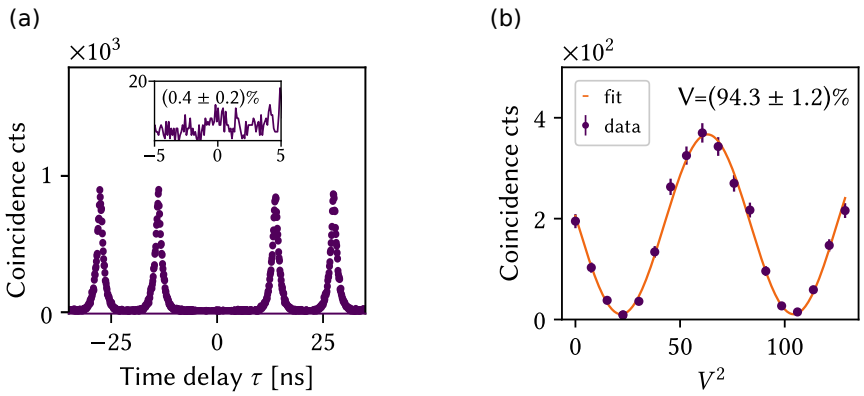

Figure 4.3.1: (a)On-chip $g^{(2)}$ correlation measurement. Performed by setting one of the on-chip MZIs to act as a 50:50 BS. (b) On-chip HOM. Scanning the phase gives oscillations in the coincidence counts, where the visibility provides the single photon indistinguishability..

demultiplexer in order to perform a HOM interference experiment. The experiment consists of scanning the phase of an MZI interferometer in order to obtain interference oscillations similar to those presented in Figure 4.1.2. In practice we record a two-detector correlation measurement for different applied voltages. As the phaseshift is proportional to the square of the voltage applied, we obtain the plot shown in Figure

4.3.1(b). We extract the HOM visibility from the fitted visibility of the sinusoidal curve [85]. We find $V_{\mathrm{HOM}} = (94.3 \pm 1.1)\%$ which is very similar to the value we obtained for the free space HOM interference experiment. We observe that the degree of quantum interference is not degradated by our PIC platform.

4.3.2 Fusion gate

We now proceed to evaluate the quality of a fusion gate performed on our chip. This evaluation takes place by making use of the fact that a fusion gate is analogous to the probabilistic photon–photon entanglement gate introduced in the previous section. This is made clear on Figure 4.3.2. Thus evaluating the quality of the entangled state produced with the circuit included in our chip will give us a measure of the fidelity of a fusion operation performed on the SiN platform.

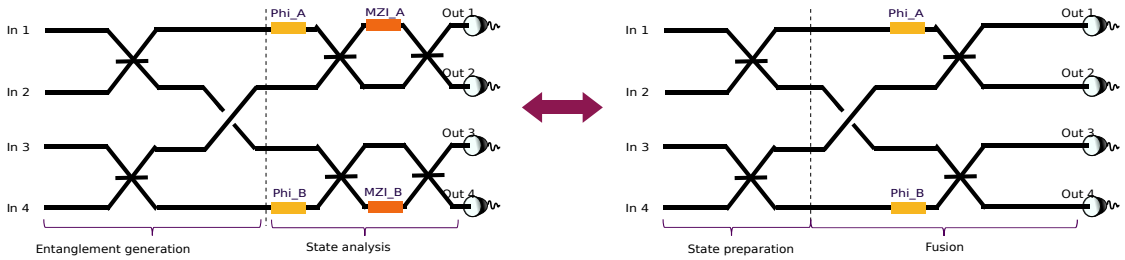

Figure 4.3.2: Equivalence between a fusion and a probabilistic photon-photon entanglement gate. The phases of the MZIs on the state analysis of the probabilistic photon-photon entanglement gate are set to $\pi/2$ to make them act like BSs.

We encode a pair of photons on path encoded qubits according to the mode numbers as $1 \mapsto |0\rangle_1$, $2 \mapsto |1\rangle_1$, $3 \mapsto |0\rangle_2$, and $4 \mapsto |1\rangle_2$. Sending photons into inputs 1 and 3 of the interferometer results in an even superposition of the two qubits, which after the swap gate results in the entangled Bell state $|\psi^+\rangle = (|0\rangle_1 |1\rangle_2 + |1\rangle_1 |0\rangle_2)/\sqrt{2}$. It is important to mention that this only applies when detector combinations that are valid in the qubit picture are observed, i.e. when there is one photon on each mode-pair [98, 99, 100]. This scheme has a success probability of 50%.

The second half of the circuit constitutes a two-qubit state analysis circuit, where the phases Phi_A and Phi_B indicate the angle in the XY plane of the bloch sphere, while the MZI phase indicates the angle in the XZ plane. We can thus measure the two qubits in any arbitrary basis combination, a freedom which we employ to reconstruct and analyse the generated entangled state.

Some example results of the raw data we get from the two-detector correlation measurements are shown in Figure 4.3.3(a), where the top figure shows the coincidences between detectors 1 and 3 when no phase is applied and the final MZI is set to be a 50:50 BS. This corresponds to a measurement of the state $|00\rangle$ in the X basis. The bottom picture shows the same but for an applied phase of $\pi/2$ on both phaseshifters,

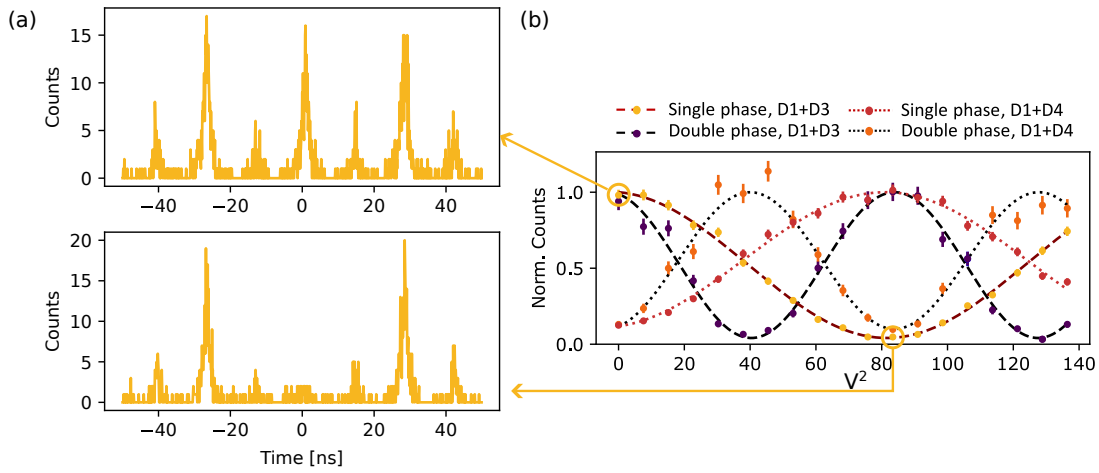

Figure 4.3.3: (a) Correlation measurements between detectors 1 and 3 for no applied phases (top) and for $\text{Phi}_A = \text{Phi}_B = \pi/2$ (bottom) (b) Plot of the correlation features for varying the phases Phi_A and Phi_B (or only Phi_A) which are directly proportional to the square of the voltage applied. Each value is obtained by calculating the ratio between the central and the side peak on the corresponding correlation measurement. Figure

which corrresponds to a measurement on the Y basis. Scanning the voltage and recording the coincidences for different detector combinations gives the data shown in Figure 4.3.3(b), where the Single phase label corresponds to only scanning the upper phase Phi_A, while double phase corresponds to scanning both Phi_A and Phi_B simultaneously. From the visibility of these curves we can extract the correlation data of the output states in different bases. For example, a double phase scan oscillates between measuring in X_1X_2 and Y_1Y_2 in a sinusoidal curve. The amplitude of the state $|00\rangle_{XX}$ equals the visibility of the curve for its corresponding detector configuration (D1+D3), while the amplitude of the state $|00\rangle_{YY}$ equals one minus this visibility.

We show the correlation data results for the Pauli matrices in bases X_1X_2, Y_1Y_2, and Z_1Z_2 in Figure 4.3.4(a), showing high probabilities for $|00\rangle$ and $|11\rangle$ states when measuring X_1X_2 and high values for $|01\rangle$ and $|10\rangle$ when measuring Y_1Y_2, and Z_1Z_2. These results are as expected for the entangled Bell state $|\psi^+\rangle$. We measure the qubits in two additional Pauli bases: X_1Y_2 and Y_1X_2, by extracting them from the single-scan visibilities from Figure 4.3.3. We obtain a total of 16 2-qubit measurements, allowing us to reconstruct the density matrix of the output state via quantum state tomography as specified by James et al. [101]. The density matrix we reconstruct is illustrated in Figure 4.3.4(b). Its overlap with the ideal density matrix of a $|\psi^+\rangle$ entangled state is of 92%, providing an important measure for the fidelity of the entangled state generated by the PIC.

It is important to analyze the reasons why the fidelity of the state is different from unity, in order to asses how to improve further experiments and wether or not

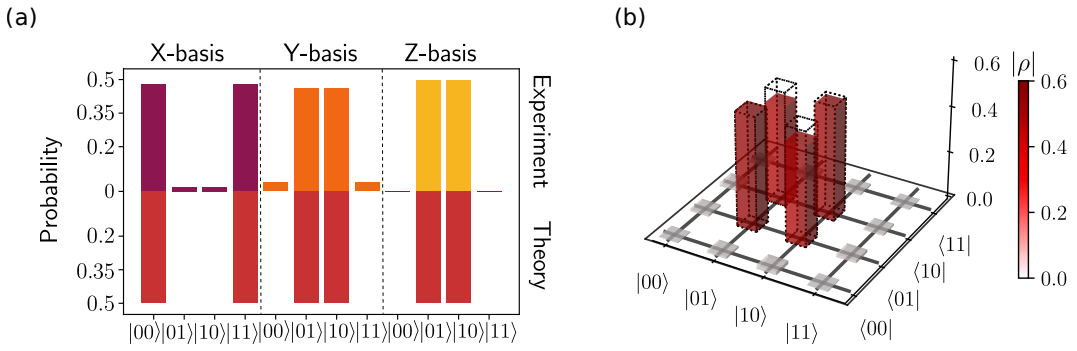

Figure 4.3.4: (a) Correlation data for Pauli X_1X_2, Y_1Y_2, and Z_1Z_2 qubit measurements on the generated Bell state $|\psi^+\rangle$. Top histograms are measured expectation values, while bottom values are theoretical expectations. (b) Density matrix reconstruction of the post-selected Bell state via state tomography. The red pillars represent the absolute values of the reconstructed density matrix, with transparent dashed pillars representing theoretical expectations. The corresponding measured state fidelity for $|\psi^+\rangle$ is 92%. Figure and caption adapted from [64].

the material platform is introducing extra errors. The first error source we want to investigate is imperfect beamsplitters. We estimate the imperfect splitting ratio of the on-chip directional couplers to be approximately 62/38 for the structures we were working on, as can be seen in Figure 4.2.9. Taking this mismatch into account (and assuming perfect indistinguishability), we calculate that the fidelity becomes 96.7%, meaning that imperfect on-chip components reduce the fidelity by approximately 3%. The second error source we investigate is photon distinguishability, which we quantified through a free space HOM interference experiment to be $(94.53 \pm 1.70)\%$ (see Figure 4.2.6 (b)). We numerically simulate how this noise affects the output statistics by using the multipermanent of the transfer matrix as explained in Chapter 2. Implementing both noises simultaneously in the simulation, we can calculate the output probability of the photons ending in any of the four possible output states. If we measure for example in the Pauli X_1X_2, Y_1Y_2, and Z_1Z_2 bases, we obtain 12 simulated values which yield an average fidelity of 99.4% when compared to the measured distribution. We observe that this error model accurately captures to two main error sources in this experiment. The remaining error margin is likely due to the small presence of a multi-photon component in the light, which could be added in the model to further refine it.

Since the photon-photon entanglement circuit is equivalent to a fusion circuit, we can infer that a fusion performed on this platform would have a fidelity of 92%, and that the main error source lies in photonic distinguishability. A later experiment, similar to the one described here, was performed in [102], where the equivalence between entanglement and fusion circuits is also employed. It can be seen that using highly

indistinguishable single photons from heralded sources and advanced fabrication techniques to obtain ideal 50:50 splitting ratios, fusion fidelities above 99% can be achieved on this platform.

4.3.3 Bosonic suppresion laws

Another experiment we can do with our platform is a test of the generalized HOM quantum interference in the form of bosonic suppression laws in a discrete Fourier transform (DFT) interferometer.

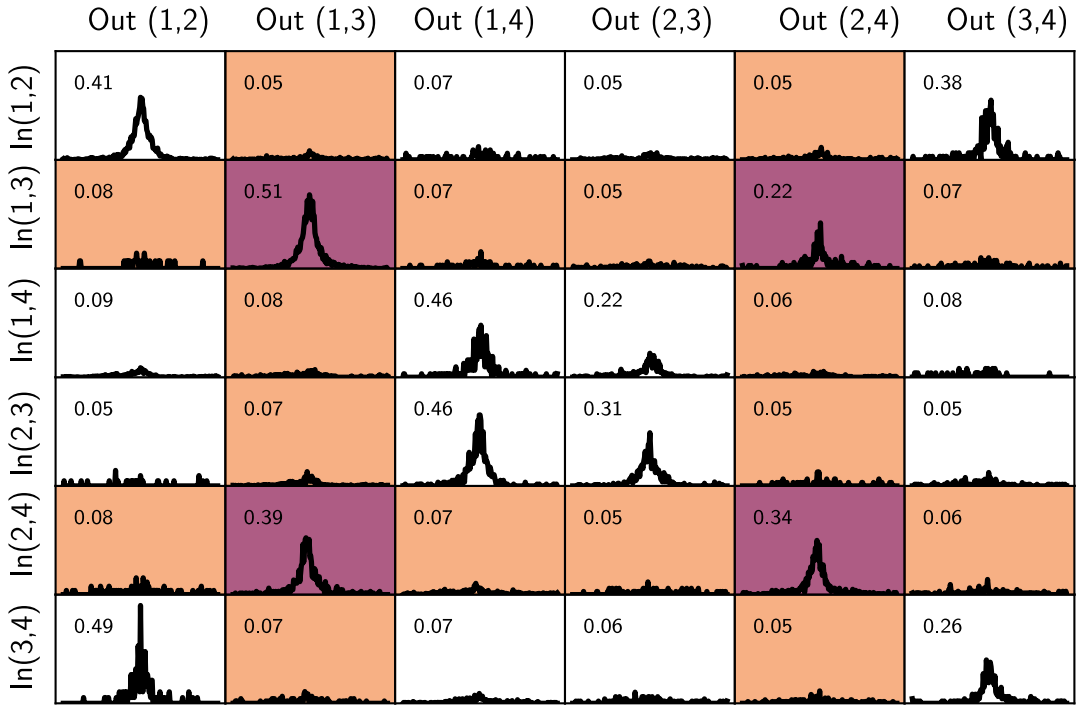

Figure 4.3.5: Experiment result of Bosonic suppression laws. Raw detection histograms are reported for all anti-bunched input-output configurations, together with the associated measurement probabilities obtained. The combinations that are expected to be suppressed and enhanced by the suppression law are highlighted in orange and purple, respectively. Figure and caption adapted from [64]

We program the MZI phaseshifters for them to behave as 50:50 BSs, in which case we get a four mode DFT interferometer described by the unitary matrix

$$U_{l,q} = \exp[(l-1)(q-1)2\pi \mathrm{i}/4]/2\,, \tag{4.3.1}$$

where $l, q \in \{1, 2, 3, 4\}$ correspond to the spatial mode number of the interferometer. This is the interferometer shown at the bottom of Figure 4.1.5(a).

We consider the case of sending $n = 2$ photons into de described fout-mode DFT interferometer. Cyclic input configuration for this case consists of sending photons into modes $(1, 3)$ and $(2, 4)$. According to eq. 4.1.3 we expect enhancement in output configurations $(1, 3)$ and $(2, 4)$ and suppression in all other configurations.

We perform an experiment to test the bosonic suppression laws with our chip. Using the two-mode demultiplexer we send photons into all 6 possible input-mode configurations and record the coincidences in all the 6 possible output-mode configurations. The results are shown in Figure 4.3.5, where the expected suppressed and enhanced configurations are highlighted in orange and purple, respectively. The white regions are those configurations that are not relevant to the bosonic suppression laws. We see suppression and enhancement exactly where it is expected according to theory, showing multimode photonic interference in our PIC. We examine the effect of experi-

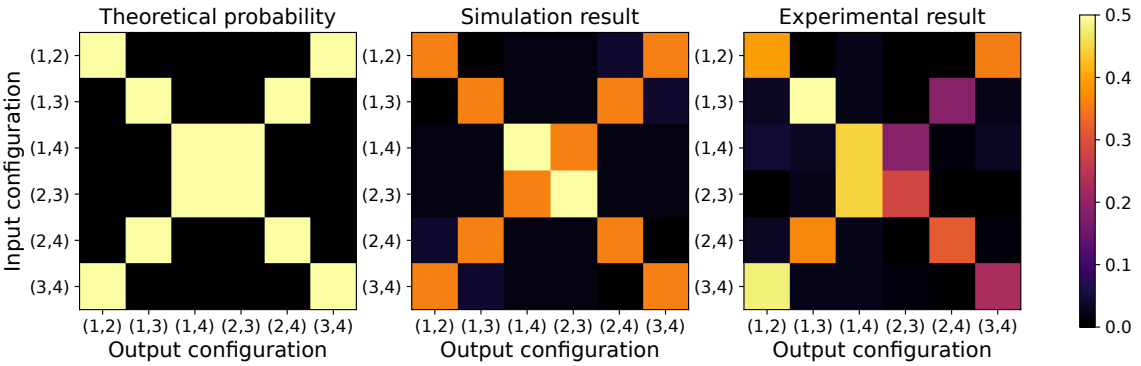

Figure 4.3.6: Bosonic suppression laws input-output distributions for the perfect theoretical case, simulation with imperfections taken into account, and experimental results. Figure reproduced from [64]. Figure reproduced from the supplementary material of [64].

mental imperfections on this experiment in a similar manner than for the probabilistic Bell state experiment. The left plot in Figure 4.3.6 shows the theoretic distribution if no imperfections were present. The center plot shows our simulation where we include errors like photonic distinguishability and imperfect ratio of the BSs are taken into account. The plot on the right shows the distribution obtained by the experimental data. We can see that errors like partial distinguishability and imperfect BSs create a distribution that resembles the experimental one, but the resemblance is not as clear as in the probabilistic Bell experiment. The fidelities of the HOM and Bell-state experiments are both above 90% while the fidelity of the suppression laws experiment calculated to be 73%. This discrepancy is attributed to coupling efficiency variation across modes. This is harmful to the fidelity of the suppression laws measurement, however, it does not have a big impact on the other experiments, where the input-output modes were fixed.

4.3.4 Heralded entanglement generation

Our PIC platform contained structures capable of performing heralded Bell and GHZ entangled-state generation. However, due to a malfunction in the 4 mode demultiplexer at the time this experiment was performed, we did not do experiments with more than 2 photons. At the time we had fixed the demultiplexer this feat was already performed by other groups [19, 103, 104], so we decided not to perform the experiment. The photonic circuits we had designed to perform these experiments are showcased in the appendix for this chapter.

4.4 Concluding remarks and outlook

In this chapter we introduce the concept of PICs and how they can be employed to implement compact photonic interferometers capable of single-photon processing.

Simple experiments requiring a low number of photons are introduced, particularly schemes for post-selected and heralded entanglement generation, as well as multi-photon interference schemes. These experiments can be implemented on PICs in order to test their functionality when integrating them with single-photon emitters.

We describe a chip fabricated on SiN which contains photonic interferometers capable of conducting the introduced experiments. Our approach to interface this PIC with our source is a modular one, as shown in the sketch of our experimental showcased in Figure 4.2.1.

Single and multi-photon experiments were performed using our experimental setup. We perform a fusion between two superposition states with a fidelity of 92%. The Bosonic suppression laws were demonstrated, which at the time of our experiment constituted the first time realization for a solid-state photon source. Conducting an error analysis we find that the main obstacle in the way of higher fidelities is imperfect BS ratios and photonic indistinguishability. Imperfect BSs can be readily corretcted with improved design of the directional couplers to be fabricated, but even if they happen they can be accounted for in the data analysis, making them a treatable problem. Photonic distinguishability on the other side is much harder to deal with, and it will be the focus of the next chapter of this thesis.

We have experimentally demonstrated that fusion operations and other quantum information tasks can be efficiently performed in a scalable PIC, opening the path for larger scale fusion-based quantum computation experiments with deterministic single photon sources.

Chapter 5

Indistinguishability Purification

In this chapter we demonstrate that partially distinguishable single photons can be purified to reach near-unity indistinguishability by the process of quantum interference.

Statement of work

This chapter is a combination of different theoretical and experimental projects all centered about indistinguishability purification protocols and under close supervision of Stefano Paesani. The author of this thesis developed the theoretical models and conducted the two experiments described in this chapter. The simulations were performed using software developed by Stefano Paesani. The physically inspired model was developed in collaboration with Andrew B. Villadsen and Eva M. Gonzales Ruiz. The Switch-based experiment was built and performed together with Stefan N. Van den Hoven. The demultiplexer-based experiment was performed at the University of Vienna in close collaboration with Lorenzo Carosini with experimental support from Huan Cao, Lena M. Hansen and Francesco Giorgino.

Our work resulted in a published article specified in [32]. This chapter has segments and figures that are adapted with minor adjustments from the article.

5.1 Introduction

Photon indistinguishability is a key requirement for multi-photon quantum experiments, where successful interference relies on identical spectral, temporal, and polarization properties [105, 106]. Imperfect photon sources, such as quantum emitters or SPDC sources, often produce photons with deviations in these properties, reducing indistinguishability and, consequently, the fidelity of quantum operations. To date, no approaches have been experimentally shown to address this problem efficiently. This chapter investigates one such approach, detailing its theoretical foundation, experimental implementation, and implications for scalable quantum photonic platforms.

Epitaxial quantum dots (QD) can generate highly indistinguishable photons due to the ability to precisely engineer their semiconductor environment [107, 16, 15], and

they have been employed to perform quantum interference experiments with multiple photons [18, 103, 108, 104, 109]. Nonetheless, distinguishability between photons remains a limiting factor for achieving perfect quantum interference between the generated photons, an poses a challenge for the realization of large scale operations with photons. [110].

In solid-state quantum emitters, photon distinguishability mostly arises from processes that are either fast or slow compared to the photon lifetime. Among fast processes, the only relevant one is pure dephasing, an error arising due to interactions of the emitter with phonons in the environment (see Figure 5.1.1 (a)). Slow processes include such as spectral diffusion, due to interactions with charges, and polarization drifts, due to transport of photons through fibers [111, 107].

Monitoring the environment of the QDs can help improve the indistinguishaibility of the emitted photons. Pure dephasing can be reduced by decreasing the temperature, which simply reduces the ammount of phonons in the environment. It can also be reduced by decreasing the QD lifetime via the Purcell effect, which reduces the amount of time that the QD interacts with phonons [111]. Techniques have also been developed to efficiently reduce the electrical noise present in GaAs photonic microchips, reducing the effect of spectral diffusion [67]. These techniques, even though efficient, are expensive to implement and have so far not been proven to be very efficient for reducing pure dephasing.

Recently there have been theoretical protocols that show a method to mitigate partial distinguishability that does not require monitoring of the QD environment. These protocols act on already-emitted photons which are processed in linear optical circuits and rely on the detection of ancillary photons [112, 113]. These we call indistinguishability purification protocols.

Purification of quantum states is a well established concept within quantum information. If one possesses multiple copies of a noisy entangled state, an entangled state with high fidelity can be obtained by applying Bell measurements between the noisy states [114]. This technique has promising applications as it can be used even for large states, known as "magic states", and has appplications in fault-tolerant quantum computation [115]. This concept has been adapted to single-photon indistinguishability by Sparrow and Marshall. In their protocols, low quality entanglement corresponds to single photons produced in a noisy environment, and the Bell measurements correspond to quantum interference in linear-optical circuits.

Indistinguishability purification protocols are heralded, meaning that while they operate probabilistically, successful events are explicitly identifiable when they occur. Introducing multiple parallel instances of the setup and selecting those where successful events are recorded—a process known as multiplexing—mitigates the limitations associated with the probabilistic nature of the protocol [116]. Apart from the efficiency, the output indistinguishability can also be arbitrarily close to unity by applying the protocol repeatedly.

In Section 5.2 we describe the protocol and introduce models for interference of partially indistinguishable photons; these models are then used to make predictions about

the indistinguishability purification achieved under different conditions. In Sections 5.3 and 5.4 we then describe two separate experimental efforts to test the protocol. The first experiment consists of a time-bin encoded approach, where the indistinguishability purification happens over repeated instances in time. The second experiment consists of a demultiplexed experiment, where the purification happens simultaneously at different points in space. Finally, in Section 5.5 we present and discuss the results of both experiments.

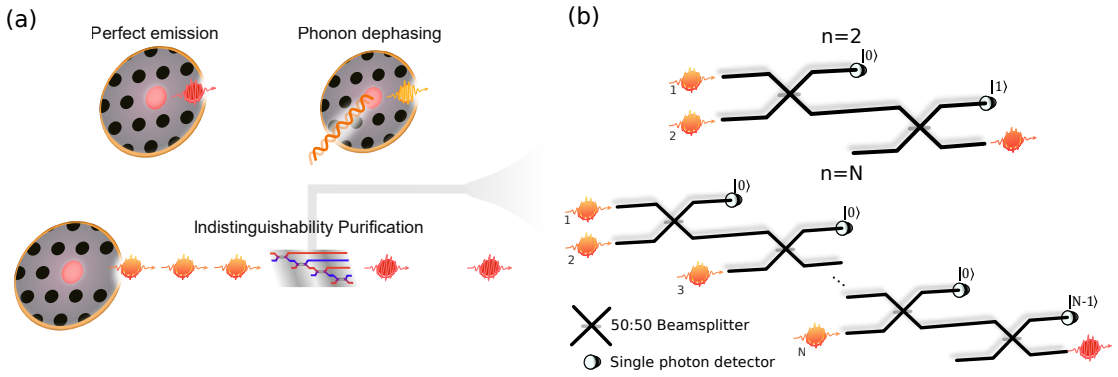

Figure 5.1.1: (a) Dephasing processes in single-photon sources like quantum dots add distinguishability to the emitted photons. (b) Examples of indistinguishablity purification circuits. These are based on cascaded Hong-Ou-Mandel-type quantum interferometers, and, depending on the heralding pattern, output a highly indistinguishable single photon. We use n to denote how many photons are required by the purification process. In the figure we have $n = 2$ photons (top) and an arbitrary photon number $n = N$ (bottom). Figure adapted from [32].

5.2 Protocol

The fundamental principle underpinning our indistinguishability purification protocol is that indistinguishable photons exhibit a higher probability of bunching on a beam splitter (BS) compared to distinguishable photons, as illustrated in Figure 5.2.1(a). If two photons are known to have interfered with each other, they then have a higher chance of being indistinguishable than before going through the beam splitter. An easy way to know if two photons bunched in a beam-splitter is to put a detector on one of the arms and verify that there is vacuum on this arm. Since the bunching occurs randomly in either arm of the beam splitter, the photons will be detected in the chosen arm 50% of the time, resulting in a loss in the protocol. If there is indeed vacuum on the detector, and we assume negligible losses in the BS, we can be certain that there are two photons with a high indistinguishability present on the opposite arm. This constitutes a single instance of indistinguishability purification. In order

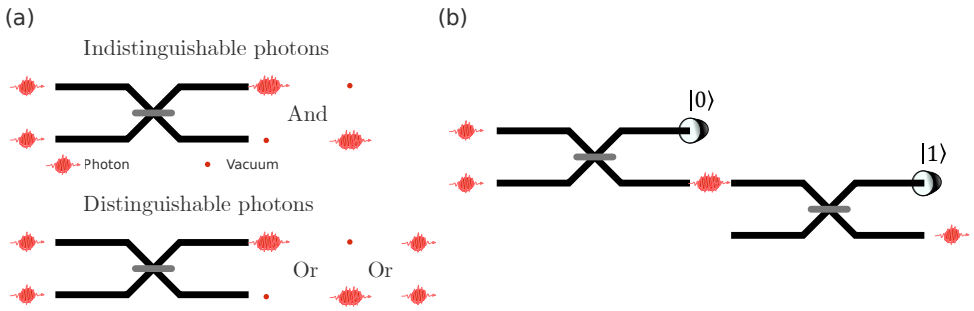

Figure 5.2.1: (a) Distinguishable photons take random paths when going simultaneously into a beam splitter (BS). The outcomes can be to have bunched photons in either output, or one photon in each output. Indistinguishable photons experience quantum interference if they arrive simultaneously at a BS, such that only the bunched outcomes are possible. (b) A zero detection on one arm of a BS heralds the presence of a bunched output on the other arm. In order to separate the two bunched photons an extra BS and a detector are used. A one-photon detection heralds the pressence of a highly indistinguishable photon on the other output.

to separate the two photons into two single photon states again, a second BS and a detector are required. If the detector records a one photon state, then it is known that the photon in the other arm is highly indistinguishable. This whole process is depicted in Figure 5.2.1(b). It is important to note that this procedure is heralded, as the occurrence of a vacuum in the first detector followed by a single-photon state detection in the second detector indicates the presence of a highly indistinguishable photon in the output arm.

The indistinguishability of the output photon can be further improved by introducing additional instances of the purification process as depicted in Figure 5.2.2(a), where a third photon is sent to interfere with the purified two-photon state. It can be shown that in an experiment where there is two photons in one arm of a BS and only one on the other, indistinguishable photons still have a higher chance of bunching than distinguishable ones. Therefore, detecting vacuum on one of the output arms will increase the indistinguishability of the resulting 3-photon state even further. The process can be repeated arbitrarily many times as depicted in Figure 5.2.2, where N partially distinguishable photons are combined to produce a highly indistinguishable single-photon output. We use the notation n=N, where n denotes the number of photons required by the purification process.

Before going into success probabilities and improvement rates, a common question arises at this point. The final photon is highly indistinguishable, but with respect to what? And will it be useful?

The answer to these questions relies on the way photons acquire distinguishability in practice, and it will help us understand the advantages and limitations of this protocol. There are two cases to be explored: Either the protocol is used to purify

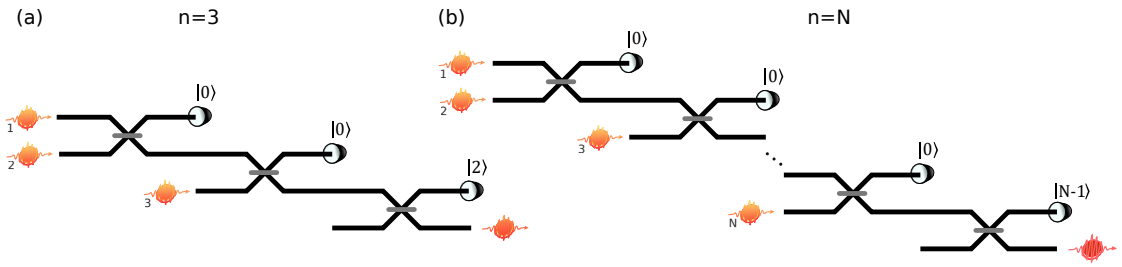

Figure 5.2.2: (a) Indistinguishability purification by interference of 3 photons, which we denominate as n=3. (b) Indistinguishabilty purification combining N photons. The detector at the last output has to be photon-number resolving in order for it to work.

photons coming from a single source, or it is to be used to purify photons coming from different sources.

In the first case, there are two kinds of errors to be explored when taking the photon generation rate into account. There are *fast* errors, meaning that they happen in time-scales shorter or in the range of the photon generation rate, which will affect the generation of specific photons individually and decrease the measured indistinguishability between any two photons emitted by the source. There are then *slow* errors which happen on time scales much larger than the photon generation rate, which will affect multiple photons and will only contribute to experiments where one photon has to interfere with another one generated at a much earlier time, but is not relevant for most single-source experiments as they rely on the interference of successive photons. Our protocol is effective for mitigating the effect of fast errors, as two photons that interfere on a BS will have a lower chance of having experienced a fast error, but our protocol will not mitigate slow errors in photons from a single source.

Finally, there is the case of two different sources interfering with each other. In this case, both slow and fast errors will influence any HOM interference experiment. In this case, indistinguishability purification will only work if the photons from the two sources are purified together, instead of being purified individually. An explanation can be found in Figure 5.2.3.

5.2.1 Expected improvement

It is important to quantify the cost and benefits of doing indistinguishability purification. The cost is linked to the success probability, and the benefit to the improvement in indistinguishability.

The success probability depends on the indistinguishability of the input photons. Here we will compute the success probability for the two extreme cases where the photons are either completely distinguishable or completely indistinguishable. The distinguishable case can be treated purely with combinatorics, as there will be no interference between the photons. We define P_n as the success probability of the final purification instance in a protocol combining n photons, and P_s as the probability to

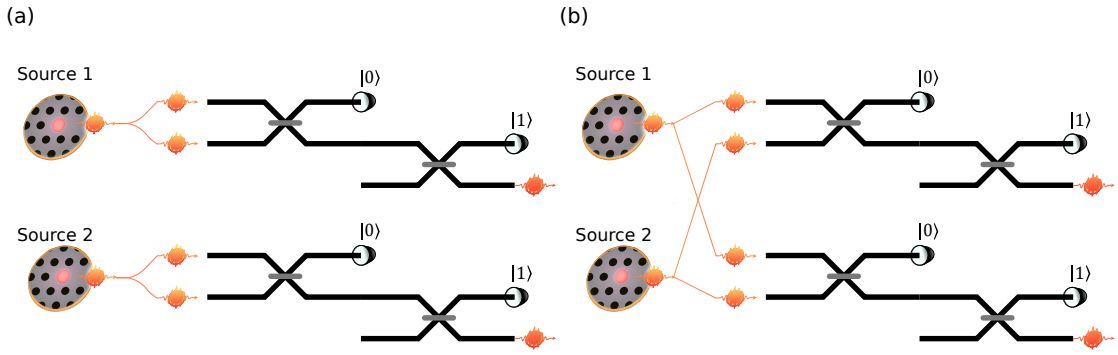

Figure 5.2.3: (a) Indistinguishability purification for single sources. The output photons will be less distinguishable compared to other photons from the same source, but still distinguishable compared to the ones from the other source. (b) Indistinguishability purification for multiple sources. The output photons will have increased indistinguishability even though they come from different sources.

separate the state into a one photon and an $n-1$ photon state. These are defined in Figure 5.2.4(a). The first one is

$$P_n = \left(\frac{1}{2}\right)^n , \tag{5.2.1}$$

as each photon has the same probability of making it into the lower arm of the beam splitter. The second can be calculated from the binomial coefficient

$$P_{\mathrm{s}} = n\left(\frac{1}{2}\right)^n . \tag{5.2.2}$$

These two can be combined to calculate the success probability of the protocol for completely distinguishable photons

$$P_{\mathrm{dist}} = \left(\prod_{k=2}^{n} P_k\right) P_{\mathrm{s}} = n\left(\frac{1}{2}\right)^{\left(\sum_{k=2}^{n} k\right)+n} . \tag{5.2.3}$$

In the indistinguishable case, we calculate P_n from the probability amplitude A of getting an n photon state on one arm of the BS

$$A = \langle 0_c n_d | (n-1)_a 1_b \rangle = \langle 0_c n_d | \frac{1}{\sqrt{(n-1)!}} (a_a^\dagger)^{n-1} a_b^\dagger \, | \, \rangle , \tag{5.2.4}$$

where a, b and c, d refer to the input and output arms of the BS. After the beam

splitter transformation this expression becomes

$$\begin{aligned} A &= \frac{1}{\sqrt{(n-1)!}} \frac{1}{(\sqrt{2})^n} \langle 0_c n_d | \left(a_c^\dagger + i a_d^\dagger\right)^{n-1} \left(i a_c^\dagger + a_d^\dagger\right) |0\rangle \\ &= \frac{1}{\sqrt{(n-1)!}} \frac{1}{(\sqrt{2})^n} \langle 0_c n_d | \left(\sum_{k=0}^{n-1} \binom{n-1}{k} (a_c^\dagger)^k i^{n-1-k} (a_d^\dagger)^{n-1-k}\right) \left(i a_c^\dagger + a_d^\dagger\right) |0\rangle \ . \end{aligned} \tag{5.2.5}$$

The inner product ensures that only the term with the highest exponent in a_d survives. The probability P_n can then be calculated as

$$P_n = |A|^2 = \left| \frac{1}{\sqrt{2}^n} \frac{\sqrt{n!}}{\sqrt{(n-1)!}} \right|^2 = \frac{n}{2^n} \, . \tag{5.2.6}$$

For calculating P_s one has to realize that there is no interference involved since only one input arm of the BS is populated. Therefore the probability P_s for the indistinguishable case will be the same as that for the distinguishable case. The final success probability is then given by

$$P_{\text{indist}} = \left(\prod_{k=2}^{n} P_k\right) P_{\text{s}} = \frac{(n-1)!}{2^{\sum_{k=2}^{n} k}} \cdot \frac{n^2}{2^n} \, , \tag{5.2.7}$$

which decreases exponentially which the number of purification instances. This is the success probability for completely indistinguishable photons. The sucess probability for completely distinguishable photons is lower, as plotted in Figure 5.2.4 and the actual success probability of an experiment with partially distinguishable photons can be expected to be somewhere in between.

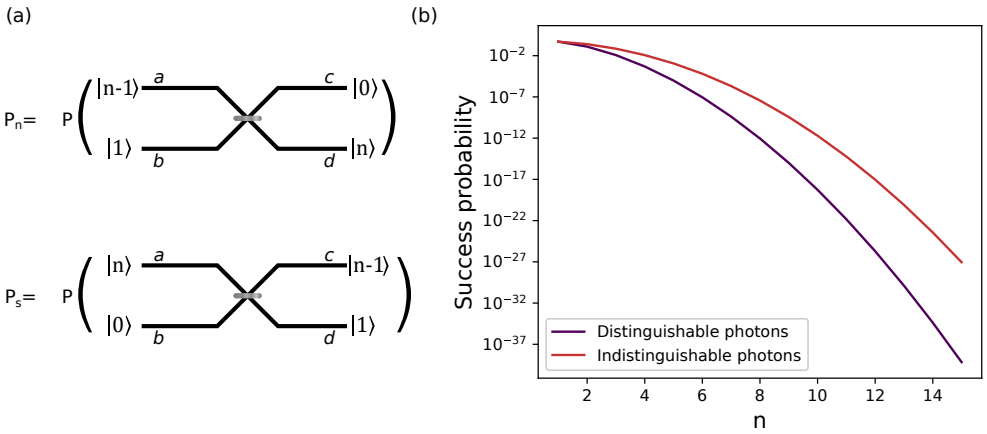

Figure 5.2.4: (a) Definition of the probabilities required to calculate the final success probability. (b)Success probability of indistinguishability purification, where n denotes the number of photons that are used by the protocol.

Calculating the increase in indistinguishability is slightly more complicated and can be done with many different models and depends on the type of indistinguishability to be modelled. The simplest way is to use the multi-dimensional permanent introduced in Chapter 2 to model distinguishability caused by fast errors. To compute the indistinguishability after the protocol, two photons generated by the protocol have to be interfered in a Hong-Ou-Mandel (HOM) experiment as illustrated in Figure 5.2.5 (a) for the simplest case of only one indistinguishability purification instance. The final indistinguishability can be extracted from the visibility of the experiment conditioned on the right detector pattern from both sides, where the visibility V and the the normalized coincidence probability P_{cc} are related as follows:

$$V = 1 - 2P_{cc}\,. \tag{5.2.8}$$

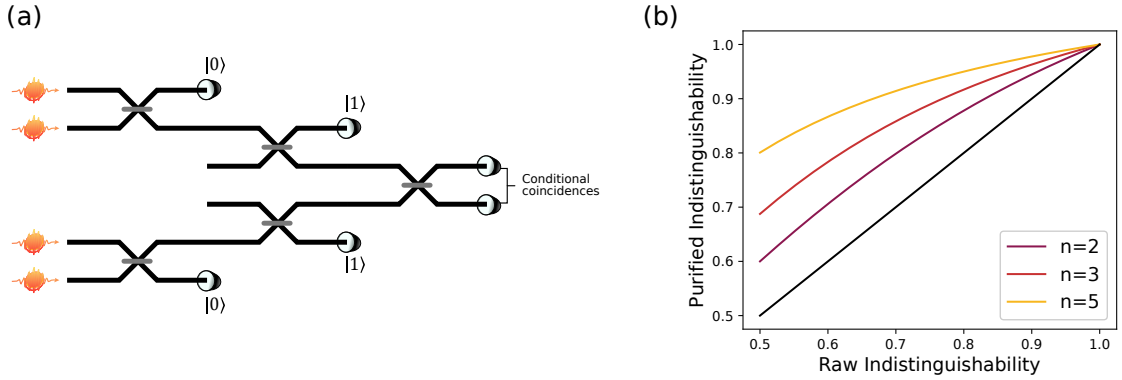

Figure 5.2.5: (a) To measure the final indistinsguishability for n=2, two copies of the setup are needed. A final beam splitter is added in order to measure the HOM visibility, from which the indistinguishability can be extracted. (b) Simulation results for different instances of indistinguishability compared to the orinal raw indistinguishability of the photons.

The final indistinguishability is shown in Figure 5.2.5(b), where the raw indistinguishability before purification is shown in the x-axis and the expected improved indistinguishability is shown in the y-axis. It is clear that higher instances of purification have a high influence on the final indistinguishability, and that there is most to be gained when the raw indistinguishability is low. This makes this protocol ideal for enabling multiphoton experiment with noisy single-photon sources.

Special note should be given to the fact that spectral filtering usually increases the indistinguishability of single photons significantly while only decreaseing the count rate with about 5-10%. On first sight this performs much better than our suggested indistinguishability purification protocol when it comes to efficiency versus improvement. Nontheless, spectral filtering has several limitations not faced by this protocol. First, spectral filtering is purely probabilistic and thus an intrinsic loss, which means that it

cannot be used to recover near-deterministic operation. Our approach does not face this limitation given that it is heralded and thus can be implemented through multiplexing of heralded events. Second, spectral filtering can reduce noise from phonon sidebands in quantum emitters and spectral detuning or correlations in spontaneous photon sources, but cannot correct for incoherent processes which happen at time scales shorter than the coherence time of the photons. Our proposed scheme should in principle be able to correct for both type of noises, making it the only sensible approach to achieve near-unity indistinguishability.

5.2.2 Indistinguishability models

The model used to generate the results above is a simplification assuming that all photons have a constant overlap between their wave packets from which the indistinguishability is defined. This model can be useful for simulating the case of applying the protocol to purification of photons generated from a single source which are mostly subject to pure dephasing, but its accuracy remains to be discussed. We will briefly introduce two other methods to do the same calculation and discuss the differences in the end.

Multipermanent model

We apply the multipermanent model described in Chapter 2 to get a numerical estimation of the output indistinguishability. Applying this model to our protocol, we compute the unitary matrix resulting from the $n = 2$ error mitigation scheme

$$M_U = \frac{1}{2\sqrt{2}} \begin{pmatrix} 2 & \sqrt{2}i & -1 & -i & 0 & 0 \\ 2i & \sqrt{2} & i & -1 & 0 & 0 \\ 0 & 2i & \sqrt{2} & \sqrt{2}i & 0 & 0 \\ 0 & 0 & \sqrt{2}i & \sqrt{2} & 2i & 0 \\ 0 & 0 & -1 & i & \sqrt{2} & 2i \\ 0 & 0 & -i & -1 & i\sqrt{2} & 2 \end{pmatrix} . \tag{5.2.9}$$

where we calculate the coincidence probability of the total output as

$$P_{\text{out}} = |\langle 0,1,1,1,1,0| U |1,1,0,0,1,1\rangle|^2 . \tag{5.2.10}$$

To compute the expected experimental HOM visibility this probability has to be normalized with the probability of getting the expected 4-photon configuration in the case where the photons do not interfere on the final beam splitter, which is calculated using the same method with the diference that the final beam splitter is replaced by an identity, we call this probability P_{ref}. The expected HOM visibility is then given by

$$V_{\text{HOM}} = 1 - \frac{P_{\text{out}}}{P_{\text{ref}}} . \tag{5.2.11}$$

Maximum and minimum purity model

The indistinguishability purification protocol discussed here was introduced by Sparrow in his PhD thesis [112], in which an analytical model was derived. The method used in that thesis to calculate the output indistinguishability relies on considering a photon as being in a mixed state of different modes $|\zeta_i\rangle$, such that the density matrix is

$$\rho = \sum_i p_i \left|\zeta_i\right\rangle \left\langle\zeta_i\right| . \tag{5.2.12}$$

Two photons will interfere perfectly if they are in the same mode and will not interfere if they populate orthogonal modes.

After a BS where vacuum is detected in one of the arms, the density matrix for the state in the remaining arm is

$$\rho = \frac{1}{N}\left(\sum_i p_i^2 (a_i^\dagger)^2[\zeta_i]\left|0\right\rangle \left\langle 0\right| a_i^2[\zeta_i] + \sum_{i\neq j} p_i p_j a_i^\dagger[\zeta_i] a_i^\dagger[\zeta_j]\left|0\right\rangle \left\langle 0\right| a_i[\zeta_i] a_i[\zeta_j]\right) , \tag{5.2.13}$$

where N is a normalization constant. After a second beam splitter and a projection on the state where one photon is detected on one arm, the remaining density matrix becomes

$$\rho' = \frac{1}{N}\sum_i p_i(p_i+1) a_1^\dagger[\zeta_i]\left|0\right\rangle \left\langle 0\right| a_1[\zeta_i] = \sum_i \frac{p_i(p_i+1)}{P+1}\left|\zeta_i\right\rangle \left\langle\zeta_i\right| , \tag{5.2.14}$$

where the purity P is defined to be

$$P = \sum_i p_i^2 . \tag{5.2.15}$$

In single photon experiments there is usually a dominant state $|\zeta_0\rangle$ with probability p_0. This probability is equivalent to the indistinguishability defined in eq. 5.2.8. The final indistinguishability will then be given by the probability of the state $|\zeta_0\rangle$ in eq. 5.2.14, which we denote as p_0'.

There are two extreme cases when calculating p_0', which are when the purity P is maximized and minimized. The purity is maximized in the case where there is only one extra possible state $|\zeta_1\rangle$, such that the density matrix is

$$\rho_{\max} = p_0 \left|\zeta_0\right\rangle \left\langle\zeta_0\right| + (1-p_0)\left|\zeta_1\right\rangle \left\langle\zeta_1\right| , \tag{5.2.16}$$

where $P = p_0^2 + (1-p_0)^2$. The purity is minimized if there is arbitrarily many possible states with vanishing probability such that $P = p_0^2$.

The indistinguishability after purification p_0' is calculated in both cases to be

$$p'_{0(\max)} = \frac{p_0(p_0+1)}{2[p_0(p_0-1)+1]} , \tag{5.2.17}$$

$$p'_{0(\min)} = \frac{p_0(p_0+1)}{2[p_0^2+1]} . \tag{5.2.18}$$

These curves are plotted in Figure 5.2.6

Physically inspired model

We also derived our own model in which a proper treatment of the mechanism responsible for pure dephasing is performed.

In this section we describe an analytical derivation for the simplest n=2 case of our protocol, where the appropiate dephasing mechanisms are taken into account in order to test the accuracy of the multipermanent model for our platform. The basics of this model were introduced in Chapter 2 and it is based on the methods described in [31]. The calculations were performed together with Andrew B. Villadsen and a step-by-step derivation can be found in his bachelor thesis [117].

We apply the formalism introduced in Chapter 2 to the $n = 2$ quantum error mitigation scheme presented in the main text, where we wish to find the coincidence probability of two photons that have gone through the mitigation circuit. Skipping all the middle steps, the coincidence probability at the end of the circuit is

$$P_\alpha = \frac{1}{2\left(1+\langle|\alpha_{ij}|^2\rangle\right)^2}\Big(1+\langle|\alpha_{ij}|^2\rangle+\langle|\alpha_{ij}|^2\rangle\langle|\alpha_{ij}|^2\rangle - 2\langle\alpha_{ij}\alpha_{jk}\alpha_{ki}\rangle-\langle\alpha_{ij}\alpha_{jk}\alpha_{kl}\alpha_{li}\rangle\Big) \tag{5.2.19}$$

It should be noted that for the final coincidence probability, there is an influence not only from the two photon indistinguishabilities, but also from the 3 and 4 photon indistinguishability instances. Following the logic from eq 2.2.11 we can write the final indistinguishability of the photons as

$$\langle|\alpha_f|^2\rangle = 1-2P_\alpha = \sqrt{\frac{x^3+5x^2+8x+3}{(2x+3)(x+1)^3}}\,, \tag{5.2.20}$$

where $x = \frac{\gamma_d}{\gamma}$.

Model comparison for n=2

It is time to compare the predictions of the 3 different models. Such a comparison can be found in Figure 5.2.6, with the raw indistinguishability on the x-axis and the expected improvement on the y-axis. It can be seen that the maximum purity model from Sparrow gives exactly the same predictions as the multi-permanent approach. The physically inspired model lies consistently in between the minimum and maximum purity models.

The physical interpretation of the difference between the models lies in the fact that even though the n=2 indistinguishability purification protocol is a two-photon experiment, the experiment to test it in practice is a 4-photon experiment. The multi-permanent and maximum purity models only take into account the pairwise indistinguishability between the photons, and thus come with the same prediction for the final outcome. The minimum purity and the pure-dephasing model on the other hand have

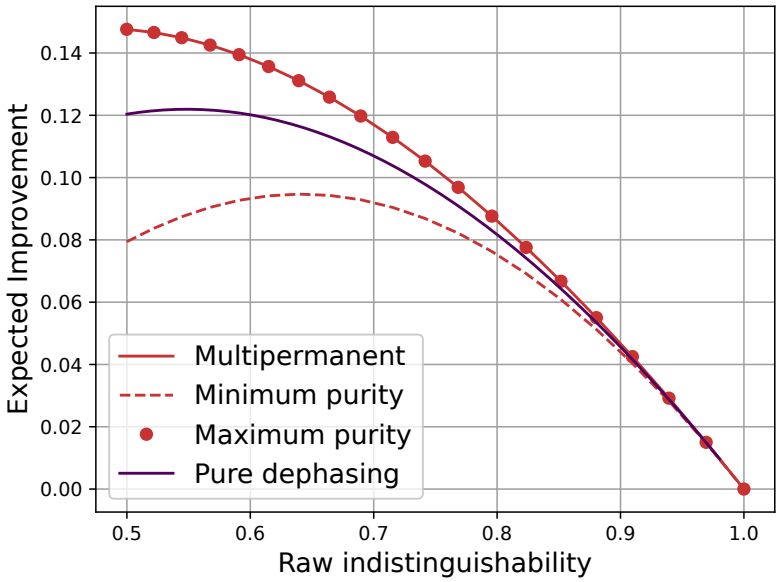

Figure 5.2.6: Comparison of the predictions of the three different models for n=2. The expected improvement is given by substracting the raw indistinguishability from the purified indistinguishability.

terms that rely on three and four-photon contributions, and take them into account in different ways, which is why their results differ.

5.2.3 Indistinguishability purification of multiple sources

We should also analyze how much improvement is expected when the photons come from multiple sources and are fed into the protocol correctly as shown in figure 5.2.3. As discussed previously, the added challenge when interfering multiple sources is that the slow errors suddenly become relevant as they will affect the photons from each source differently. In this section we will look into two sources of slow errors and analyze their effect on our protocol, these are polarization drifts and spectral diffusion.

Spectral diffusion

When working with quantum dot (QD) single-photon sources, the main source of slow errors come from spectral difusion, which is when charge noise from the environment slowly changes the energy of the two-level system. This source of noise can be included into the physically inspired model described above if the Δ_i term in eq. 2.2.9 is not set to zero. In which case we denote the two photon indistinguishability by $|\beta_{ij}|^2$ instead of $|\alpha_{ij}|^2$, and it can be calculated using the integral in eq. 2.2.10 to get

$$\langle|\beta_{ij}|^2\rangle = \frac{\gamma(\gamma+2\gamma_d)}{(\gamma+2\gamma_d)^2+\Delta_{01}^2}\,. \tag{5.2.21}$$

Since we use the quantity Δ_i to simulate spectral diffusion, it represents a quantity that varies over time and oscillates around zero, since spectral diffusion is mainly caused by small electric field fluctuations. We will assume that it's value at different times follows a gaussian distribution with standard deviation σ. In such case the average value for $|\beta_{ij}|^2$ becomes

$$\begin{aligned}\langle|\beta_{ij}|^2\rangle &= \int_{-\infty}^{\infty} \frac{\gamma(\gamma+2\gamma_d)}{(\gamma+2\gamma_d)^2+\Delta_{01}^2} \cdot \frac{1}{\sqrt{2\pi}\sigma} \cdot e^{-\frac{\Delta_{01}^2}{2\sigma^2}} d\Delta_{01} \\ &= \sqrt{\frac{\pi}{2}}\frac{\gamma}{\sigma}\mathrm{erfc}\left(\frac{\gamma+2\gamma_d}{\sqrt{2}\sigma}\right) e^{\frac{(\gamma+2\gamma_d)^2}{2\sigma^2}} \\ &= \sqrt{\frac{\pi}{2}}\frac{1}{y}G\left(\frac{2x+1}{\sqrt{2}y}\right),\end{aligned} \tag{5.2.22}$$

which is the indistinguishability that would be extracted from a HOM measurement between two quantum dots, where we have defined

$$G(a) = \mathrm{erfc}(a)e^{a^2}\,. \tag{5.2.23}$$

Calculating the final indistinguishability after the protocol can be done very similarly to the one quantum dot case, except that due care should be taken as to which instances of indistinguishability should be used. The equivalent to eq. 5.2.19 in this case becomes

$$\begin{aligned}P_\beta = \frac{1}{4\left(1+\langle|\beta_{ij}|^2\rangle\right)^2}\Big(&2+3\langle|\beta_{ij}|^2\rangle+2\langle|\beta_{ij}|^2\rangle\langle|\beta_{ij}|^2\rangle-\langle|\alpha_{ij}|^2\rangle-4\langle\beta_{ij}\beta_{jk}\alpha_{ki}\rangle \\ &-\langle\beta_{ij}\alpha_{jk}\beta_{kl}\alpha_{li}\rangle-\langle\beta_{ij}\beta_{jk}\beta_{kl}\beta_{li}\rangle\Big),\end{aligned} \tag{5.2.24}$$

where computing the integrals for the higher indistinguishability integrals and using

eq. 5.2.8 yields the final equation for the indistinguishability to be

$$|\beta_f| = \frac{\sqrt{10}}{\sqrt{y(2x+3)}(x+1)(2x+1)\left(\sqrt{2\pi}\,G\left(\frac{2x+1}{\sqrt{2}y}\right)+2y\right)}$$

$$\cdot\Bigg\{\frac{y}{5}\Bigg[yx^2\sqrt{2\pi}(x+\tfrac{3}{2})(x^2+\tfrac{5}{3}x+\tfrac{3}{4})G\left(\tfrac{2x+3}{\sqrt{2}y}\right) \tag{5.2.25}$$

$$-\tfrac{2}{3}yx\sqrt{2\pi}(2x+1)(11x+18)(x+1)^2\,G\left(\tfrac{\sqrt{2}(x+1)}{y}\right)$$

$$+(2x+3)\left(\tfrac{5}{2}x^4+\tfrac{(8y^2+31)}{4}x^3+\tfrac{(41y^2+65)}{8}x^2+\tfrac{(69y^2+57)}{16}x+\tfrac{(17y^2+9)}{16}\right)\Bigg]$$

$$-\sqrt{2\pi}\left(x+\tfrac{1}{2}\right)\Bigg(x^5+\tfrac{(69-47y^2)}{15}x^4+\tfrac{(79-143y^2)}{10}x^3+\tfrac{(378-1339y^2)}{60}x^2+\tfrac{(189-1278y^2)}{80}x \tag{5.2.26}$$

$$+\tfrac{(27-306y^2)}{80}\Bigg)G\left(\tfrac{2x+1}{\sqrt{2}y}\right)\Bigg\}^{\frac{1}{2}},$$

where we have defined $y = \frac{\sigma}{\gamma}$ as the variable that represents the ammount of spectral diffusion.

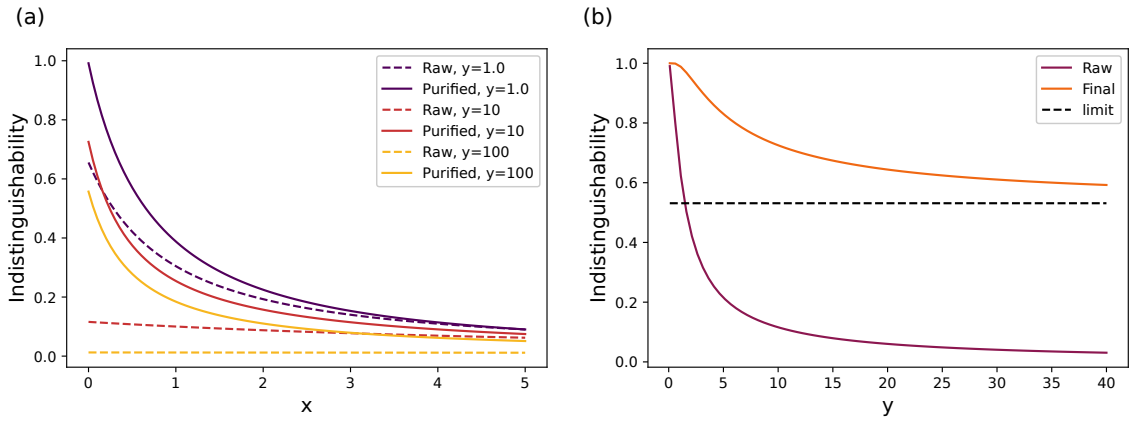

Figure 5.2.7: (a) Expected indistinguishability in the two quantum dot case for different values of the dephasing variable x. The raw lines come from the visibility of photons from the two dots on a beam splitter. (b) Expected indistinguishability in the two quantum dot case for different values of the spectral diffusion variable y in the limit where there is no pure dephasing such that $x = 0$. The final indistinguishability goes towards the limit of $\sqrt{17/32}$.

The final indistinguishability is compared to the initial one for different values of x and y in figure 5.2.7 (a). It can be seen that our protocol always increases the indistinguishability no matter the conditions, and even if spectral diffusion creates

high distinguishability between the photons, the final indistinguishability after the protocol remains high. This can be appreciated even more in figure 5.2.7(b), where the effect of spectral diffusion has been isolated by setting $x = 0$, and it can be seen that even if the initial indistinguishability goes towards zero, the indistinguishability after the protocol goes towards a fixed value of 17/32. This value should be noted to be very close to 1/2, which corresponds to a HOM visility of 50%.

Polarization drifts

The other error than can arise when interfering photons from different sources is polarization drifts, which can happen particularly if the photons travel through very long fibers before they interfere. We will now analyze how well our protocol can correct for such errors.

The effect of polarization on an interferometer experiment can be readily analyzed by creating a copy of the interferometer which represents the interference between photons of two orthogonal polarizations, as illustrated in Figure 5.2.8 (a). In this model, a beam splitter with a certain reflectivity represents the probability of the photons acquiring an orthogonal polarization. If the BS is 50:50 it corresponds to comparing horizontal (H) with diagonal (D) polarized light. The extra phaseshifter in the lowest arm is there such that the case where there D polarized light on one arm but anti-diagonal (A) polarized light on the other can also be simulated. If the added phase is 0, then we simulate having D polarized light on both arms, while we simulate A polarized light if the phase is π.

The results of the simulation with the model described can be seen in Figure 5.2.8(b). The upper bound is obtained when the phase shifter induces $\phi = 0$, and the lower bound when it is $\phi = \pi/2$. Physically these limits correspond to the photons from the second quantum dot arriving with either the same polarization or with opposite polarizations. It can be seen that the indistinguishability always improves, and that it improves the most when the polarizations of the photons from the two sources are orthogonal.

We can now conclude that accordding to all our simulations, the distinguishability purification protocol should improve the indistinguishability of any single photon source, regardless of the error type, and it is even more efficient to mitigate errors that give rise to distinguishability between multiple sources.

5.2.4 Simulation of errors

This subsection was reproduced with minor adjustments from the supplementary material of [32].

Multiphoton contributions. The multiphoton contribution of a single photon source is quantified by the $g^{(2)}(0)$ value. In this section we analyze the influence of a non-zero $g^{(2)}(0)$ on our error mitigation scheme. For this analysis we will assume that there are no three-photon emissions from the two level emitter, as in our experiment this is highly unlikely to happen. Thus the $g^{(2)}(0)$ value is directly related to

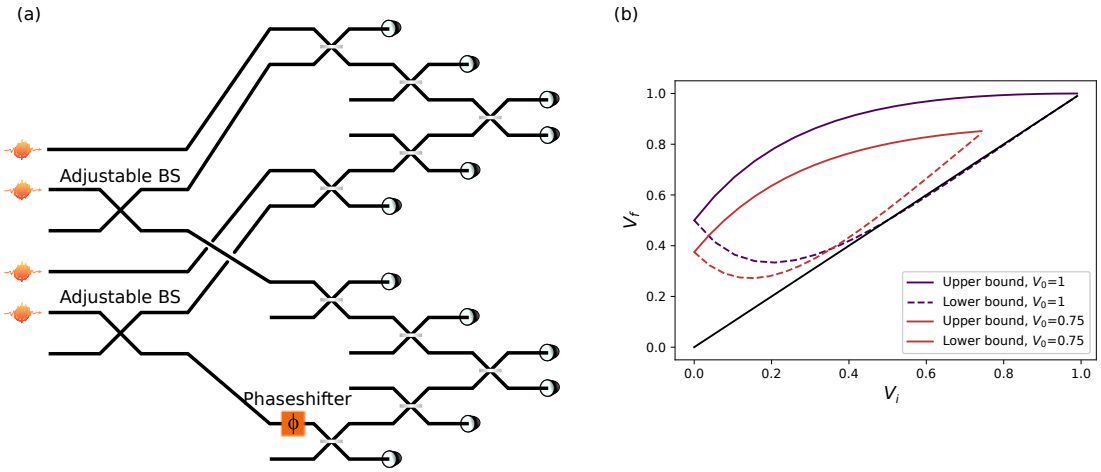

Figure 5.2.8: (a) Sketch of the circuit used to simulate indistinguishability purification of two quantum dots with different polarizations. The adjustable beam splitters (BS) can do any rotation between identity and swap to simulate polarization going from H to V. The phaseshifter is analogous rotations on the XY plane of the Bloch sphere. (b) Simulation of the improvement for different polarizations. We denote V_0 as the raw indistinguishability of the single quantum dots, V_i as the indistinguishability resulting from a direct HOM visibility experiment between the dots, and V_f as the final indistinguishability after the protocol.

the probability of a two-photon state P_2. The direct relation can be calculated from eq. (1) in [118], which gives a relation for the multi-photon probability P_m with the $g^{(2)}(0)$ and the multi-photon probability B

$$P_m \leq \frac{1 - Bg^{(2)}(0) - \sqrt{1 - 2Bg^{(2)}(0)}}{g^{(2)}(0)} \,. \tag{5.2.27}$$

We can set $B = 1$, as the probability of a click to unity given that we can only analyze the events where a detection happened, and we also truncate $P_{n>2} = 0$ such that $P_2 = 1 - P_1$ and $P_m = P_2$, we arrive at the relation

$$P_2 = \frac{1 - g^{(2)}(0) - \sqrt{1 - 2g^{(2)}(0)}}{g^{(2)}(0)} \,. \tag{5.2.28}$$

Our simulation consists of calculating the coincidence probability between the final two detectors given a certain value for the $g^{(2)}(0)$ and the indistingusihability of the photons. In the case where there are no events with three or more photons, the total probability P_T is given by the sum the binomial coefficients for the possible two-photon configurations at the input, such that

$$P_T = \sum_{\eta=0}^{2n} (1 - P_2)^{2n-\eta} \cdot P_2^{\eta} \cdot P_{\eta} \,, \tag{5.2.29}$$

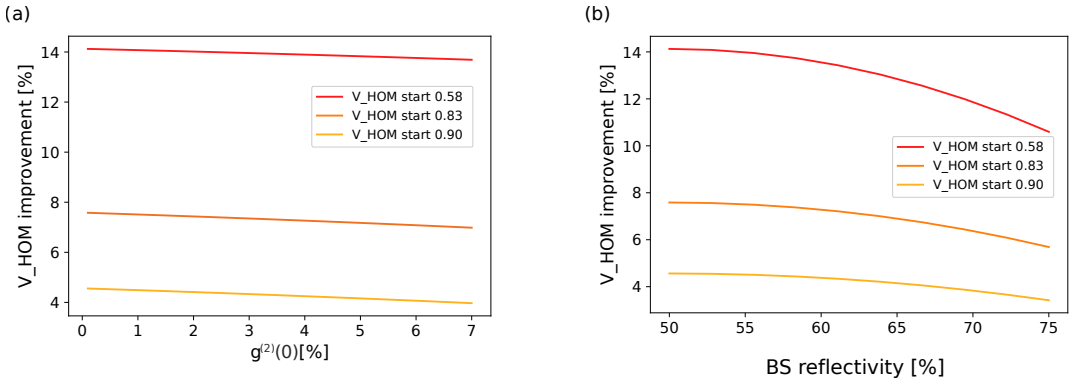

Figure 5.2.9: (a)Influence of multiphoton contributions on the expected HOM visibility improvement. (b) Influence of having imperfect beam splitters on the protocol.

where η is the amount of two-photon states considered in a given step of the simulation, P_η is the probability to get a coincidence given η and n is the number of photons being used for a single purification circuit. We calculate P_η using the multipermanent model described in eq. 2.2.13 and 2.2.17, such that

$$P_\eta = \sum_{\alpha(\eta)} \sum_{\beta(\eta)} |\langle \alpha(\eta)| U |\beta(\eta)\rangle|^2 , \tag{5.2.30}$$

where α and β represent a given output and input configuration. For the input configuration, the summation goes over all of the combinations of η double photon positions distributed over $2n$ total inputs. For the output configuration, the sum goes over all of the output states that would give the same signal in our non-photon number resolving detectors.

To calculate the expected HOM visibility we also compare to the reference probability where the final beam splitter is replaced by an identity as in eq. 5.2.11.

We performed a simulation of the expected influence of the $g^{(2)}(0)$ value using the described model and the results can be seen in Fig. 5.2.9(a). It can be seen that a high $g^{(2)}(0)$ value will slightly decrease the expected visibility improvement, but the effect is not very pronounced. The $g^{(2)}(0)$ value for the measurements with the etalon was of 2 % while it was of 7 % without the etalon. Thus we expect the influence to be negligible with the etalon.

On the other hand, in an experimental setup there is no easily accessible way to extract the intrinsic HOM visibility value without it being influenced by the $g^{(2)}(0)$. This is a complex matter which depends highly on the type of photons that are contained in the multi-photon component [119]. The intrinsic HOM visibility may thus actually be better or worse than expected depending on the $g^{(2)}(0)$ value and the type of multi-photon components. An accurate evaluation of how to calculate this properly requires further theoretical inquiry of the protocol.

Imperfect beam splitter contributions. Having lossy, unbalanced or asymmetrical beam splitters can sometimes make a difference in the measured HOM visibility as

these errors may affect the side-peaks differently than the central peak.

We can simulate the influence of this error by changing the splitting ratio in the construction of the unitary matrix that simulates the circuit. We found that changing the splitting ratio of the first or the second BS did not have any influence on the final HOM visibility. The splitting ratio of the final BS on the other hand does have an influence on the final indistinguishability. This is applies both for the raw and the purified value of the visiblity, but the influence is more pronounced for the purified value. The expected difference between the HOM visibility before and after purification are plotted Figure 5.2.9(b). It can be seen that for highly imperfect reflectivities of the final BS, the expected improvement will be lower than expected. In our experiment we strived to install a BS with a close-to-50:50 splitting ratio for the final BS. The reflectivity is dependent on the polarization, and since this is tuned for every run of the experiment, an exact value is hard to provide. However, we are confident that the reflectivity is between 45 and 55 %, for which according to the simulation, the influence on the visibility improvement should be negligible.

Loss contributions. Losses can influence the calculated indistinguishability as they affect the side-peaks of a two-photon correlation measurement differently than they affect the central peak. We explain this in more detail in the data analysis section. Even though they have an influence, their effect is measurable since it is possible to know the loss rate of the system, and it can be taken into account in the data analysis.

We can thus conclude that photon losses should have negligible influence on the expected visibility improvement.

5.2.5 Other indistinguishability purification protocols

The indistinguishability purification presented so far is not the only one there is, but it was the first one to be proposed, and it was the only one available at the time we started planning the experiment, which is why this thesis is focused on that protocol. There are at the time of the publication of this thesis three other theoretical works with indistinguishability purification protocols

- Marshal et al. [113] describes a protocol that requires 3 photons to output one indistinguishable photon. It has better efficiency than the $n = 3$ protocol described in this thesis, but lower indistinguishability improvement.

- Saied et al. [120] proposes a number of new multi-photon indistinguishability purification protocols with better scaling with respect to n compared to the protocol described in this thesis.

- Somhorst et al. [121] proposes an indistinguishability purification protocol inspired by discrete Fourier transform, and show that their scheme is asymptotically optimal in error reduction per photon consumed as the number of photons increases.

5.3 Time-domain experiment

Having studied the theory behind indistinguishability purification and the predictions given by different models, we will now describe the first experiment we performed to show the protocol experimentally. This experiment did not produce any valuable data due to error sources that will be discussed later in the section. We still think that negative results are valuable to present as we learned a lot in the process. For more positive results we recommend for the reader to skip to the next section.

The idea behind the time-domain experiment was to build a setup that could perform an arbitrary number of purification instances without changing the physical setup, i.e. by having an electronically controlled optical switch determine the number of instances. This process is illustrated in Figure 5.3.1(a). The first variable beam splitter is responsible for letting the first photon directly into the delay loop, and then serve as the BS responsible for the purification at later times. It is therefore set to swap during the arrival of the first photon, then to 50:50 splitting and finally to swap again to let the purified multi-photon state out. The second variable BS has the function of being an identity such that the zero detections can be performed and convert into a 50:50 BS when the multi-photon state arrives to implement the separation part of the protocol.

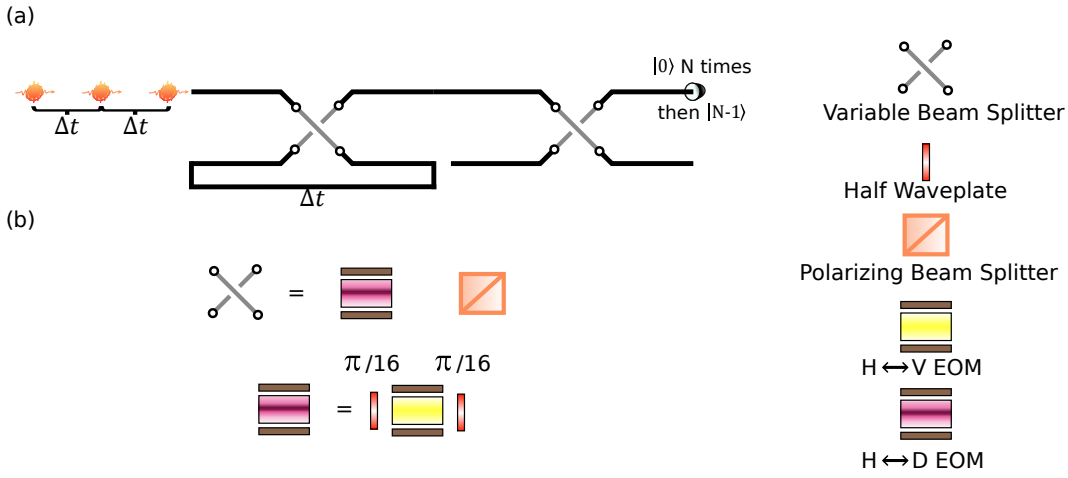

Figure 5.3.1: (a) time-domain setup concept illustration. The variable first variable beam splitter (BS) starts as a swap, which then is changed into a 50:50 BS. The second starts as an identity and is changed into a 50:50 BS after N instances of purification.(b) (top) Working principle of the variable beam splitter with polarization optics. (bottom)The rotation created by an EOM when it is on can be changed by adding waveplates with the right rotation angle before and after it.

When doing experiment in bulk optics, the leading approach to implement switches is through electro-optic modulators (EOMs), as they can have fast modulation speeds

and low losses. We had 3 ultra-low loss EOMs available at the time we designed the experiment, which means that it was possible to implement the scheme in Figure 5.3.1(a). Our EOMs work as a half waveplate at an angle of $\pi/4$ with respect to H polarization when they are on, meaning that they flip H to V and opposite when they are on, but do nothing to D, A, clockwise (C) or counterclockwise (CC) polarized light (except for applying phase-shifts), and do not alter the light when they are off. A switch can then be constructed using an EOM and a polarizing beam splitter (PBS), where H polarized light gets transmitted and V polarized light gets reflected.

A PBS also serves as a BS that transforms between path and polarization encoding. An easy way to picture this is with a D and an A-polarized photon going into the same input of a PBS.

$$|D_0 A_0\rangle = a_0^\dagger[D] a_0^\dagger[A] \,|0\rangle = \frac{1}{2}(a_0^\dagger[H]+a_0^\dagger[V])(a_0^\dagger[H]-a_0^\dagger[V]) \,|0\rangle = \frac{1}{\sqrt{2}}(|H_0 H_0\rangle+|V_0 V_0\rangle)\,, \tag{5.3.1}$$

where we use the notation that a subscript denotes a path mode and a letter within square parenthesis denotes a polarization mode. The last equality only holds in the photons are indistinguishable. In this case a PBS will create bunching into the output spatial modes if the photons are indistinguishable,

$$\frac{1}{\sqrt{2}}(|H_0 H_0\rangle + |V_0 V_0\rangle) \xrightarrow{\text{PBS}} \frac{1}{\sqrt{2}}(|H_2 H_2\rangle + |V_3 V_3\rangle)\,, \tag{5.3.2}$$

where 0(, 1) denotes the input modes and 2, 3 denote the output modes of the PBS, while randomly distributed outputs if the photons are distinguishable.

If we had an EOM that transformed H, V polarized light into D,A polarization we could construct the circuit in figure 5.3.1(a) with fewer optical components. Our EOMs cannot perform this transformation by default, but if the polarization is rotated using waveplates before and after it enters the EOMs, the desired transformation can be achieved. Figure 5.3.1(b) shows a setup implementing the desired transformation by using half-wave plates rotated by $\pi/16$ with respect to the horizontal axis.

5.3.1 Experimental setup

We generate single photons using semiconductor quantum dots (QD) embedded in photonic-crystal waveguides. A thorough description of the quantum dot and the optics used to collect the single photons can be found in chapter 4.

The single photons are sent to a bulk optics setup through an optical fiber. Using the HWP-EOM-PBS combination to implement on demand BSs, the circuit of Figure 5.3.1(a) can be implemented experimentally as illustrated in Figure 5.3.2(a). We use non-resonant electro-optical modulators (EOMs) as switches.

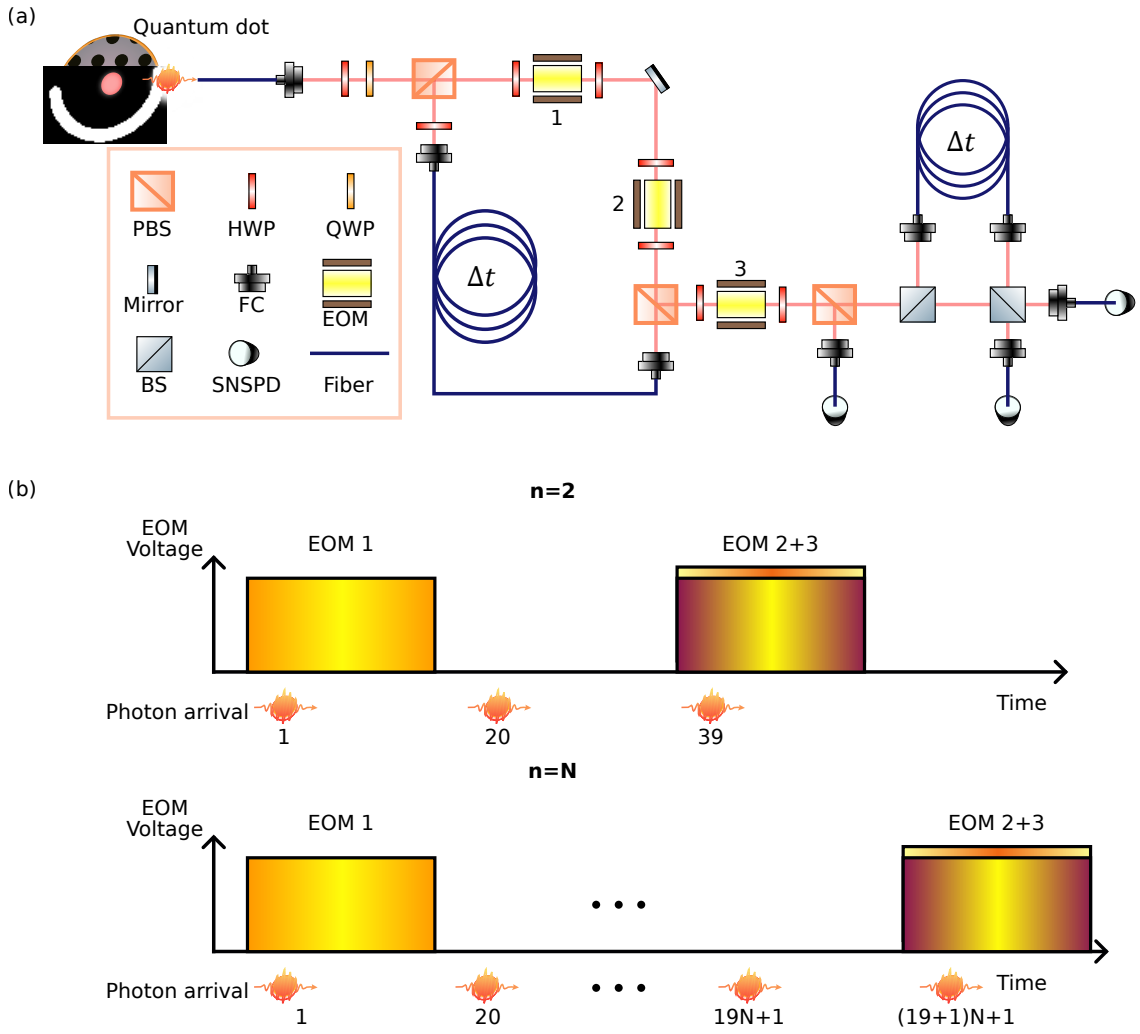

Figure 5.3.2: (a) time-domain experimental setup in practice. Δt denotes the time between two photon trains. PBS: Polarizing beam splitter, HWP: half-wave plate, QWP: quarter-wave plate, FC: fiber coupler, EOM: electro-optic modulator, BS: beam splitter, SNSPD: superconducting-nanowire single-photon detector.(b) Pulse sequence administered to EOMs for different purification instances compared to the arrival time of the photons.

The EOMS work by applying a voltage to a Pockels cell, which will make the crystal inside birefringent while the voltage is running, and transparent when there is no voltage. The high voltage required to modulate ultra-low loss non-resonant EOMs makes it a technical challenge to drive them with a high frequency. Our EOMs had a maximum modulation frequency of 1 MHz. There is also a limitation on the time they can be on compared to the duty cycle (the time of a full cycle), and that they can only turn on once per cycle. By experience we found this limit to be 26% of the

duty cycle before they risk breaking. The original purpose of the EOMs was to create a 4 mode demultiplexer, which is why we had three of them available. In a four mode demultiplexer, the duty cycle limitation is not a problem as they maximally need to be on once and for 25% of the time in the protocol. The frequency limitation can be circumvented by making trains of demultiplexed photons instead of single instances, with the only disadvantage that the delays have to be longer. These limitations pose a bigger challenge to the experiment we wanted to do, which requires 2 EOMs, but one of them needs to be able to turn on twice during the duty cycle. This challenge can be circumvented by using 3 EOMs, such that they all only need to be on once during the duty cycle.

Ideally the fiber delays should be adjusted to match the repetition rate of the single photons, but since the repetition rate of our experiment is limited by the maximal frequency of the EOMs, the length of the fibers is set to match the duration of the photon trains resulting from the EOM signals. This in our case corresponded to a delay of 290 ns, in order to delay a train of 19 photons separated by 13.7 ns each. The final adjustments for the delay length are done by moving the position of the mirrors and the fiber coupling lens in the free space setup.

The timing when the EOMs are on determines the specific protocol to be applied, as EOMs 2 and 3 are the ones to determine when the purification phase is over and the separation has to be done. Figure 5.3.2(b) illustrates the pulse sequence given to the EOMs and how it relates to the number of purification instances that it corresponds to in practice.

After the separation setup the photons are sent to a free space HOM setup (see Chapter 4 Figure 4.2.6) in order to measure the final indistinguishability of the photons. This is also illustrated in figure 5.3.2(b). We use superconducting-nanowire single-photon detectors (SNSPDs), which are also described in greater detail in Chapter 4.

5.3.2 Experimental results

The simplest experiment to test our protocol is in the case for n=2, which requires a 4 photon experiment to be proven advantageous. Given our single photon rates, a 4 photon experiment would be a lengthy measurement and we decided to start with an even simpler experiment to test the setup before committing to long-integration-time measurements. Given that the $g^{(2)}(0)$ is directly related to the measured HOM visibility, it is relevant to measure the $g^{(2)}(0)$ of the photons before and after the indistinguishability purification setup.

The $g^{(2)}(0)$ of the unpurified photons can be readily measured by using a beam splitter and measuring the ratio of coincidence counts at zero time delay with the coincidence counts of one of the side-peaks. We did not observe significant blinking in this QD sample, so comparing the central peak to some of the near side peaks can give an accurate value for the $g^{(2)}(0)$. To measure the $g^{(2)}(0)$ after indistinguishability purification we replace the HOM setup in figure 5.3.2(b) with a beam splitter. It is

then possible using post-selection to measure the $g^{(2)}(0)$ of the events where a 0-photon state and a 1-photon state were recorded.

The resulting histograms for the two HBT experiments are shown in Figure 5.3.3. The $g^{(2)}(0)$ computed from Figure (a) is

$$g^{(2)}_{raw}(0) = 3.0 \pm 0.1\% \,, \tag{5.3.3}$$

while the value after purification was computed to be

$$g^{(2)}_{purified}(0) = 8.7 \pm 0.7\% \,. \tag{5.3.4}$$

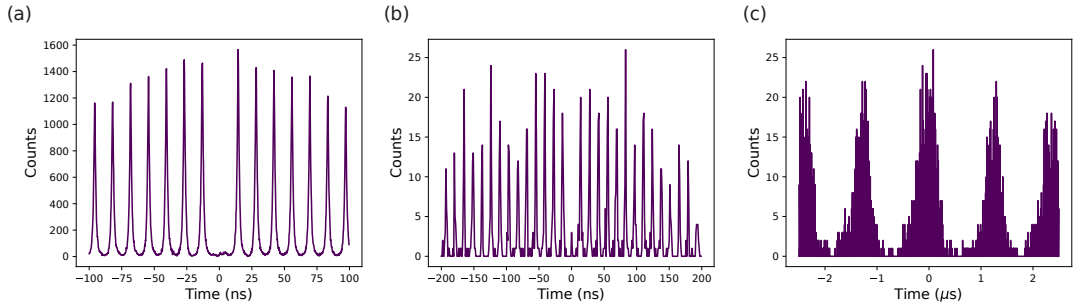

Figure 5.3.3: Preliminary results for the time-domain experiment. (a) $g^{(2)}(0)$ before purification. (b) $g^{(2)}(0)$ after purification (c) $g^{(2)}(0)$ after purification zoomed out

It can be seen that the $g^{(2)}(0)$ value increases significantly due to the indistinguishability purification setup. This is an unacceptable error as it would equally decrease the final value of the HOM visibility, contradicting the purpose of the setup. It was therefore important for us to find the source of the error and methods to mitigate it.

The first test was to block the delay and remove the waveplates before and after the EOM. Measuring the $g^{(2)}(0)$ of the photons in this case gave us exactly the same result as measuring it directly after the source. The we proceeded to unblocking the delay, and measuring the $g^{(2)}(0)$, and finally we included the two HWPs. The following table shows the $g^{(2)}(0)$ value measured under different conditions for the setup.

Measurement	$g^{(2)}(0)$ no fix	$g^{(2)}(0)$ with fix
Source and BS	3 %	2 %
Setup, blocked delay	3 %	2 %
Setup, no WPs	27 %	2 %
Setup	49 %	14 %
After postselection	8 %	-

The fact that unblocking the delay increased the $g^{(2)}(0)$ value significantly hinted at the fact that the fidelity of the PBS to direct light with a certain polarization into the right path was low. After doing some quick characterization of our PBSs we

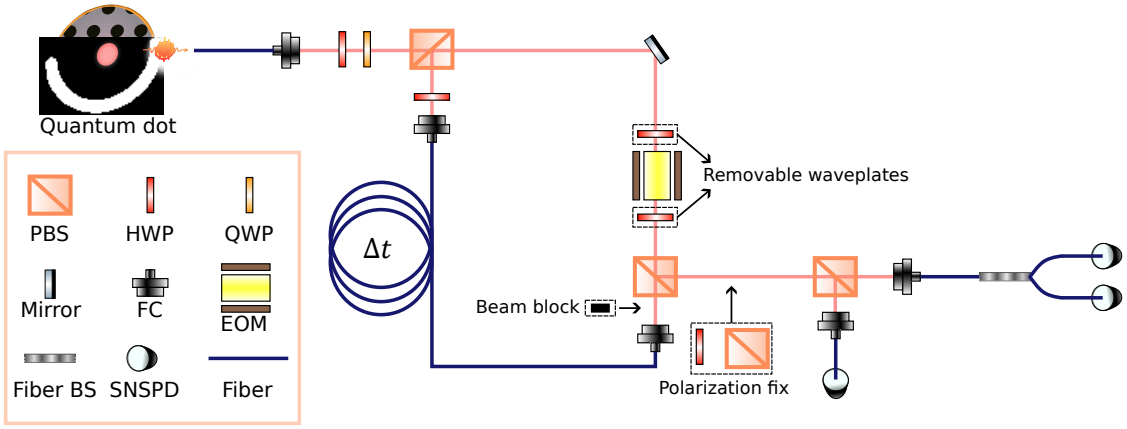

Figure 5.3.4: Experimental setup for measuring the $g^{(2)}(0)$. The marked areas are the ones that where removable in order to find the source of the error. PBS: Polarizing beam splitter, HWP: half-wave plate, QWP: quarter-wave plate, FC: fiber coupler, EOM: electro-optic modulator, BS: beam splitter, SNSPD: superconducting-nanowire single-photon detector

found that their error rate could be as high as 5% for the reflected beam, but usually below 1% for the transmitted beam. A quick way to fix this issue was to add an extra PBS to sort out the photons that resulted from an error in the first PBS. The placing of the extra PBSs is illustrated in figure 5.3.4. After the quick fix, we repeated the measurements of $g^{(2)}(0)$ under different conditions and the results can be seen on the right column of the table above. It can be appreciated that unblocking the delay did not worsen the measured value, meaning that the error stemming from the PBS was succesfully eradicated. Unfortunately the error stemming from the HWPs at each side of the EOM was not eradicated and a significant increase in the $g^{(2)}(0)$ value was still present. At this point we decided to give up pursuing this approach for indistinguishability purification, as we could not think of a way to remove the error caused by the HWPs.

5.3.3 Discussion

There are two ways to improve upon our experiment in order for it to be doable. The first would be to have EOMs that can execute the necessary rotation without the need of the extra HWPs. Such EOMs exist but due to their price and very limited utility we could not afford to buy them.

The second way to make the experiment viable would be to use path based BSs (either fiber or free space) for the purification procedure, instead of using PBSs. This would require a slight redesign of the experimental setup, and the suggested design can be seen in Figure 5.3.5.

Even though we did not manage to show indistinguishability purification with our

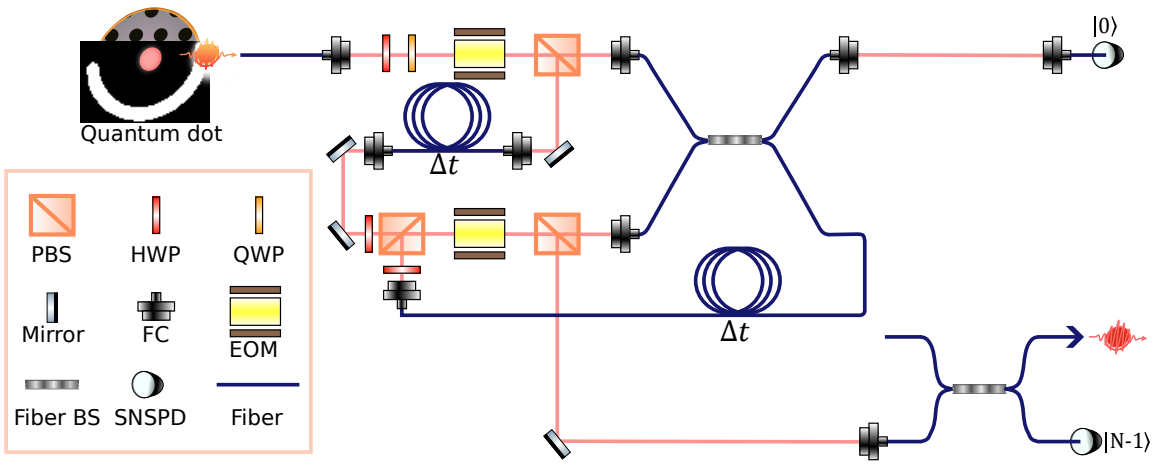

Figure 5.3.5: Recommended time-domain experiment with the experimental equipment that was available to us with the extra addition of two fiber based beam splitters. The pulse sequence to be administered to the EOMs is the same as that in figure 5.3.2(b).

time-domain experiment, we managed to find the sources of errors and we believe that if these are addressed correctly as we have suggested, time-domain indistinguishability purification should be possible and has many advantages compared to path demultiplexed based experiments.

The first advantage is that there are fewer polarization errors when doing free space optics, as polarization only drifts in fibers and it is easier to control it using wave-plates rather than fiber-polarization controllers. Another advantage compared to a demultiplexing-based setup is that there are fewer fiber delays required, which allows for fewer errors in the arrival time of the photons. The last advantage is in the hardware requirements of the experiment, which in a demultiplexing-based setup increase linearly as the number of purification instances increase while they remain constant in a time-domain setup with the possible exception of needing more detectors for pseudo photon-number resolution.

Another advantage of the setup in Figure 5.3.2(a) worth mentioning is the way the final HOM visibility experiment is performed. Changing the length of the delay of the HOM experiment from matching the repetition rate of the photons to matching the repetition rate of the inditinguishability purification protocol allows for measuring the final indistinguishability without having to create a physical copy of the setup. Alternatively, our implementation of the protocol where the time bins are composed of photon trains instead of single photons allows to use the HOM setup without the need to alter the delay, as the purified photons come with the same repetition rate as the single photons, but only at the end of the duty cycle given by the EOMs.

5.4 Space-domain experiment

In this section I will describe the experiment I performed during my external stay in the University of Vienna. This work was done in close collaboration with Lorenzo Carosini and other researchers from Philip Walthers' group. Some of the text and figures from this section are reproduced with minor adjustments from [32].

The simplest way to test indistinguishability purification is to replicate the circuit in Figure 5.2.5(a) with fiber beam splitters (BSs). The requirement to make this work is to have 4 photons arriving simultaneously at the input arms of the circuit. This requires a spatial 4-mode demultiplexer, which is why we call this experiment the space-domain experiment. In this section we will describe the experimental setup required for such an experiment, the results obtained and discuss how indistinguishability purification is efficient for different noise sources in single photons.

5.4.1 Experimental setup

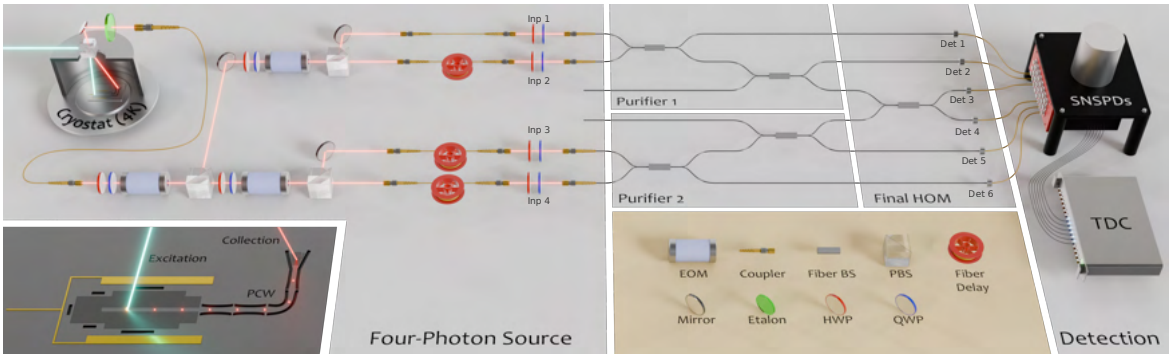

Figure 5.4.1: The single-photon source (inset) is an InAs QD coupled to a GaAs PCW, gated via metal electrical contacts (depicted in gold), kept at 4 K inside a cryostat. An etalon serves as a frequency filter, eliminating phonon side-bands to maximize photon indistinguishability. The emitted single-photon stream is routed into four spatial modes through a free-space demultiplexer, generating sets of four simultaneous input photons. Fiber-based temporal delays precede a final free-space setup, ensuring precise polarization control and enabling artificial delays before the purification stages. (Center) Two copies of the indistinguishability purification circuit are implemented through fiber beamsplitter (BS), and the outputs interfere at a final BS to test the indistinguishability of purified photons. (Right) Output configurations are measured through six superconducting nanowire single-photon detectors (SNSPDs) and a time-to-digital converter (TDC) to process their time-tags. This Figure and its caption was reproduced from [32].

A schematic of the full experimental set-up, which implements two copies of the $n = 2$ purification circuits and performs quantum interference between the two purified

outputs, is shown in Figure 5.4.1. The setup consists of a quantum dot (QD) single-photon source (SPS) followed by a four mode demultiplexer. The photons are then interefered according to the indistinguishability purification protocol using fiber BSs and finally detected using SNSPDs and a time tagger to analyze the data.

Single photon source

Deterministic single-photon generation is achieved from a neutral exciton of an InAs QD embedded in photonic crystal waveguide (PCW), detailed in the bottom left inset of Figure 5.4.1. For more details about QDs in PCWs we refer to Chapter 4. The QD is pumped resonantly with a pulsed laser, spectrally shaped with a 4-f system, to set a bandwidth of ∼90 pm and match the QD wavelength λ=938.4 nm.

Electrical tuning of the QD, facilitated by low-noise electrical contacts, stabilizes the charge state, ensuring emission on the desired transition and minimizing spectral diffusion due to residual charge noise [122, 16]. Even though this tuning should in principle only influence the output wavelength of the emitted photons, it can have an influence on the indistinguishability of the emitted photons, as co-tunnelling of carriers from the contacts can create slight shifts in the frequency of the emitted photons. For this it is important that the voltage applied is not near the edge of the charge plateau for the quantum dot in use.

The single photons are emitted in the PCW and fiber-coupled via a shallow-edged grating and a cryo-compatible objective lens. An etalon with a bandwidth of 32 GHz can be employed as a frequency filter to optimize the indistinguishability of emitted photons by removing the undesired phonon-induced spectral sideband.

Pumping the QD with resonant π-pulses at a repetition rate of 80 MHz yields single photons at a measured rate of 16.1 MHz (with an 85% efficient detection system), corresponding to a 23.7% fiber-coupled efficiency of the single-photon source, and purity of $1 - g^{(2)}(0) = (97.21 \pm 0.01)\%$.

Four-mode demultiplexer

The photon stream is then converted into four streams of simultaneous photons in different spatial modes through a time-to-space demultiplexing module illustrated in the center-left of Figure 5.4.1.

Depending on the type of EOM, there can be two types of demultiplexers. For non-resonant EOMs it is common to use them for cascaded demultiplexers, where a single photon at a time is removed from the main path and sent to a different delay. At the NBI we had a cascaded demultiplexer, and a rough sketch of the setup can be seen in figure 5.3.2(a), where the setup becomes a demultiplexer if the first mirror is replaced by a PBS and fiber couplers followed by the correct delays are placed. For the experiment in Vienna we had resonant EOMs available, for which a tree-like structure is required.

As shown in Figure 5.4.1, the demultiplexer consists of three resonantly-enhanced electro-optic modulators (EOMs) and polarising beamsplitters (PBSs) [123, 19] to

route the photons in four different output modes and with different fiber lengths to compensate for the temporal delays. At this stage, we detect four-photon coincidences at a rate of 3.2 kHz.

An additional free-space coupling is introduced before feeding into the fiber-based HOM interferometers to control the arrival time and polarization of the photons. To make sure that the photons arrive exactly at the same time, a calibration procedure previous to the experiment is performed: We feed the excitation laser into the demultiplexer and try to achieve classical interference on a fiber BS. The fiber couplings after the demultiplexer are mounted on translation stages such that the exact point of the coupling can be changed to micrometer precision. The output of the fiber BS is sent to a spectrometer, which will show a constant peak when there is no interference and a peak of oscillating amplitude when there is interference. Since the pulse width of the laser is in the order of tens of femtoseconds, seeing interference means that the photons arrive simultaneously within a time that is much shorter than their lifetime, ensuring minimal influence on their capability to exhibit quantum interference.

Purification circuit

The purification circuits are implemented with optical fibers and involves two fiber beam-splitters (BSs) for each copy of the scheme, with the purified photons interfering in a final BS. We characterized the optical losses induced by the purification setup to be of 1 dB. These are mainly due to fiber connectors between the beam splitters. Because the overall circuit is based on cascaded HOM interferometers, which are phase-insensitive, no active phase stabilization is required.

In order to ensure that the photons have the same polarization throughout all the fiber BSs, the polarization has to be calibrated before each experiment. The calibration happens by sending laser light into the demultiplexer and collecting it from the output of the final HOM BS of the setup. The light is sent into a free space setup with a quarter and a half-waveplate followed by a PBS and a powermeter. The polarization is adjusted for each of the four inputs such that there is absolute extinction of the laser light on the powermeter.

Detection

The photons are finally directed to six superconducting-nanowire single-photon detectors (SNSPDs, average 85% system efficiency) to measure the output configurations. The electrical signal from the detectors is processed using a Swabbian time tagger unit, which records the time stamps from all of the 6 detectors for post-processing.

5.4.2 Data analysis

The data in our experiment has the format of time tag streams, which simply record the arrival time of single photons on a given detector over the duration of the experiment.

The most useful method to analyze such data is to use premade software that can create virtual channels and efficiently compute cross-correlation measurements.

Auto-correlation measurements for pulsed-excited single photon sources are a standard way of visualizing data in the field. Both in the case of $g^{(2)}(0)$ measurements and HOM visibility measurements, the desired value to be calculated can be extracted from the ratio of the area of the central peak with the average area of the side peaks. Thus in our experiment we would like to extract the final indistinguishability value by doing a similar cross-correlation measurement.

Most HOM experiments for deterministic single photon sources rely on data analysis where a correlation measurement between the tags of the two detectors is performed. To extract the HOM visibility, the area of the central peak is compared to the area of the same central peak but where the photons are made completely distinguishable, either by time delay or polarization rotation of one of the photons. In our experimental setup, which relies on consecutive fiber beam splitters, it was challenging to introduce a delay or a rotation in a reliable way, which is why we instead compare the central peak to the side peaks of the correlation, similar to a $g^{(2)}(0)$ measurement. Unlike a regular correlation measurement, there are two ambiguities that should be taken with caution:

1. The central peak is always well defined, but in the four-photon case the side peaks can be constructed in different ways. It is important to use the correct definition of a side peak.

2. The height of the central peak compared to the side peaks is not equal to 1 even if the photons are completely distinguishable. The visibility cannot be extracted by just considering the ratio of the central peak to the side peak.

Definition of a side peak

The correct way to construct a side peak is to create a virtual channel for each copy of the experiment and create an correlation measurement between the virtual channels in the end. Not using the virtual channels can lead to the mistake of creating side peaks where current photons are heralded by previous events, which would increase the size of the side peaks leading to more counts on the side peaks than what there should be.

Visibility estimation

We present an in-depth analysis of how to calculate the HOM visibility depending on the values of the central and side peaks in the appendix for this chapter. We will here present the final results of the analysis.

In order to calculate the raw HOM visibility V_{raw}, we block two of the input paths from the demultiplexer. We integrate for 30 s and observe that the single-photon count rate is 10 MHz at the final detectors. We then perform a correlation measurement

between the detector signals using a time tagger. This measurement gives time dependent values and we extract the central-peak counts C_{central} and the side-peak counts C_{side} by integrating on a 2 ns time window around the expected central values. We find V_{raw} by solving the system of equations:

$$\begin{aligned} 10^7 \cdot 30 \cdot t^2 \cdot 0.378\,(1 - V_{\text{raw}}) &= C_{\text{central}} \\ 10^7 \cdot 30 \cdot \Big[0.275 \cdot t(1-t) + t^2\,(0.0189(3 - V_{\text{raw}}) + 2.00)\Big]^2 &= C_{\text{side}} \end{aligned} \tag{5.4.1}$$

where t is the transmission probability of a photon through the whole setup. Some of the prefactors might appear unusual due to the reflectivity of two of the beam splitters in our setup, which we found to have a ratio of 45:55. This discrepancy leads to the resulting atypical values.

Next we estimate the HOM visibility of the heralded case, where all of the paths are unblocked. We integrate for 800 s while the singe-photon count rate is 10 MHz. We perform a two-detector correlation measurement on the virtual channels as described above, from which we extract the side peak and the central peak counts by integrating over a 2 ns time window. We estimate the purified HOM visibitility V_{pure} by solving the following system of equations:

$$800 \cdot 10^7 \cdot P_{\text{c,pure}} = C_{\text{central}}, \tag{5.4.2}$$

$$800 \cdot 10^7 \cdot P^2_{\text{1D,pure}} = C_{\text{side}}\,, \tag{5.4.3}$$

where $P_{\text{c,pure}}$ and $P_{\text{1D,pure}}$ are functions of t, V_{raw}, and V_{pure} defined in the appendix for this chapter. The system becomes a 4th degree polynomial in t which we solve numerically using the least squares method.

5.4.3 Fast-noise regime

This section is a reproduction with minor adjustments of the results section in [32].

To analyse the improvement in indistinguishability induced by the purification, we first assessed the raw HOM visibility by interfering only two demultiplexed photons (inputs 1 and 4 in Figure 5.4.2) by blocking inputs 2 and 3. Inputs 2 and 3 are then unblocked to implement the full circuit to test quantum interference between purified photons and extract their purified indistinguishability.

The purification protocol was tested in different experimental configurations of the QD, each with a different value of partial distinguishability between the emitted photons. The data from each configuration are shown in Figure 5.4.2. In the first configuration ("No etalon" label in Figure 5.4.2b), we test the protocol in a high-noise scenario by removing the etalon filter after the QD, which results in higher distinguishability due to the presence of incoherent spectral sidebands. This is indeed manifested in a measured low raw HOM visibility of $V_0 = 0.5829(1)$, as depicted in Figure 5.4.2(a)(lower). When the purification protocol is implemented, the visibility of HOM interference between the purified photons was increased to $V_f = 0.685(5)$ as depicted in Figure 5.4.2(a) (upper), marking a significant improvement of 10.2(5)%.

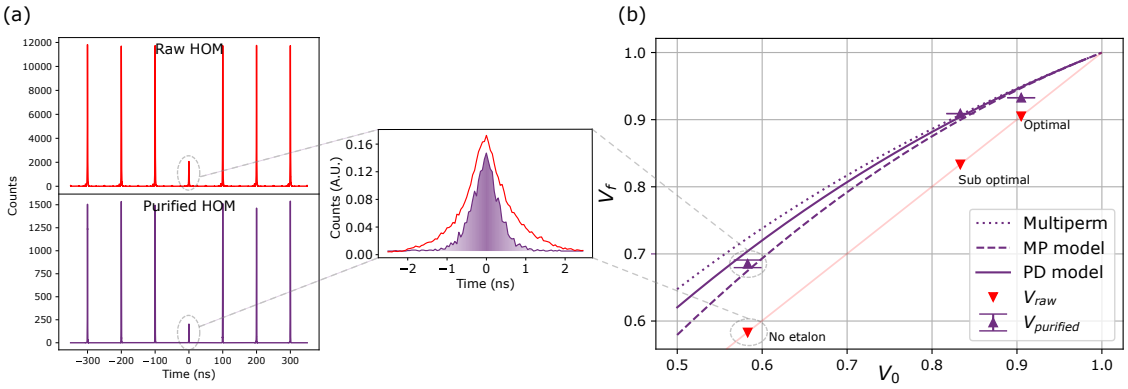

Figure 5.4.2: **Purification results for fast noise processes**. (a) Two-photon correlation measurement results for HOM experiments with raw (top) and purified (bottom) photons. (Inset) Normalised central peaks for both cases, showing an improved suppression for the purified (purple) case. (b) Obtained improvements in visibility for three configurations of the QD source with different noise levels. The curves show the theoretical estimates for different noise models, as described in the main text. The error bars (only shown when exceeding the size of the markers) are calculated via Monte-Carlo error propagation assuming Poissonian photon statistics. Figure and caption reproduced from [32].

The purple curve is both narrower and has a lower maximum than the red curve, suggesting that both the dynamics and the amplitude of the distinguishable components are altered. The width of the peak nonetheless only changes due to the lower heralding probability of photons far away from the center position, as the effect can also be seen on the sidepeaks. It can thus not be concluded that the purified photons have different properties than the raw ones, except for a lower distinguishable component.

In a second QD configuration ("Optimal" label in Figure 5.4.2b), the etalon was added to test the protocol in a low-noise environment where most phonon-induced noise is filtered out. The initial raw HOM visibility was measured to be $V_0 = 0.9050(1)$, which is then improved to $V_f = 0.9327(1)$ using the purified photons. As discussed in the Supplementary Information, we estimate that in this case the remaining noise contributions limiting the visibility are dominated by spurious multi-photon terms arising by the finite $g^{(2)}(0)$ of the QD, while contributions due to partial distinguishability is mostly removed via the purification.

We tested one additional scenario ("Sub optimal" label in Figure 5.4.2b) where we keep the etalon but intentionally detune the voltage applied to the QD from its optimal value. Applying a voltage that is closer to the edge of the charge plateau increases the probability of co-tunelling of carriers to the contacts. This experimental condition induced a slight reduction in raw HOM visibility to $V_0 = 0.8332(1)$, which is then enhanced to visibility of $V_f = 0.9090(5)$ through purification.

The data histograms which are the base for the Sub-optimal and Optimal config-

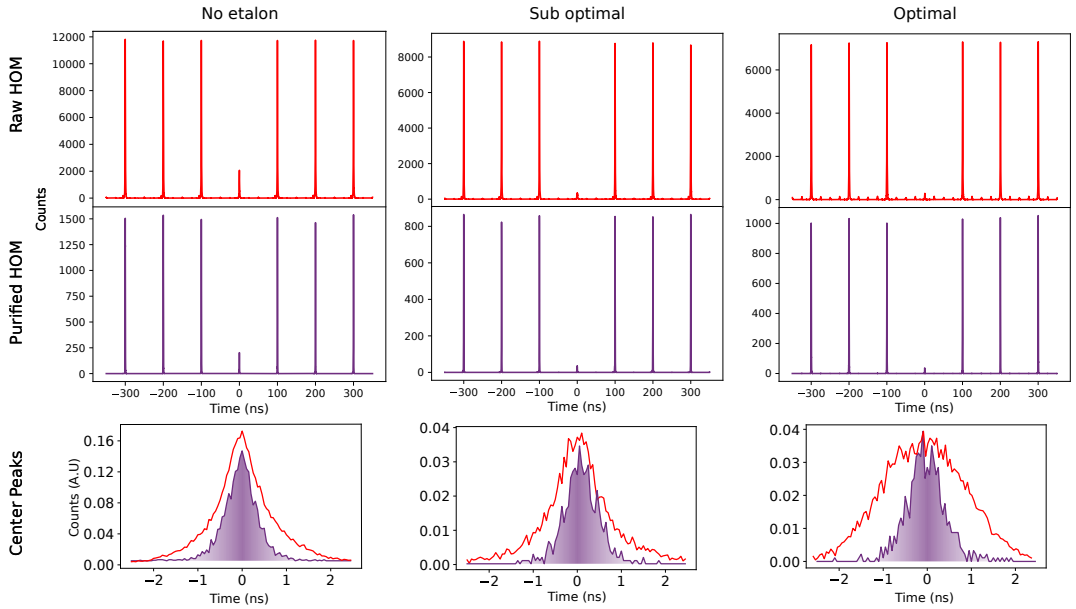

Figure 5.4.3: Data histograms for the Optimal and Sub-optimal configuration results. Figure reproduced from the supplementary material of [32].

uration results are shown in Figure 5.4.3.

In Figure 5.4.2 we also plot the theoretical estimations of the indistinguishability for the purified photons as a function of the raw visibilities, and used in addition three different models for predicting the partial distinguishability of the photons as introduced in Section 5.2. The theoretical curves give slightly different expected improvements but agreement with the measurements is exhibited. Even though more datapoints are needed to draw a significant conclusion about how good the data agrees with the theory, it may be suggested that the last datapoint is below the expected value due to the $g^2(0)$ value preventing us from extracting the intrinsic indistinguishability of our purified photons.

5.4.4 Slow-noise regime results

After demonstrating successful purification for the case of a fast physical process, in particular phonon-induced dephasing, we test the purification protocol in the presence of slow errors as well. In this case, we deliberately altered the polarization of one input photon per purifier, as illustrated in Fig. 5.4.4a, and again evaluated the HOM visibility before and after purification. The results, shown in Fig. 5.4.4b, compare our experimental data (in purple) with a simulation illustrating the application of the purification protocol to photons with different polarizations. The polarization of the photons after going through multiple fiber BSs is transformed in a randomized manner by temperature drift and bending of the fibers, and thus setting for a specific transformation is not attempted. The upper bound comes when the photons' polar-

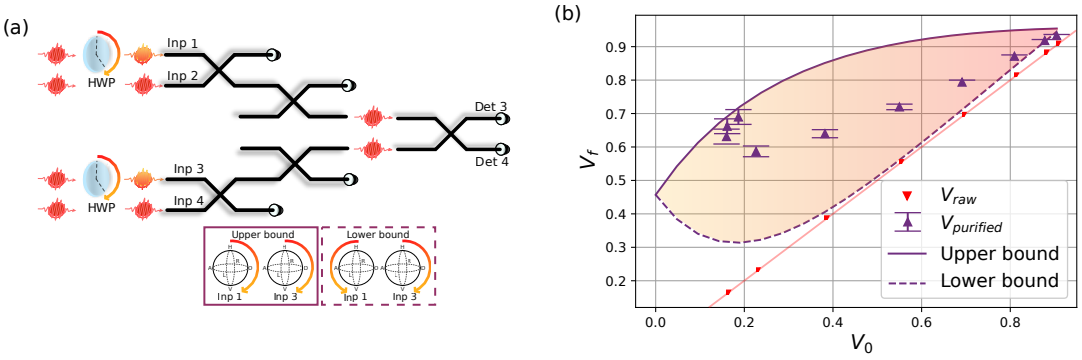

Figure 5.4.4: (a) Purification in the presence of polarization-induced distinguishability contributions implemented by rotating the HWP of inputs 1 and 3. (b) Experimental purified indistinguishabilities (purple markers) for various raw HOM visibilities (red markers). The theoretical upper and lower bounds are the expected improved values in the cases where the polizations of inputs 1 and 3 are rotated in the same or opposite directions, respectively. Figure and caption reproduced from [32].

ization is rotated in the same direction of the Bloch sphere, while the lower bound comes when they are rotated in opposite directions. Both cases are illustrated in the upper side of Fig. 5.4.4b, and the associated curves are plotted together with the measured raw and purified HOM visibilities. Representative histograms used to generate three of the data-points from the figure are shown in Figure 5.4.5. The observed data again show significant improvements in the indistinguishability and is compatible with the theoretical bounds described above, demonstrating the realization of a successful purification protocol for both slow and fast noise contributions.

5.5 Conclusion

In this chapter we have demonstrated a new type of purification process in quantum optical systems: the purification of partially distinguishable photons through quantum interference. We began by reviewing the theoretical background behind the protocol, combining numerical simulations based on multi-permanent calculations of the scattering matrix with a tailored analytical model that accounts for noise processes specific to quantum dot sources. We find that the models all predict improvement in indistinguishability through the protocol, but yield slightly different predictions due to them being based on different assumptions. We employ these models to investigate how certain error sources would affect the efficacy of the protocol and find that apart from affecting the final count-rate, our protocol is robust against typical error sources like losses, optical imperfections and multi-photon components. We also investigate what happens when the protocol is applied to photons from different sources, and find that our protocol should still be able to improve the output indistinguishability in that

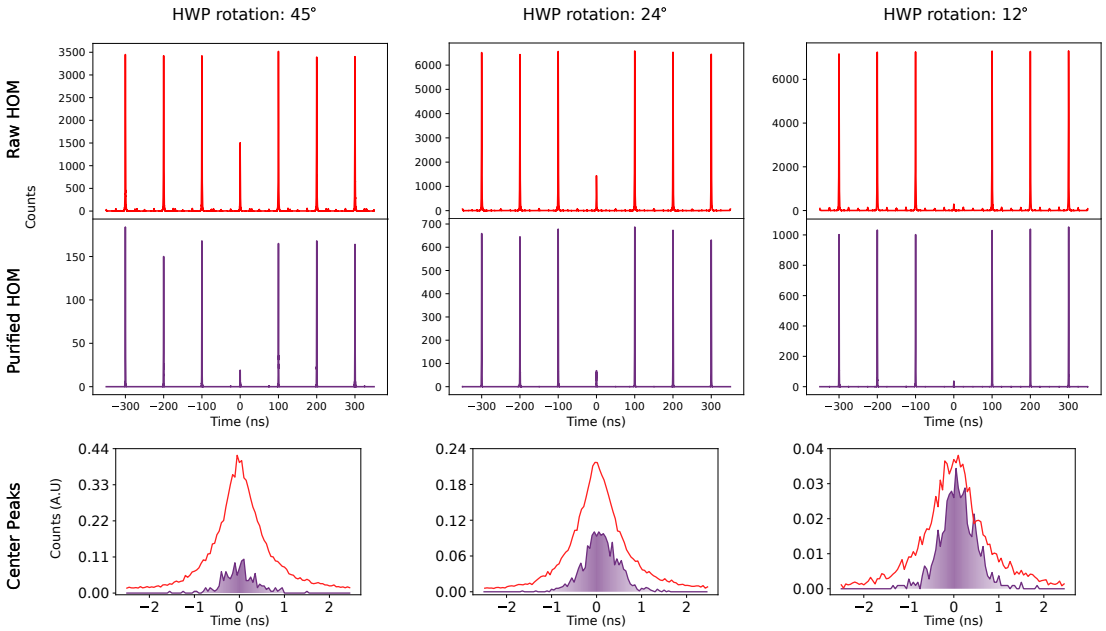

Figure 5.4.5: Representative histograms used to generate the Figure 5.4.4 (3rd, 5th and 9th datapoints). Figure reproduced from the supplementary material of [32].

case, specially for correcting polarization-induced distinguishability.

Experimentally, we verified the protocol through two complementary approaches. In the temporal-domain approach, we aimed to implement purification using a single beam splitter to achieve interference at multiple points in time. However, limitations in the available components prevented successful execution. We identified the key shortcomings, performed a detailed analysis of their impact, and outlined practical recommendations for future implementations.

In contrast, the spatial-domain approach, employing a time-to-space demultiplexer, successfully demonstrated purification with significant improvements in photon indistinguishability. Using a simple purification circuit with n=2 input photons, we showed that the protocol effectively mitigates both fast and slow noise processes, outperforming existing noise mitigation techniques such as environment monitoring and time-resolved measurements, which are limited to addressing slow noise sources like spectral diffusion. These results highlight the versatility of the purification protocol and its potential for integration into various quantum photonic platforms.

This experiments establish purification as a powerful tool for overcoming the challenges posed by partial distinguishability, paving the way for its adoption in scalable quantum systems. Future efforts will focus on extending the protocol to larger-scale implementations and exploring its integration with different photon sources and quantum photonic architectures.

Chapter 6

Photonic Quantum Simulation

In this chapter we describe our work with silicon-on-insulator photonic integrated circuits and their use within analogue quantum simulations of interacting-spin systems.

Statement of work

The work presented in this chapter was done in close collaboration with Patrik Isene Sund and Alif Laila Muthali, under the supervision of Stefano Paesani and Yunhong Ding. Alif Laila Muthali designed, fabricated and characterized the silicon chip, as well as helping with the installation and running the experiment. Patrik wrote and optimized the program used to perform the metropolis algorithm, as well as running and refining the experiment. The author of this thesis participated mainly in the installation of the experimental setup, building the non-PIC components: demultiplexer, frequency conversion setup and single photon source setup. Stefano Paesani suggested the idea of using this setup for simulation of interacting spins as well as providing essential support in how to run the experiment and the code for the simulations.

6.1 Introduction

Through this thesis we have explored different primitives that could be used for building photonic quantum computers. These had the aim to be parts of a generalized quantum computer with no specific application in mind. In doing so we delved into the physics of quantum emitters and photonic integrated circuits (PICs). In this chapter we explore an immediate application of these hardware components within quantum simulation, bypassing the need for a quantum computer.

Analog quantum simulation is a field of quantum information science which employs mappings of Hamiltonians in known quantum systems to Hamiltonians that are hard to compute with a classical computer. If a physical system governed by a given Hamiltonian can be experimentally realized and is controllable, various measurable quantities related to that Hamiltonian can be extracted [124, 125]. It has also been shown recently that under certain conditions it is possible to map classical systems into

analog quantum simulators[126], resulting in quantum simulation of classical systems, where classical simulations of such systems would be less efficient.

A classical model that has numerous parallels in various physical systems as well as in models within information science is that of a system of interacting spins [127]. In Figure 6.1.1(a) we show 1D and 2D arrays of spin configurations in crystal formations. The spins interact with each other through their dipole moment, which leads to them having a preferred configuration that corresponds to the system's ground state. This configuration may then be altered upon the application of an external magnetic field or contact with a thermal bath. There are different models used to calculate the energy of an array of interacting spins. In Figure 6.1.1(b) we show the 2-spin and the 4-spin models, which are p-spin models where p refers to the order of the interaction considered when calculating the energy.

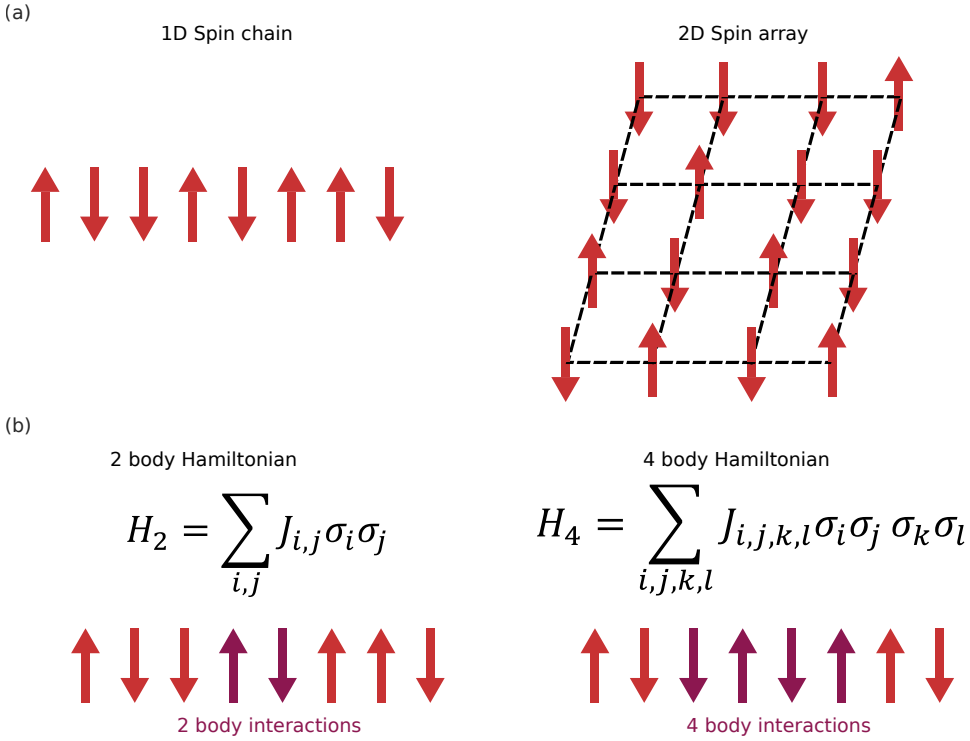

Figure 6.1.1: (a) Illustration of a 1D spin chain and a 2D spin array, both of which are examples of ordered interacting-spin systems. (b) Illustration of the 2 and 4 body Hamiltonians used to describe the dynamics of interacting-spin systems.

The physics of p-spin models are computationally complex given that their Hamiltonian is the sum over a p-dimensional tensor. Properties like the ground state configuration or the phase transition dynamics are generally hard to simulate. Nonetheless being able to solve for some of these properties can have many immediate applications in classical optimization problems like solving the Hopfield model [128], which is used to study memory problems in neural networks [129].

The photonics industry is a growing sector that has allowed multiple technological advancements for telecommunications and ultra-fast information processing [76]. These advancements can be readily applied to quantum technologies, as single photons can propagate through the exact same channels as classical light. In chapter 4 we presented a proof of principle experiment integrating single-photons and photonic integrated circuits (PICs), and discussed how the simulation of these cannot be performed efficiently on a classical computer. Similarly, large scale PICs interfaced with single photons offer a route for analog quantum simulation of physical systems that are hard to simulate on classical computers.

In this chapter we will explain how many of the dynamics of a system of interacting spins can be simulated using photons interfering in linear-optic circuits and discuss how this can yield an advantage over performing the computations on a classical computer. We will then proceed to describe a proof of principle experiment employing photonic integrated circuits to simulate a simple interacting-spin system. At last we will describe the results of such an experiment and discuss the limitations imposed by our system.

6.2 Theory

The Hamiltonian of an interacting spin system including only 2-body interactions is given by

$$H_{\text{2body}} = -\frac{1}{2}\sum_{j,k}^{N} J_{j,k}\sigma_j\sigma_k\,, \tag{6.2.1}$$

where σ_j is a z Pauli operator acting on the j-th spin or simply a number $\sigma_j \epsilon [1, -1]$ in the classical case. This is the dominant term in the interaction, but a more accurate Hamiltonian should include the contributions from the 4-body interactions

$$H_{\text{4body}} = -\frac{1}{2}\sum_{j,k,l,m}^{N} J_{j,k,l,m}\sigma_j\sigma_k\sigma_l\sigma_m\,. \tag{6.2.2}$$

It should be noted that the two-body interaction term is included in this hamiltonian for the terms where $j = l$ and $k = m$. We will now describe how this Hamiltonian can be mapped into a linear-optic circuit and its permanent. We recall from eq. 2.2.13 that the amplitude of n photons scattering on an interferometer can be calculated as

$$\begin{aligned}\langle k_1, k_2, ..., k_n|\, U\, |c_1, c_2, ..., c_N\rangle = \\ \frac{\text{Perm}(B)}{\sqrt{\prod_i k_i!}\sqrt{\prod_j c_j!}}\,,\end{aligned} \tag{6.2.3}$$

where k_i denotes the output modes and c_i the input modes. The matrix B is the submatrix resulting from selecting rows and columns according to output and input modes as shown in eq. 2.2.14.

We consider scattering of a generalized input state

$$|\psi\rangle = \sum_{\vec{c}\in C_M} a_c \, |\vec{c}\rangle \ , \tag{6.2.4}$$

where C_M is the set of n photons in M modes. After propagating through a screen of

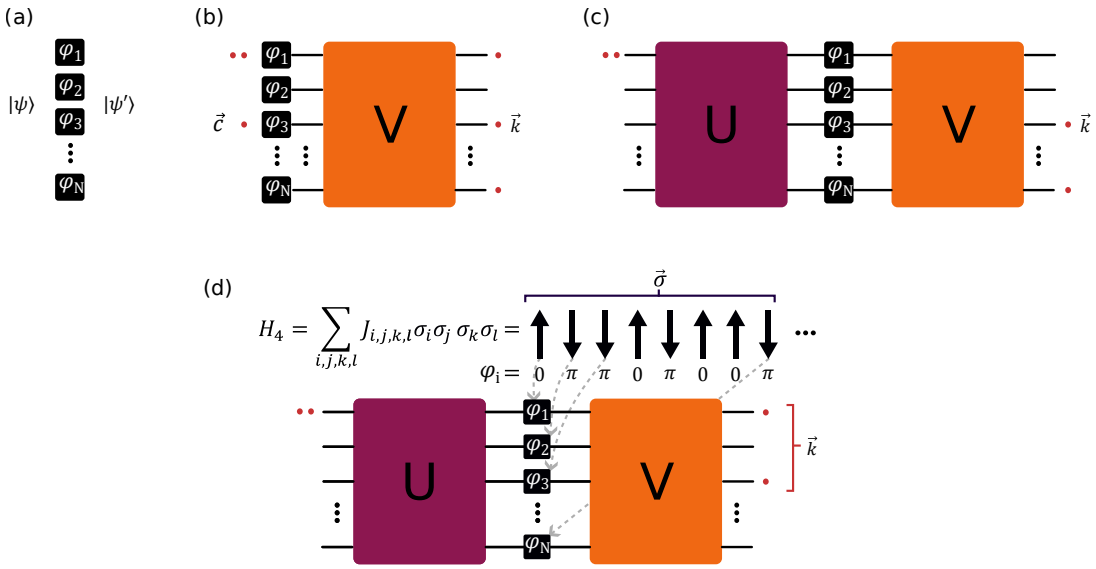

Figure 6.2.1: (a) A photonic superposition state is altered by a screen of phase shifters. (b) Photons propagating through interferometer V. (c) Full circuit with U and V necessary for photonic quantum simulation of an interacting spin system. (d) Mapping between an array of interacting spins and a photonic interferomenter.

phase shifters as shown in Figure 6.2.1(a), the state it will transform into

$$\begin{aligned} |\psi'\rangle &= \sum_{\vec{c}\in C_M} a'_c \, |\vec{c}\rangle \ , \\ a'_c &= e^{i\sum_{j=1}^{n}\phi_j} a_c \, , \end{aligned} \tag{6.2.5}$$

After propagating through an interferometer described by a unitary matrix V as shown in Figure 6.2.1(b), the scattering amplitudes become

$$\left\langle \vec{k} \right| S \, |\psi'\rangle = \sum_{\vec{c}\in C_M} \frac{a'_c}{\sqrt{\prod_i k_i!}\sqrt{\prod_j c_j!}} \mathrm{Perm}(S_{k|c}) \, . \tag{6.2.6}$$

In order to simulate spins we now restrict the possible phases that can be applied to two possible values $\phi_j = \{0, \pi\}$. These values can be anything as long as they are separated by π, but they can always be simplified to be $\{0, \pi\}$ by adding the correct

overall phase. Any spin will then be mapped to a phase of $\sigma = \pm 1$. The amplitudes can be written as

$$\left\langle \vec{k} \right| S \left| \psi' \right\rangle = \sum_{\vec{c} \in C_M} a_c \frac{\sigma_{c1}\sigma_{c2}...\sigma_{cn}}{\sqrt{\prod_i k_i!}\sqrt{\prod_j c_j!}} \mathrm{Perm}(S_{k|c}) \,. \tag{6.2.7}$$

the probability of getting an output state $\vec{k}$ given a spin configuration $\vec{\sigma}$ is then

$$\begin{aligned} P(\vec{k}|\vec{\sigma}) &= |\left\langle \vec{k} \right| S \left| \psi' \right\rangle|^2 = \left\langle \vec{k} \right| S \left| \psi' \right\rangle \left\langle \vec{k} \right| S \left| \psi' \right\rangle^* \\ &= \sum_{\vec{x},\vec{y} \in C_M} \frac{a_x a_y^*}{\prod_i k_i! \sqrt{\prod_i x_i!}\sqrt{\prod_j y_j!}} \mathrm{Perm}(S_{k|x})\mathrm{Perm}(S_{k|y})^* \prod_i \sigma_{xi} \prod_i \sigma_{yi} \\ &= \sum_{\vec{x},\vec{y} \in C_M} J_{\vec{k}}(x_1, ..., x_n, y_1, ..., y_n) \prod_i \sigma_{xi} \prod_i \sigma_{yi} \,. \end{aligned} \tag{6.2.8}$$

We have thus arrived at an equation where the probability of scattering has a very similar form to the Hamiltonian of an interacting spin system. We note specially for the case of scattering of two photons that the equation becomes

$$P([k_1, k_2]|\vec{\sigma}) = \sum_{\vec{x},\vec{y} \in C_M} J_{[k_1,k_2]}(x_1, x_2, y_1, y_2)\sigma_{x1}\sigma_{x2}\sigma_{y1}\sigma_{y2} = -H_{4body} \,. \tag{6.2.9}$$

This equation tells us that a two-photon state can simulate the dynamics of an interacting spin Hamiltonian with up to 4 body interactions.

Any input state $|\psi\rangle$ can be generated from a simple two-photon input state by adding a universal interferometer with a unitary matrix U as illustrated in Figure 6.2.1(c). A convenient choice for the U matrix is that of a discrete-Fourier transform (DFT), as it creates a uniform superposition state to propagate through the phase shifters, maximizing the complexity of the simulation. We describe DFT matrices in Chapter 4.

We illustrate in Figure 6.2.1(d), how an array of interacting spins is mapped to the type of photonic interferometer that we have discussed, where the state of the individual spins is equivalent to the phase executed by the individual phase shifters in the center.

An accurate simulation requires that the input state and the V matrix are tuned to map into the same components as the J matrix of the spin system Hamiltonian, but doing so would require the permanents to be calculated, missing the computational advantage. It is though still possible to get some useful information through this method without calculating permanents, by computing the ground state and exploring its dynamics.

6.2.1 Metropolis algorithm

The ground state can be found by making use of the fact that the probability of a scattering event is proportional with a negative sign to the energy of its equivalent array

of interacting spins. Finding the set of phases that maximizes the success probability (or the count rate in an experimental setup) is thus equivalent to finding the spin configuration that minimizes the Hamiltonian, which is the definition of the ground state.

We find the ground state configuration by applying a Monte Carlo based algorithm known as the Metropolis algorithm. The algorithm initiates with a random phase (spin) configuration. At each step, one of the phase shifters is modified by π, effectively flipping a spin, and the resulting change in the success probability is evaluated to determine whether the new configuration is accepted. This is illustrated in Figure 6.2.2(a). If the phase flip does not increase the success probability the old configuration remains unchanged. If the phase flip increases the success probability the phase configuration is updated. If the process is repeated many times, the probability will increase until the optimal configuration has been achieved. We simulate what hap-

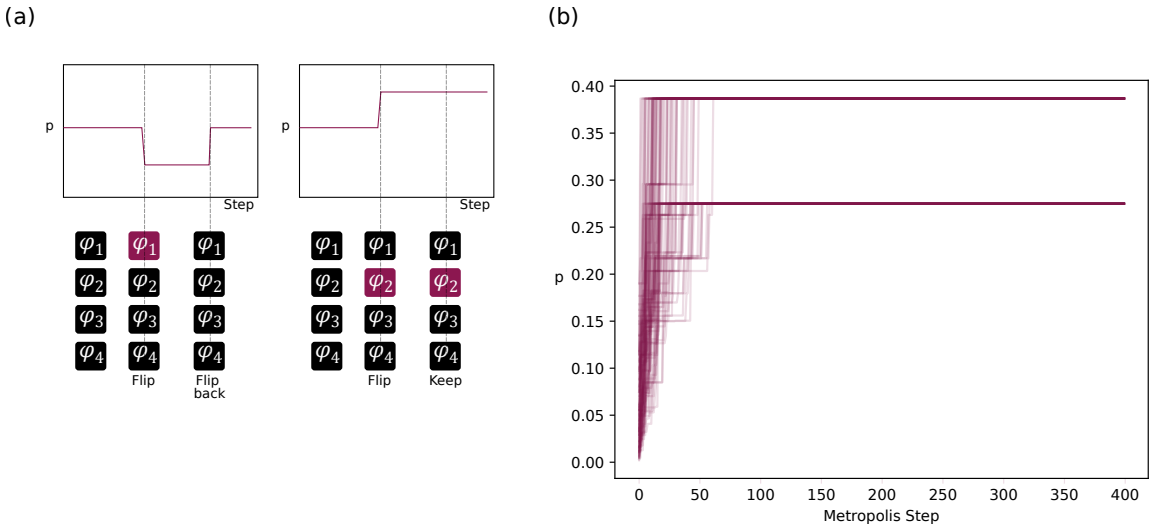

Figure 6.2.2: (a) Principle behind the metropolis algorithm. A phaseflip leads to a change in the probability of detecting a certain output combination. If the probability is greater as before the flip, the new phase is adopted into the phase configuration. (b) Example simulation of sampling through the metropolis algorithm. We simulate 2 photons propagating through a 10 mode interferometer. We observe a local maximum and a global maximum in the probability. (Simulation done by Patrik I. Sund)

pens when applying the metropolis algorithm for an experiment with n=2 and m=8 in Figure 6.2.2(b). In the simulation, U is set to be a DFT, V is set to be a Haar Random matrix and k is an output chosen randomly. Running the algorithm many times shows that most configurations end up in one of two possible energy states. The one with the higher probability corresponds to the ground state configuration, while the lower one is a local mininum corresponding to a different state. Running the metropolis algorithm many times results in different steady state solutions with different energies. A way to visualize how many spin states there are and how close they are to each other is to

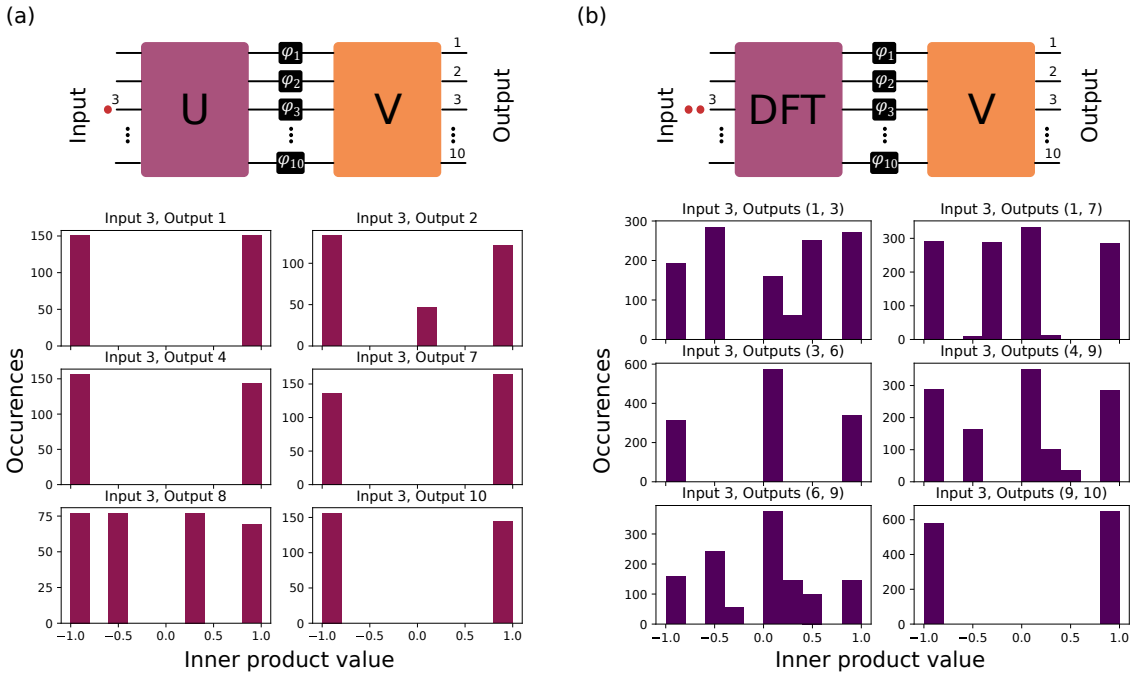

Figure 6.2.3: (a)Inner product simulations for a one photon experiment. The simulation consists on running the metropolis algorithm many times and collecting the final spin states (phase configurations). The spin states are represented as vectors with values ± 1 and all of their inner products with respect to each other are computed. Changing the output configuration effectively changes the Hamiltonian of the spin system that is being simulated. (b) Inner product simulations for a two photon experiment. We observe that ferromagnetic behavior is much more rare than for the case with one photon.

take the inner product between them. We define the inner-product between two spin states $\vec{\sigma}_1$ and $\vec{\sigma}_2$

$$\frac{1}{N}\sum_{i=1}^{N}\sigma_{1,i}\cdot\sigma_{2,i}, \tag{6.2.10}$$

where N is the number of spins. As the individual spins take values of either -1 or 1, the inner product also takes values between -1 or 1, where the case of -1 corresponds to opposite values for every spin in the two states, and 1 corresponds to every spin being parallel.

After taking all the inner products between all the resulting spin states the different values can be plotted on a histogram. If there is a clear global maximum, all of the states should have inner product with a value of 1. But in this situation it is possible for the same maximum to acquire an overall global phase of -1, which would result in the exact opposite spin-state, making the inner product -1. A case with only one possible

energy configuration will thus exhibit only two possible spin states which configurations are each other's opposites, a phenomenon similar to ferromagnetic behavior.

In Figure 6.2.3(a) we show different results for a simulation where the metropolis algorithm has been run many times in a situation where a single photon scatters on the interferometer type shown in Figure 6.2.1(c), corresponding to the simulation of a 2-body Hamiltonian. It can be observed that most configurations achieve only two possible inner products, which indicate that ferromagnetic behaviour is highly likely in a 2-spin model. In part (b) we show the same situation with scattering of two photons, i.e. simulating a 4-body Hamiltonian. Here it can be observed that most configurations do not lead to ferromagnetic behaviour, indicating the presence of many local minima for energy configurations.

The metropolis algorithm is not only useful to find ground state configurations of spin systems, it can also be used to simulate what happens when there is a non-zero temperature involved. To include temperature into the algorithm, the rejection condition is changed, such that if a spin flip results in lower counts it will still have a chance of being accepted. The condition for accepting a spin flip that leads to lower probability is

$$r < \exp(\Delta P \beta), , \tag{6.2.11}$$

where r is a randomly generated number between 0 and 1, ΔP is the change in probability after the flip which must have a negative sign in order for the condition to be evaluated, and $\beta = 1/T$ with T being the temperature. This way for T=0 the model is unchanged but for $T \to \infty$ every spin flip will be accepted, making the end result completely random. In an experimental setup we do not measure a probability P but rather a count rate or a power, which is why the relevant temperature ranges can vary significantly between different experiments.

A simulation of the metropolis algorithm for different temperatures can be seen in Figure 6.2.4(a). We simulate a two-photon experiment where the configuration of the interferometer leads to only one possible energy state at zero-temperature. It can be observed that the ferromagnetic behaviour disappears and becomes a Gaussian distribution around zero for high temperatures. A more detailed 2D map is plotted in Figure 6.2.4(b), where the behaviour becomes clear. For a 2-photon experiment it is more common to have non-ferromagnetic configurations at zero temperature, so we also show the results of a simulation of such a configuration in Figure 6.2.4(c). This system exhibit phase transitions going from 3 peaks to two peaks and then to a Gaussian distribution, showing that the dynamics of interacting-spin systems are nontrivial and worth exploring.

Classically the ground state dynamics can be calculated in polynomial time with respect to the number of modes M. Running the analogous quantum simulation on a photonic chip also scales polynomially in time with M, but it is a lower order polynomial. Quantum advantage can thus be expected when M is large. More details will be given in an upcoming manuscript co-authored by Stefano Paesani.

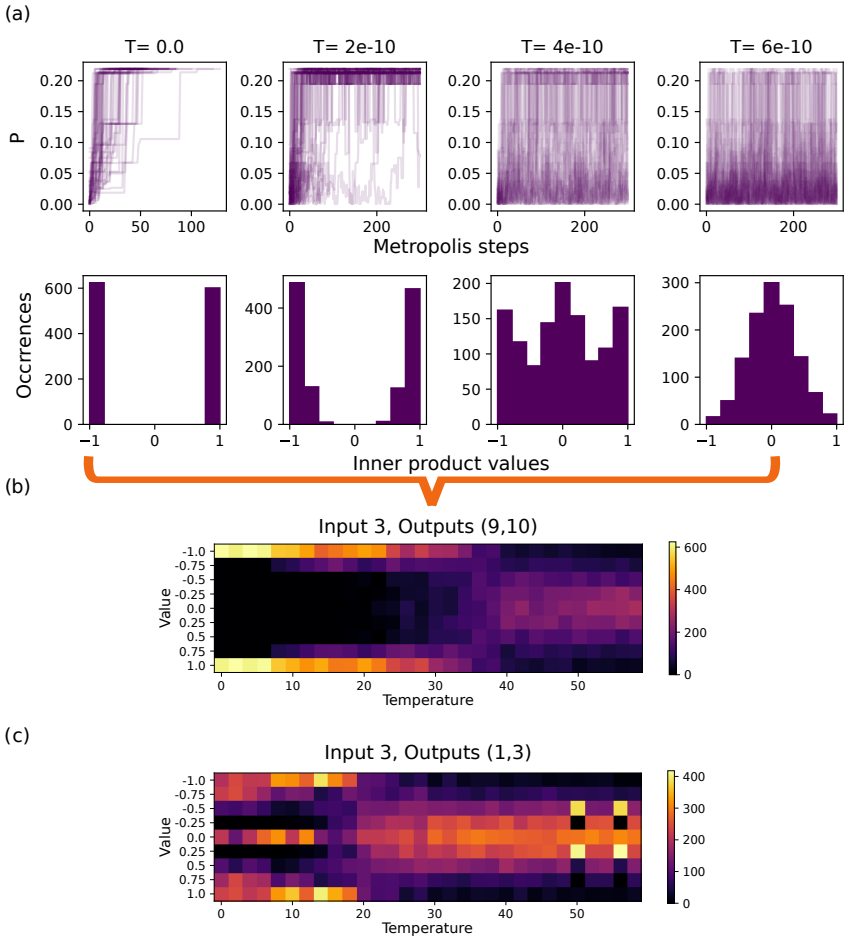

Figure 6.2.4: (a) Temperature simulations. (up) Metropolis algorithm simulations for different temperatures. (down) Corresponding inner product histograms for the simulations (b) 2D histogram of the inner products of the same system including more temperatures. (c) 2D histogram of the inner products of a different system, one that does not exhibit ferromagnetic behaviour at zero temperature. Phase transitions from a 3 peak state to a ferromagnetic state to a Gaussian state can be observed.

6.3 Experimental setup

This experimental project is a collaboration with the technical university of Denmark (DTU), where the aim was to combine their expertise in fabrication of photonic integrated circuits [130] with our single photon sources. For this project a large silicon-on-insulator (SOI) chip was fabricated. The chip exhibits a universal 10x10 photonic interferometer in the Clemens architecture [131]. Given that the transparency range of Si is in the telecom range, the photons emitted from our quantum dots in the range of 930 nm is not suitable. To bridge this gap we use a frequency conversion setup capable of converting single photons from our quantum dots to telecom wavelength [132], which enables photon scattering experiments in Si PICs. An overview of the

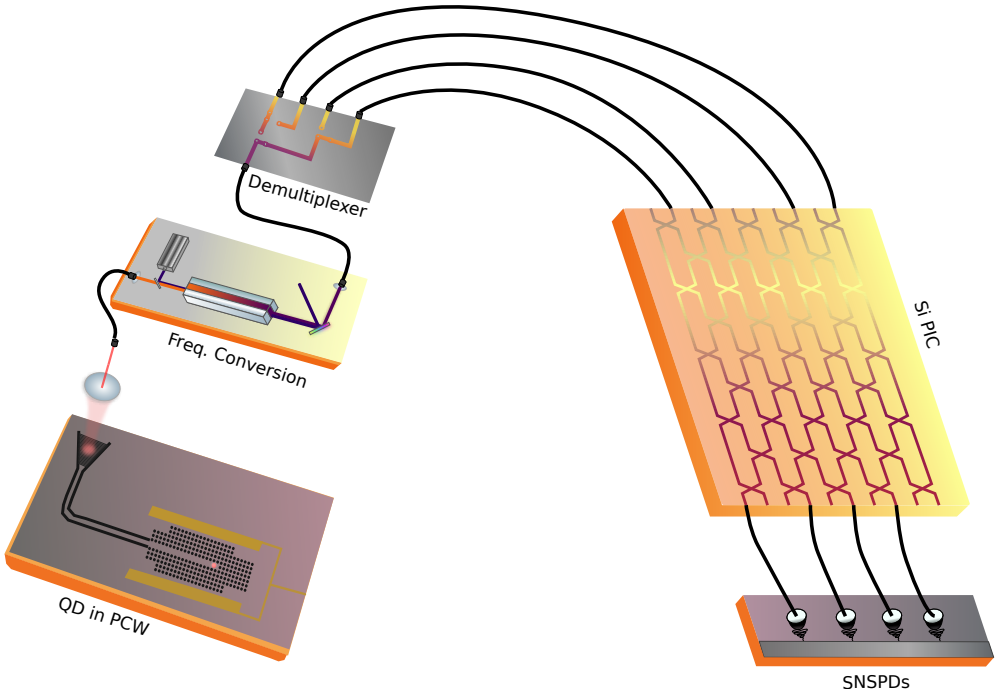

Figure 6.3.1: Proposed experimental setup for faithful interacting spin system simulations. A quantum dot (QD) in a photonic crystal waveguide (PCW) generates single photons that are converted to telecom C-band wavelength through a free space frequency conversion setup. The photons are then demultiplexed using a two/four photon fiber-based demultiplexer. The simulation happens at a Silicon photonic integrated circuit (PIC) which contains a universal 10 mode interferometer. We finally measure the probability of a ceratin output by counting detections on superconducting-nanowire single-photon detectors.

experimental setup that is to be used is depicted in Figure 6.3.1. A QD SPS is resonantly excited with a pulsed laser with a repetition rate of 80 MHz. The photons are transported through a fiber to a free space frequency conversion setup, where through

difference frequency generation the frequency of the photons becomes 1550 nm. The converted photons are then demultiplexed using a fiber based demultiplexer of either 2 or 4 modes, depending on the experiment to be realized. The demultiplexed photons are coupled into the Si PIC through a fiber array and the output is collected on another fiber array. Finally the photons are detected using telecom SNSPDs.

The SPS sample used for this project is very similar to the one described in Chapter 4. Unfortunately the wire bonding on the SPS structures of the chip was faulty and these structures could not be used, so we use multiple-port design structures, sub-optimal for single-photon generation. We performed spectroscopy on different structures to find the best QD candidate. We chose a QD emitting at a wavelength of 932 nm. The attained count rate at the detectors after alignment optimization is about 2 million counts. This suggests a source efficiency in the range of 2%. The low efficiency is attributed to using structures unsuitable for single-photon generation, and to low efficiency SEGs which came due to a fabrication error during the fabrication of this sample.

The frequency conversion setup is described in [132] and further in [133]. The DFG happens on a periodically poled lithium niobate (PPLN) waveguide where a high power laser at a wavelength of 2.4 μm is coupled into the waveguide together with the single photons. The free space optical setup is illustrated in Figure 6.3.2(a). The phase matching condition is met by using a poling period of 25.7 μm and tuning the temperature of the waveguides to be around 43° Celcius. This poling period corresponds to a different waveguide than the one used in [132], which has not been studied nor optimized as much as the previous one. The length of the waveguides is 48 mm and should allow for conversion of single photons with close to unity efficiency if enough laser power is coupled into them. We achieved an internal efficiency of maximally about 80% and an end to end efficiency of about 30%. The low internal efficiency can be attributed to imperfect coupling of the 932 nm beam into the waveguides, where a possible explanation could be a spot of dust preventing perfect coupling into the fundamental mode. This can partly explain the low end to end efficiency, but another possible explanation could be an imperfect fiber coupling at the end which again can be attributed to the output mode of the frequency conversion not being only a Gaussian mode.

The fiber-based demultiplexer that we use is illustrated in Figure 6.3.2(b). It consists of a small electro-optic modulator (EOM) directly integrated with a PBS, which splits the path of the outgoing photons depending on the voltage applied to it. This is an off-resonant EOM which receives a strong voltage signal from a circuit board that amplifies the signal received from a signal generator. We tested the performance of the EOM using a classical laser and varying parameters like the frequency and amplitude of the triggering signal. We found optimal shape and visibility of the output light signal when driving it with a frequency of 1.25 MHz and a peak-to-peak voltage of 5V. With this frequency, photons are divided into photon trains with a length of 64 photons.

The second part of the demultiplexer consists of a delay line with a fiber long

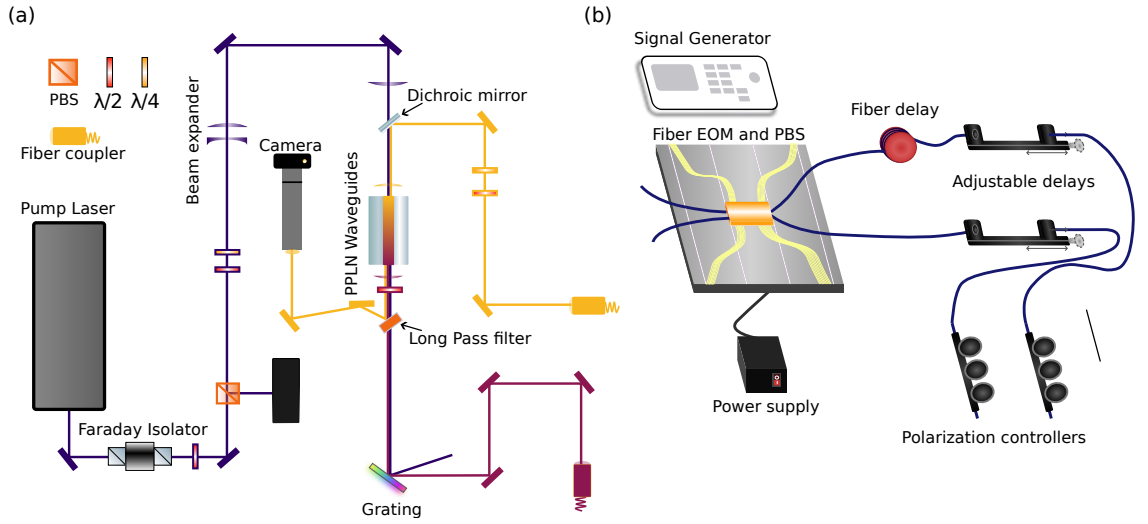

Figure 6.3.2: (a) Frequency conversion setup. A strong pump laser at 2400 nm is combined with single photons at 940 nm on periodically-poled lithium niobate (PPLN) waveguides in order for the single photons to be converted to 1550 nm.(b) Fiber based demultiplexer. It consists of an active component in the form of a fiber-based electro-optic modulator (EOM) followed by a PBS in order to send a train of photons into a fiber delay and the subsequent train into a non-delayed path.

enough to delay the photons by the amount of time required by the frequency of the EOM. For our case this corresponds to a 70m long fiber. The fine adjustment of the delay length is performed by adding tunable free-space optical delay lines to each output of the demultiplexer. The tuning is performed by optimizing the interference visibility of a classical pulsed laser going through the demultiplexer. We used the same laser applied for excitation of the QD, converting its frequency first.

6.3.1 Si PIC

The single photons are coupled into the Si chip by using a 16 channel fiber array. High efficiency grating couplers are fabricated into the chip, which are optimized for coupling at an angle of 75 degrees for 1550 nm light. The coupling is also polarization dependent, as the waveguides have a significantly higher transparency for the TE than the TM mode. For this purpose it is necessary to add a polarization controller before the chip coupling and optimize the input polarization before any run of the experiment. At the output an equal fiber array is placed in order to collect the light, as shown in Figure 6.3.3. The fiber arrays have to be as close as possible to the chip without touching, as touching will damange the fiber array. The angled coupling makes it slightly harder to align the fiber arrays into the optimal position, making the need for in-plane mirrors unavoidable. We characterized the insertion loss through the chip

by sending light into any of the inputs and collecting light simultaneously at all of the outputs. Comparing the input power to the sum of the output powers we got that for most inputs the insertion loss was of about 6 db. The unitary transformation

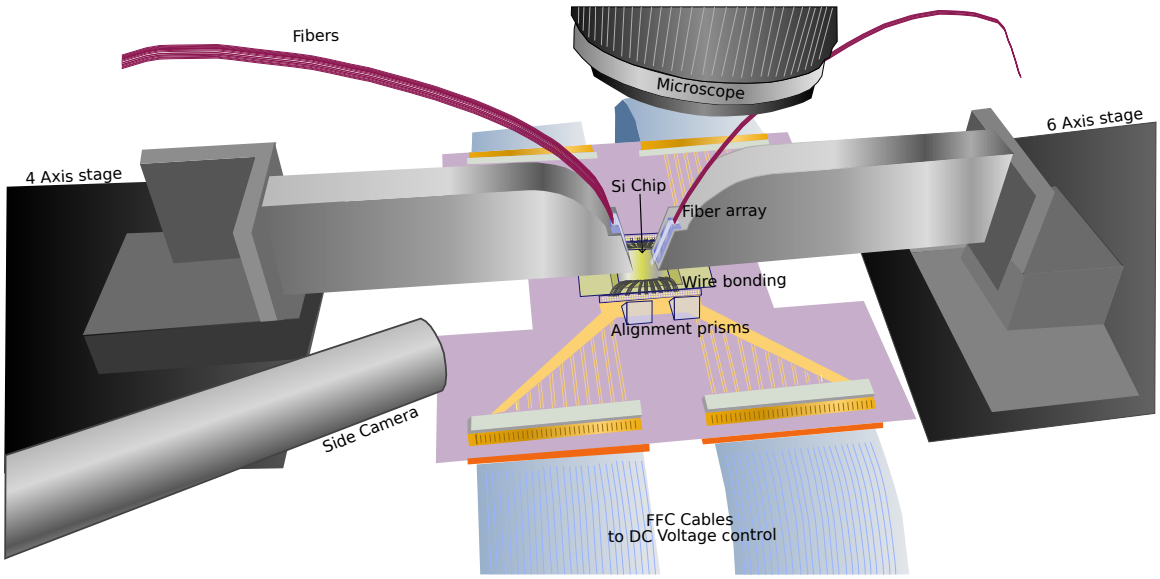

Figure 6.3.3: Illustration of the experimental setup to couple light and electrical contacts into the chip. Light couples through angled fiber arrays in and out of the chip. To optimize the coupling it is essential that the fiber arrays are as close as possible to the chip without actually touching it. Fot his purpose we use both a side camera and a a microscope with alignment prisms to monitor the position of the fiber array. The electrical contacts in the chip are wire-bonded to metal lines on the PCB in order to connect to the computer controlling the experiment.

produced by the chip is reprogrammable as it contains phase shifters that work through the thermo-optic effect, similarly to those in the SiN PIC in Chapter 4. Howerver, the electrical control is slightly different as the contacts in this chip are wirebonded, eliminating the need for manual coupling of an electrical probe. This is an advantage for a chip with a single structure but a high ammount of phase shifters, as it avoids the danger of scratching the surface of the chip with an electrical probe. The other end of the bonded wires leads to a printed circuit board (PCB), which connects to FFC cables to interface with the voltage control, which is very similar to that we used for the SiN chip of Chapter 4, illustrated in Figure 4.2.8. We present a 3D visualization of the interferometer on the chip in Figure 6.3.4, where we make clear which sections belong to which part of the photonic circuit. The left inset of the figure shows an SEM image of one the chip's high efficiency photonic-crystal grating couplers, where the taper-like structure of the holes can be appreciated. The right inset shows a zoom in of one of the central MZI structures, and a further zoom in shows an SEM image of one of the directional couplers that make up this MZI. It can be observed that the

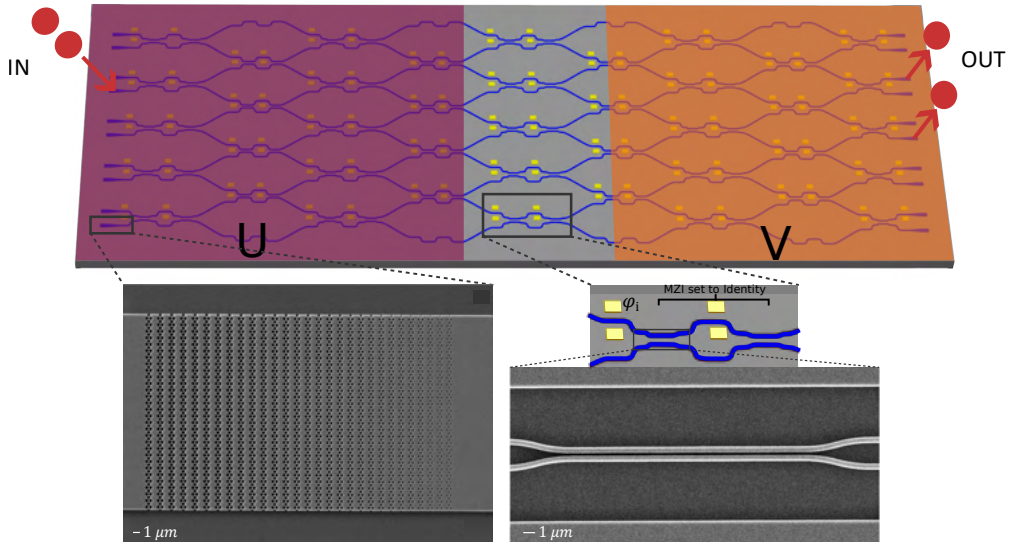

Figure 6.3.4: Three dimensional representation of the photonic chip used for the quantum simulation experiment (Illustrative only, not to scale). The interferometer consists of a network of MZIs and external phase shifters which together create a 10 mode universal Clements-style interferometer [131]. The left Inset shows the SEM image of the Apodized photonic crystal grating coupler used for light coupling. The right inset shows the phase shifters at the center of the chip which apply the spin-mapped phases ϕ_i as long as all of their neighboring MZIs are set to identity.

waveguides have low roughness and that the structure is highly symmetrical on the input and output, showcasing the precision of the fabrication and suggesting very low losses on the directional couplers of the chip.

A more detailed depiction of the interferometer inside the chip is shown in Figure 6.3.5(a). It consists of a 10x10 universal interferometer of the Clemens type [131] with an MZI and an external phaseshifter at every node. Since we did not have two electronic boards, we were only able to access 64 out of the 89 phase shifters in the chip. The unreacheable phase shifters are marked in red. In order to implement a unitary transformation similar to the one in Figure 6.2.1(c), we need the MZIs in the center of the interferometer to be set to identity. Doing so results in the interferometer shown in Figure 6.3.5(b), where we show that we can simulate up to 9 interacting spins with this configuration. In practice we could only simulate 7 spins due to one of the MZIs at the input being broken, forbidding us from doing experiments that access all 9 central phaseshifters In this case the U and V matrices are not universal unitaries as those that may be expected from Figure 6.2.1(c), and we can thus not use this setup for a general quantum simulation of any interacting spin system, but it should suffice to observe the temperature dependent spin dynamics.

Essential to the metropolis algorithm is that the phases in the center of the chip can be switched between two values separated by π, as explained in the theory section.

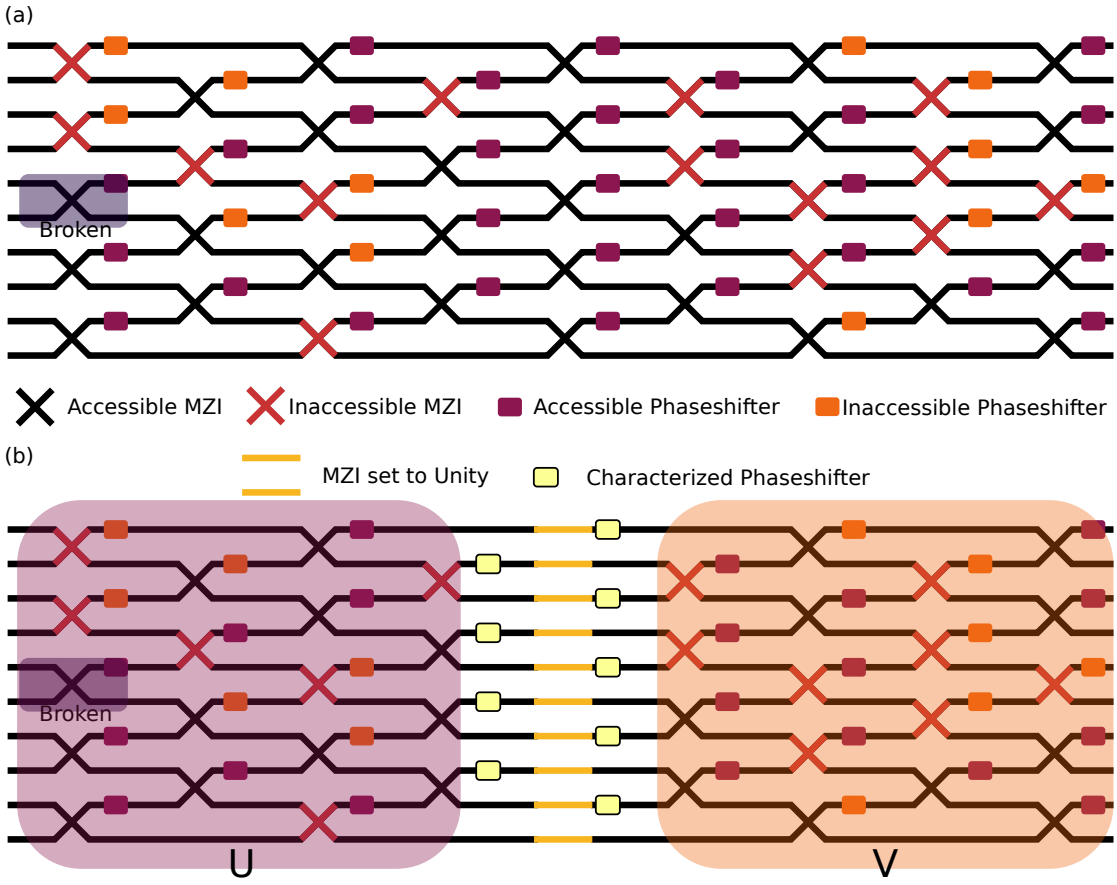

Figure 6.3.5: (a) Schematic of the interferometer in the Si PIC. Due to insufficient equipment, not all the electrical contacts were accessible for the experiment. This lead to certain MZIs and phase shifters being inaccessible. (b) Specifying the U and V matrices in the experiment. A screen of phase shifters between them arises if the MZIs at the center of the interferometer are set to identity.

To this end it is essential to characterize the external phase shifters at the center of the chip with respect to the voltage applied to them. It is also essential to characterize the MZIs at the center of the interferometer such that they can be accurately set to identity. A standardized characterization procedure for a universal interferometer cannot be applied in the case where many of the phase shifters are inaccessible. Instead we characterize the central MZIs and phase shifters highlighted in Figure 6.3.5(b). The MZIs in the two main diagonals are characterized first, and the results from these measurements are used to characterize the MZIs in the sub-diagonals by setting the last MZIs in the main diagonals to identity. The characterization is done in sets of diagonals because in order to know that we are setting the MZIs to specifically identity, we need to make sure that we measure the light from only one output port of the MZI, with no interference from the other output port.

The characterization of an individual MZI happens by sending classical light into an input port reaching the MZI and detecting with a power meter placed at an output that directly depends on the phase applied to the MZI. Scanning the voltage applied to that MZI and recording how the power changes gives interference fringes from where the phase to voltage relation can be extracted using a fit of the intensity curve. Through this procedure all of the relevant MZIs can be characterized and set to identity. The external phases in the center of the chip can be characterized after that as they always form part of a bigger MZI and scanning the phase applied to them will always result in interference at any connected output of the chip.

Simplified experiment

Due to the low efficiency of our single photon source and the very low quality of the emitted single photons, the experimental results described on this thesis will not be those of experiments with a demultiplexed and frequency converted single photon source, but rather those of a simpler experiment, where the two photon component of an attenuated coherent laser is used as the input.

A true single photon source would have the advantage of precise control of the amount of photons being sent into the interferometer, whereas attenuated coherent light can only be used for two-photon experiments and there will always be a small error induced by the presence of higher photon-number states. But using attenuated coherent light suffices for a proof of principle experiment showcasing the central aspects of the experiment.

6.4 Results

Single-photon measurement

We start with the most simple version of the experiment, which from a technical perspective is to send light through the chip using a classical light source and measuring the output with a powermeter. After characterizing the external phase shifters and setting the central MZIs on the chip to identity, we implement the metropolis algorithm as described in the theory section. Doing so should simulate an interacting spin system where only the two-body interaction Hamiltonian is included.

In practice, several valuable insights were gained from the initial runs of the experiment. First, the method to chose which spin is to be flipped was originally set to be at random, but we learned that for the low number of spins that we are simulating it is much more efficient to systematically flip the phases in order. An early termination condition is included such that if all of the phases are shifted and none of them give a relevant increase in the output rate the run will terminate. Second, in practice the power going into the interferometer and coupled out can vary not only due to phases being changed, but also due to instabilities in laser power, polarization drifts and slight changes in the alignment during the experiment. The change in power will necesarily

change the maximum that we try to optimize in the metropolis algorithm over time. For this reason it is important that every time we flip a phase that does not lead to an increase in count rate the phase is reset. This approach ensures that each phase change is compared to the current maximum count rate rather than an outdated maximum that may have drifted due to these instabilities. Third, we observed that power meters

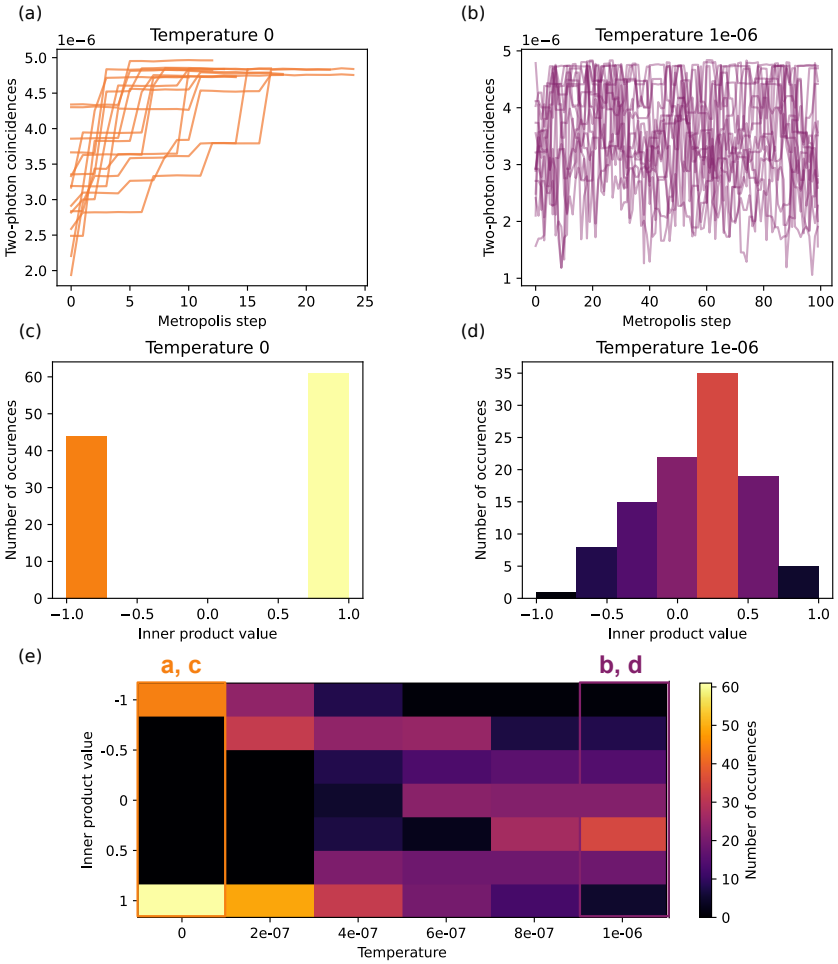

Figure 6.4.1: (a) Results for power-meter-based experiment of the metropolis algorithm (single-photon experiment) for multiple runs. (b) Similar experiment with a high simulated temperature on the programming of the metropolis algorithm. (c) Inner product histogram obtained from the final spin states of the zero temperature experiment. (d) Inner product histogram for the high temperature experiment. (e) 2D histogram of the inner product for different temperature values in the metropolis algorithm.

exhibit a slow response to changes in measured power. To address this, a delay was introduced after each phase shift to allow the measured power to stabilize. This issue could alternatively be mitigated by using faster power meters or by measuring single

count rates with single-photon detectors.

The results of doing multiple rounds with the metropolis algorithm can be seen in Figure 6.4.1(a), which consists of 15 runs with maximally 100 metropolis steps in each of them. The power on the y-axis can be seen to increase as we flip the spins, showing that the success probability is indeed increased through the algorithm. For the zero temperature measurement it can be observed that there is only one maximum, suggesting that this is the global maximum for the simulated spin system. The different spin states achieved through the algorithm are collected and all of their inner products to respect to each other are computed. The different attained values for the inner products are gathered in a histogram as shown in Figure 6.4.1(c), where for this configuration we can see that ferromagnetic behaviour is achieved in the zero temperature case, while it exhibits a Gaussian behaviour in the high temperature case, shown in Figure 6.4.1(b) and (d). We thus see highly ordered behaviour for low temperatures and chaotic behaviour for high temperatures, as expected from a 1D array of interacting spins.

We show the behaviour of the simulated spin system for a wide range of temperatures in Figures 6.4.1(e), where the transition from a ferromagnetic state to a random mixed state can be closely observed.

The input mode was chosen to be one that could reach all the 7 relevant spins, and the output mode was selected to be one with a ferromagnetic signature. The input and output modes used were chosen at random. From a theoretical perspective, changing the input and output modes corresponds to changing the $\vec{c}$ and $\vec{k}$ vectors in equation 6.2.8, which in the end corresponds to simulating a slightly different J matrix in the interacting-spin Hamiltonian. We tried redoing the experiment for different input-output configurations and observed that similarly to figure 6.2.3(a), many configurations led to Ferromagnetic behaviour. We will later discuss what effect is achieved from varying the V matrix in the interferometer.

Two-photon measurements

Having tested the metropolis algorithm through simple classical light measurements we proceed to performing a quantum experiment where the light source is a highly attenuated classical laser, but the detectors are SNSPDs. For this experiment we optimize the coincidence counts on a pair of detectors following two output modes from the chip. Given that we are dealing with a coherent input state, if the light is sufficiently attenuated, the probability of having 3 or more photon states propagating through the interferometer becomes negligible, making this an experiment where two photons interfere with each other. In doing so we simulate an interacting spin system Hamiltonian that includes up to four-body interactions.

The results of running the metropolis algorithm for the described two-photon experiment with a given configuration of input and output modes is shown in Figure 6.4.2(a) for the zero temperature case. The corresponding histogram over the inner products of the resulting spin states is shown in Figure 6.4.2(c). We see that this

system exhibits ferromagnetic behavior even though there seems to be two different energies for the final spin configurations. From a purely theoretical perspective, this result is unexpected and is likely explained by fluctuations in the photon flux through the chip over the course of the experiment. The results obtained by running the

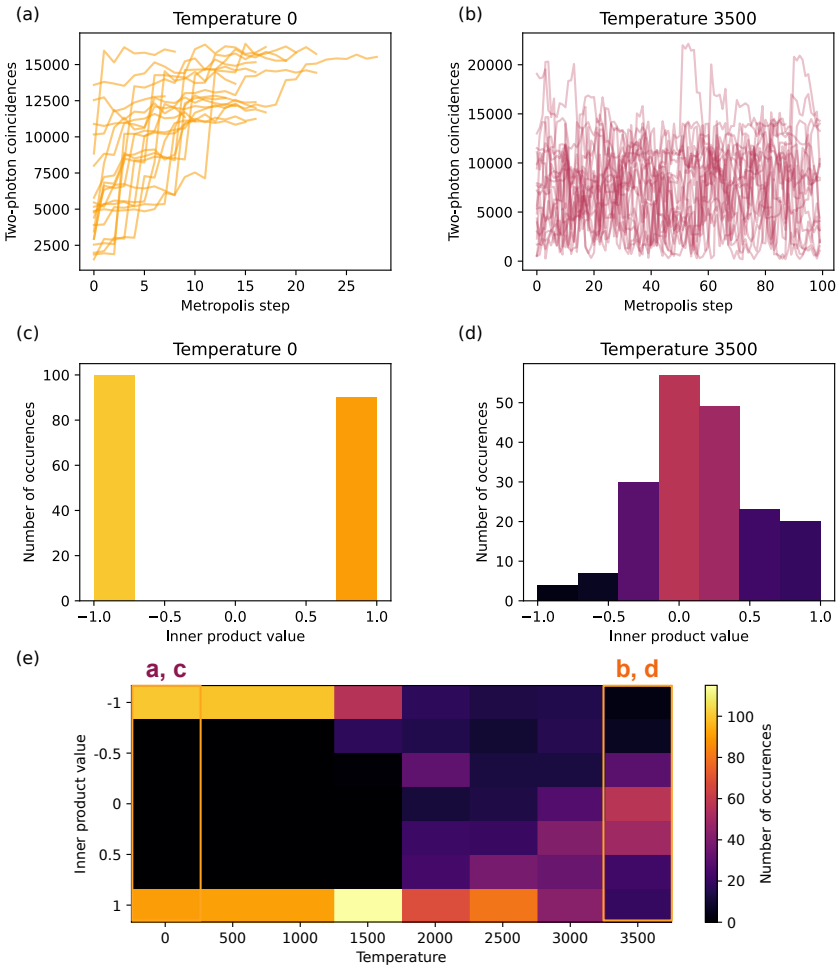

Figure 6.4.2: (a) Results for two photon experiment of the metropolis algorithm. (b) Similar experiment including a high temperature on the programming of the metropolis algorithm. (c) Inner product histogram obtained from the final spin states of the zero temperature experiment. (d) Inner product histogram for the high temperature experiment. (e) 2D histogram of the inner product for different temperature values.

metropolis algorithm for the same system but at a high temperature is shown in Figure 6.4.2(b) and (d). It can be observed that the metropolis algorithm never manages to find an optimum energy state and that the final spin states form a Gaussian distribution for their inner-product histogram, meaning that it is random which spin state the algorithm arrives to.

We have thus shown that the dynamics of an interacting spin system described

by a four-body Hamiltonian exhibiting ferromagnetic behaviour at zero temperature can be simulated using interferometers in PICs. Our approach allows us to see what temperature is required to achieve a phase transition in the magnetic state of the spin-system.

A noteworthy error source is the power of the input laser, as it should be low in order to isolate the two-photon component at the input. For a pulsed laser, the value α used to characterize its coherent state can be calculated given the count rate c and the laser repetition rate r by

$$|\alpha|^2 = \langle n \rangle = \frac{c}{r}, \tag{6.4.1}$$

which for our range of count rates a repetition rate of 80 MHz becomes results in a 3 photon component that is a 4-8% as likely as the two-photon component.

In a setup with losses it can be confusing to determine which losses to take into account in the measure of the power fed into the equation. Given that photons do not interact and only interfere, the correct point to measure the power is right before the detectors, such that all the losses of the setup should be included but not the detection efficiency.

Different spin systems

So far we have shown that interacting-spin dynamics are exhibited by applying the metropolis algorithm in a two-photon experiment. However, in this experiment the J matrix of the simulation was fixed, i.e. only one type of interacting spin system. This system exhibited ferromagnetic behavior when simulated both with the two- and four-body Hamiltonian. Since we want to show that we are able to simulate many different types of spin-dynamics with our chip, we will now focus on simulation of different spin systems with other J matrices.

The J matrix that is simulated can be varied by changing the input-output configurations or by changing the U and V matrix transformations. In our experiment we can freely change the output configuration of the detectors, but the input configuration is limited to always sending two photons to the same input. This limitation can be lifted by using the demultiplexed SPS. Unfortunately the coincidence count rate we had with the SPS was too low to be able to run the metropolis algorithm since the baseline source efficiency was very low, preventing us from conducting the experiment with the QD. Additionally, the U and V matrices in our chip did not perform universal transformations and we were also not able to control all of the phase-shifters within them. Despite these constraints, we are still able to implement a range of variations, allowing us to conduct a proof-of-principle experiment that demonstrates that this platform can simulate the dynamics of different spin systems.

For our experiment we decided to randomly vary the V matrix and run the metropolis algorithm many times for a two-photon experiment. Figure 6.4.3(a) shows 4 different results of the inner-product histogram obtained after setting random values for the V matrix and doing multiple runs of the metropolis algorithm. We can see that none of them exhibit ferromagnetic behavior and they all have unique non-gaussian

signatures. This is in agreement with the simulation shown in Figure 6.2.3(b). It is

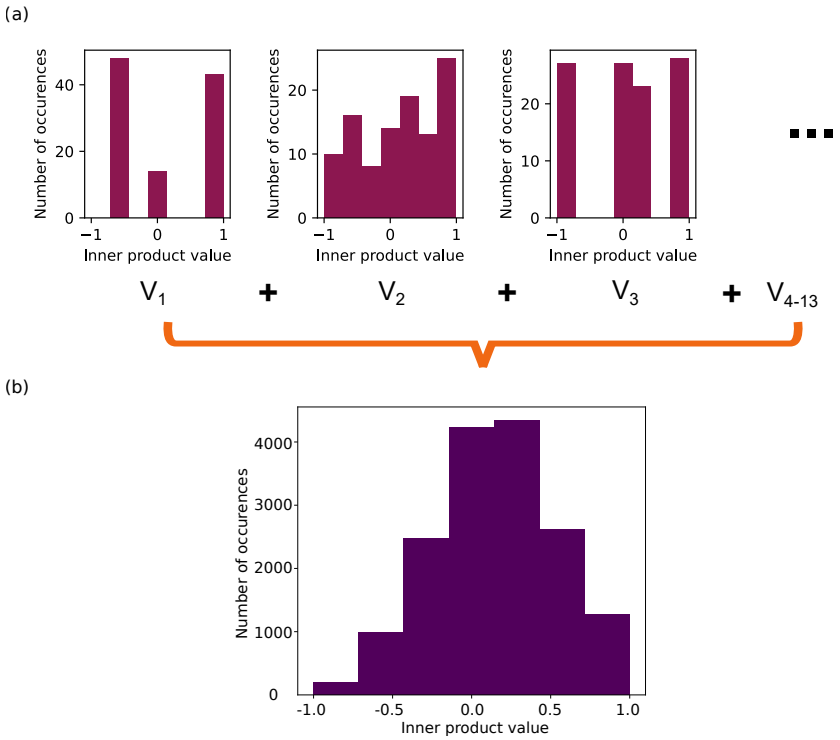

Figure 6.4.3: (a)Inner-product histograms for different individual configurations of the U and V matrices. (b) Combined histogram of all the data regardless of the U and V matrix configurations.

possible that our photonic chip may have an inherent bias toward certain spin configurations, either due to phase shifters not flipping properly or due to some paths in the chip having more loss than others. To address this concern, we present Figure 6.4.3(b), which shows a histogram of all inner-product values combined. The histogram reveals a Gaussian distribution, indicating that the values are entirely random with respect to one another and lack any inherent structure. From this we can conclude that different configurations of the spin matrix can lead to different ground state configurations in our simulation, and that our chip has no hardware-driven preference for specific spin configurations.

6.5 Conclusion

Interacting spin systems are physical models with numerous real-world applications, often displaying complex dynamics that are challenging to simulate on a classical computer. In this chapter we describe a mapping between interacting spin systems and photonic circuits. Through this mapping it is possible to simulate the ground state

dynamics of a spin system by applying an algorithm on a photonic interferometer called the metropolis algorithm. We propose an experimental setup that is able to simulate any interacting-spin system relying on single photons produced with QD single-photon sources and photonic information processing in silicon-based PICs. Due to technical limitations with our QD SPS we proceed to showcasing a proof of principle experiment where the emitter is replaced with an attenuated coherent light source.

We experimentally demonstrate that we are able to simulate interacting-spin systems described by both two and four-body Hamiltonians, where we can find their ground state configuration and their dynamics as the temperature increases.

We present an example of a classical system that can be efficiently simulated using an analog photonic quantum simulator, demonstrating the potential of quantum systems for practical applications.

Chapter 7

Concluding remarks and outlook

Photonic quantum computers are promising candidates for solving complex problems that are hard to solve using classical computers. In this thesis we take experimental steps to understand the basic requirements of photonic quantum computing, and find some specific problems they can be applied for.

The central approach to quantum computing that is studied is that of fusion-based quantum computing (FBQC). We describe the underlying principles of FBQC in Chapter 3 and discuss how it can be achieved with quantum emitters. We then proceed to describe a first proof-of-principle experiment where we perform the first example of a fusion between deterministically-generated entangled resource states using a quantum emitter. Apart from a proof-of-principle demonstration of fusion, our experiment has the curious result of generating entanglement of a quantum-emitter spin with itself at a different time. This not only showcases one of the peculiarities of quantum mechanics, but it also demonstrates that the time dimension can be employed for further scaling of fusion networks, reducing the hardware requirements for a given computation.

To move from a proof-of-principle experiment to a large-scale technology capable of solving problems requiring a high amount of operations, we interface our quantum emitters with photonic integrated circuits (PICs). Chapter 4 describes our experiments where a quantum dot source emits single-photons that are processed on SiN PICs. We start by describing basic experiments like the HBT and HOM experiments and proceed to slightly more complex ones like showcasing the bosonic suppresion laws for a four-mode interferometer. We demonstrate the feasibility of this platform when it comes to fusion-based quantum computation by testing the fidelity of a path-encoded fusion operation. The circuit for a fusion operation is equivalent to the circuit required for probabilistic Bell state generation, thus measuring the fidelity of the generated entangled state gives a measure of the expected fusion fidelity. We find that the main limitation for achieving very high fusion fidelities are fabrication imperfections and distinguishability of the emitted photons.

Improving the indistinguishability of single photons is not only relevant for our specific implementation of a fusion operation, but also essential for most quantum computing protocols requiring single photons. We describe in Chapter 5 a protocol

that can increase the indistinguishability of a set of single photons by quantum interference and detection on a subset of them. We perform an experiment where the simplest possible implementation of the protocol is tested. We find that our indistinguishability purification protocol indeed increases the indistinguishability of the photons, independently of the mechanisms that are responsible for creating distinguishability between the photons.

Even though we set up the foundations for the construction of a universal quantum computer, we show that there are more immediate applications of quantum emitters and PICs. We describe in Chapter 6 a mapping between the Hamiltonian of a system of interacting spins and the scattering probability of photons propagating through a photonic interferometer. We perform a proof-of-principle experiment where we demonstrate that the dynamics of the ground state of certain spin glasses are replicated with an interferometer on a silicon PIC. We thus show an analogue quantum simulation of a classical system using the technologies studied during this thesis.

Outlook

FBQC with deterministic entanglement

Slight adjustments and improvements to the experimental setup used for the temporal fusion experiment would allow the exploration of some relevant and interesting concepts.

The use of the protocol as a quantum memory, where the state of the spin is encoded in a photon, was not explored. In order to do so, a slight adjustment to the pulse sequence would convert the protocol from an entanglement protocol to a teleportation protocol. Varying the delay length while monitoring the fidelity of the teleported state could reveal important information about the possibilities and limitations of teleporting information forward in time using light. Further increase of the collection efficiency and the spin-photon entanglement fidelity would allow for generation of larger entangled resource states at a higher rate. This would allow both for creation of larger temporal fusion networks, giving the opportunity to investigate entanglement percolation for bigger scale implementations. Alternatively, the larger resource states can be applied in fault-tolerant fusion schemes requiring an emitter simultaneously entangled to multiple photons [134, 135].

Apart from quantum memory, fusions may play a vital role in creating networks for the making of functional quantum computers.

Our current implementation involves only one emitter, which is fused with itself through free space optics. In this situation, free space optics gives the highest possible efficiency for the protocol. Further scaling of fusion networks will inevitably require operations with photons from many different emitters, in which case the required photonic interferometers to realize the fusions will quickly grow in size and complexity. Performing the fusion operations on PICs like those studied in this thesis will offer a route to implement the required circuits in a simple and scalable fashion.

FBQC with probabilistic entanglement

An alternative route to entanglement generation is through heralded probabilistic operations, requiring measurement-based non-linearities. This approach is less efficient but far more simple from a hardware perspective, as it only requires single photons, a demultiplexer, a PIC and single photon detectors, without the need for magnetic fields or multiple excitation lasers. In this thesis we discussed the use of PICs with schemes for heralded entanglement generation. Large PICs with multiple entanglement generation modules can be combined with fusion circuits on the same platform, allowing for direct implementation of FBQC within one chip.

For this approach it is essential to have highly indistinguishable photons, so protocols for indistinguishability purification may be necessary. Our protocol is probabilistic with a low success probability, reason why it may not be directly applicable for a full scale quantum computer. But since our work, other theoretical proposals for indistinguishability purification have been made, with improved hardware performance [113, 120, 121]. It is possible that clever design of photonic circuits can directly include indistinguishability purification within the applied operations. Improved use of indistinguishability purification opens a path for the use of imperfect sources for fault-tolerant quantum computing.

* * *

Further in the future, quantum emitters and PICs may be directly combined through heterogeneous integration. This would increase the efficiency of the platform combination and make the whole setup even more scalable. A photonic quantum computer may in the end be comprised in a single chip where all of the functionalities are integrated. It is not clear which designs or architectures will be used at that point, but we can for certain say that some of the first steps to get there were taken during the work described in this thesis.

Appendices

Appendix A

Appendix for Chapter 3

Statement of work

The following error analysis was performed by Yijian Meng and Ming Lai Chan, and the text explaining it is taken from the supplementary material of [42]

Monte-Carlo Fidelity Simulations

To analyze the impact of experimental imperfections on the state infidelity, we conducted Monte-Carlo (MC) simulations, incorporating error parameters detailed in Supplementary Table A.1. The details of MC simulation, including how error sources are incorporated, are described in Ref. [37]. The outcomes of these simulations for the current experiment are summarized in Supplementary Table A.2. To discern the contribution of individual error sources, we initially ran simulations considering all errors, resulting in an entanglement fidelity $\mathcal{F}_o$. We found $\mathcal{F}_o = 52\%$ for both ψ_+ and ψ_- states, which is similar to the experimental results.

The simulation follows the experimental generation and detection procedure, employing 12 measurement configurations to project early and late spin states into one of the three bases: X, Y, or Z. For each spin state, we simulate over 5000 realizations.

To simulate the detection procedure based on two-photon events on the detector, we also include an additional drop in photon visibility attributed mostly to imperfect path delay and polarization drift in the detection interferometer. To evaluate this effect, we perform a Hong–Ou–Mandel measurement[27], measuring the visibility between early and late photons that are 300 ns apart, resulting in $V_f = 68(1)\%$. We compare this with the visibility measured when the photons are 12 ns apart while other settings are similar, i.e., $V_i = 84(1)\%$[37]. The relative drop in visibility due to the delay is quantified by the formula $1 - V_i/V_f = 19\%$.

Subsequently, we conducted a second simulation to find the infidelity caused by the different error sources. We denote the lack of a specific error source p, to yield a fidelity $\mathcal{F}_p$. The infidelity attributed to an error source p can be estimated as $\mathcal{F}_p - \mathcal{F}_o$. While this method assumes the errors are independent, it provides a valuable

estimate for prioritizing further optimization efforts. Supplementary Table A.2 lists the contribution from all known error sources.

The highest contribution comes from off-resonant excitation, which happens when we excite the opposite diagonal transition than the one we are interested in. The two diagonal transitions are separated by 9 GHz, while our pulsed laser used for excitation has a bandwidth of 20 GHz. In order to avoid exciting both transitions we tune the frequency of the excitation laser slightly away from the other transition, but unwated excitations are unavoidable. The next two significant error sources are nuclear spin noise and incoherent spin-flip during rotation pulse.

It should be noted that many of the listed error sources when combined will correlate destructively such that the total error provided by them is more than the sum of their individual errors. For example the negative effect of off-resonant excitation would be magnified by a population increase in the off-resonant spin state under an imperfect spin π-rotation pulse.

Parameters	
Radiative lifetime $1/\Gamma$	235 ps
Cyclicity C	36
Spin rotation Q-factor Q	34
Spin readout fidelity F_{r}	99%
Spin initialization fidelity F_{int}	99%
Pure dephasing rate γ_d	0.069 ns^{-1}
Excitation laser detuning	$-2GHz$
Frequency splitting between cycling transitions Δ	10 GHz
Excitation pulse shape	Gaussian
Excitation pulse area	0.7π
Excitation pulse duration (FWHM intensity)	30 ps
High-frequency nuclear spin noise	Modelled as in [37]
Visibility reduction from 300 ns delay	-19%

Table A.1: List of parameters used for the simulation. The excitation laser detuning is the detuning of the excitation laser relative to the targeted cycling transition. The amplitude of nuclear spin noise is extracted from the spin echo visibility measurement, see Ref. [37].

All error sources	**Infidelity**
Off-resonant excitation	8.5 %
Nuclear spin noise	4.3 %
Spin-flip error during rotation	3.7 %
Visibility reduction from 300 ns delay	1.6 %
Spin readout error	1.1 %
Phonon-induced pure dephasing	0.7 %

Table A.2: Infidelity contribution of all simulated errors. The infidelity contribution due to an error p is calculated as the difference in simulated fidelity with and without the error source p.

Appendix B

Appendix for Chapter 4

Heralded entanglement generations circuits

We show the circuit design of the interferometers we had in our chip in Figure B.0.1. The heralded Bell state generation interferometer is shown in part (a), which is also the one that was used for all of the 2 photon experiments reported in Chapter 4, where different subsets of it were used for the different experiments. We show a zoom in of the directional couplers and the phase shifters on the chip. The electrical pads that connect to the different phaseshifters can also be appreciated at the botoom of the figure.

In part (b) we show the circuit required for heralded GHZ statet generation. The circuit has 12 inputs and 12 outputs, requiring a fiber array with a minimum size of 24 fibers.

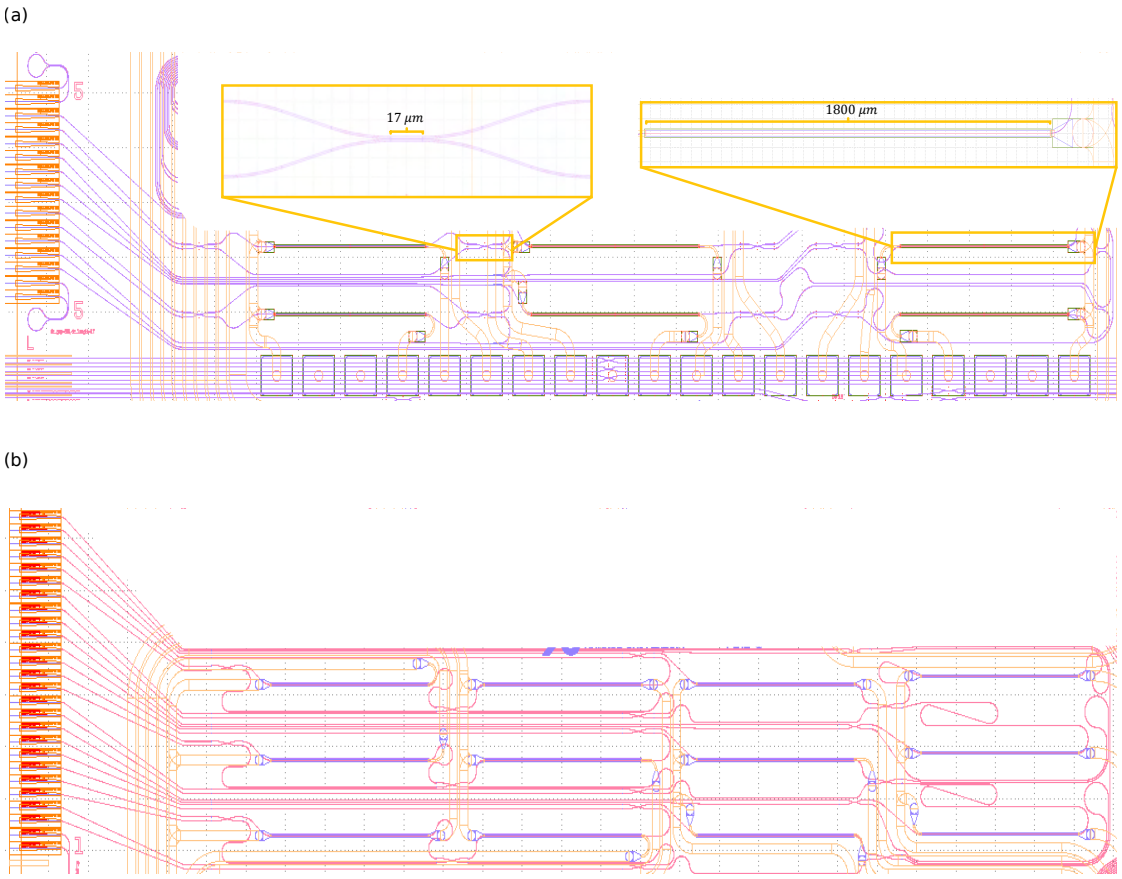

Figure B.0.1: (a) On chip circuit design of a Heralded Bell state generation interferometer. The directional couplers and phase shifters are all equally designed and specified on the inset. (b) On chip circuit desing of a 3-photon heralded GHZ state generation interferometer.

Appendix C

Appendix for Chapter 5

Statement of work

The equations presented in this appendix were derived by Patrik Isene Sund in collaboration with the author of this thesis. The text is taken from the appendix of [32].

Estimating HOM visibility from central and side peaks

We will start by investigating the setup used for the measurement of the raw HOM visibility, shown in Fig.C.0.1(a). The beamsplitters in this setup had close to 50:50 splitting ratio, except for the second two which had splitting ratios of 45:55, with 55% of incoming light would be reflected (i.e. exit from the other port of the beamsplitter). In order to get a central peak, both photons will have to reach the final beamsplitter. Expressing the system efficiency as t, the probability of two input photons producing a central peak, $P_{\mathrm{c,raw}}$ will be equal to:

$$P_{\mathrm{c,raw}} = t^2 \cdot 0.5^2 \cdot 0.55^2 \cdot \frac{1}{2}\left(1 - V_{\mathrm{raw}}\right), \tag{C.0.1}$$

where V_{raw} is the raw HOM visibility to be measured. To estimate the probability of a side-peak, we first note that our setup produces strings of pairs of photons at a repetition rate of 10 MHz, where each photon-pair instance can be considered a time-bin. A positive (negative) side-peak is the result of the top (bottom) output detector clicking in one time-bin, and the bottom (top) detector clicking in the subsequent time-bin. As the probability of producing a click in the top output detector and bottom output detector is equal, the probability of generating a side-peak $P_{\mathrm{s,raw}}$ this is equal to the product of the probability of producing a click in a specific output detector $P_{\mathrm{1D,raw}}$ ("one detector")

$$P_{\mathrm{s,raw}} = P_{\mathrm{1D,raw}}^2.$$

A detector click in a specific output detector can be produced in a number of ways in any given time-bin. In the case that a single-photon is lost (either the upper input

photon or the lower input photon), the remaining photon will have to take the correct path through three consecutive beamsplitters. If two photons survive, a click can be produced either if both photons reach the final beamsplitter and do not bunch on the bottom output detector, or if only one of the two photons takes the correct path through three consecutive beamsplitters while the other photon does not reach the final detector. Combining all terms, the probability can be written as

$$\begin{aligned} P_{\text{1D,raw}} =& 2 \cdot t(1-t) \cdot 0.5^2 \cdot 0.55 \\ &+ t^2 \Big(0.5^2 \cdot 0.55^2 \cdot \frac{1}{4}(3 - V_{\text{raw}}) \\ &\quad + 2 * 0.5 \cdot 0.55 \cdot (1 - 0.5 \cdot 0.55) \cdot 0.5 \Big), \end{aligned} \tag{C.0.2}$$

where the first term contains a factor of $t(1-t)$ to take into account that one photon should survive and exactly one photon should be lost.

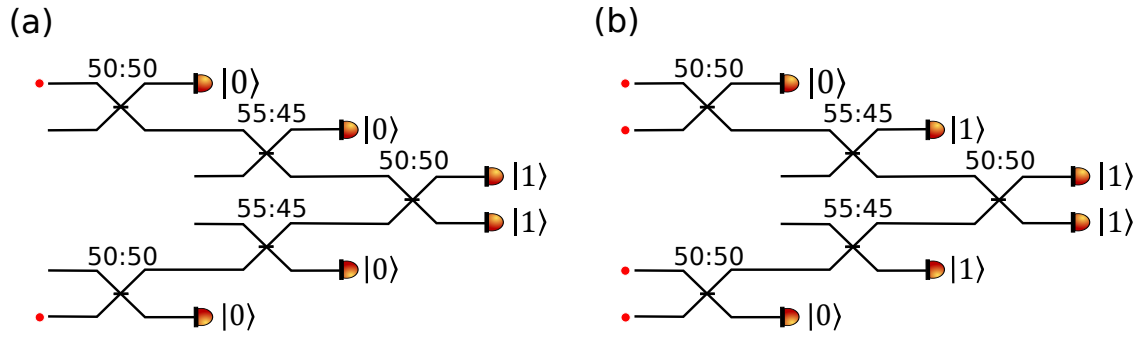

Figure C.0.1: Experimental setups used for the measurement of the raw (a) and purified (b) HOM visibilities, with realistic values for the BS reflecivities according to the manufacturer.

To estimate the raw HOM visibility, we optimize both t and V_{raw} to fit the central peak counts, and the side-peak counts from the coincidence measurement, one of which is shown in Fig. 3(a) in the main text. For the raw measurement, the repetition rate of the experiment was 10 MHz, and the integration time was 30s, and as such we can estimate both the system efficiency and the raw visibility by fitting the following two equations to the experimental data

$$10 * 10^6 \cdot 30 \cdot P_{\text{c,raw}} = \text{central-peak counts} \tag{C.0.3}$$

$$10 * 10^6 \cdot 30 \cdot P^2_{\text{1D,raw}} = \text{side-peak counts} \tag{C.0.4}$$

A similar analysis can be performed for the setup used to measure the purified HOM visibility, shown in Fig.C.0.1(b). In this setup, pairs of output detectors are gated, such that the upper (lower) output detector only records a click if the upper

(lower) herald detector clicks simultaneously. For the central peak, we require that all four photons make it to the correct detectors. This happens with probability

$$\begin{aligned} P_{\text{c,pure}} &= t^4 \cdot P_{\text{bunch}}^2 \cdot P_{\text{split}}^2 \cdot 0.5 \cdot (1 - V_{\text{pure}}), \\ P_{\text{bunch}} &= 0.25 \cdot (1 + V_{\text{raw}}), \\ P_{\text{split}} &= 2 \cdot 0.55 \cdot 0.45, \end{aligned} \tag{C.0.5}$$

where P_{bunch} is the probability that two input photons bunch on the first beamsplitter, P_{split} is the probability that two bunched photons split on the second beamsplitter, and where V_{pure} is the purified HOM visibility.

As for the side-peak, we now have four photons per time-bin, and to produce a side-peak we require that at least one photon reaches the correct herald detector and that at least one photon reaches the corresponding output detector for two successive time-bins, to which we attribute the probability $P_{\text{1D,pure}}^2$ similarly to case for raw visibility. We can break this down to where the two top photons go and where the two bottom photons go. For the two top photons, we will get contributions from three cases:

1. One photon goes to the herald, one goes to the top input mode of the final beamsplitter, which we label P_{h1t1}.

2. One photon goes to the herald, no photon arrives in the top input mode of the final beamsplitter, which we label P_{h1t0}.

3. Two photons go to the herald such that no photon arrives in the top input mode of the final beamsplitter, which we label P_{h2t0}.

These three cases have probabilities

$$P_{\text{h1t1}} = t^2 \cdot P_{\text{bunch}} \cdot P_{\text{split}}, \tag{C.0.6}$$

$$\begin{aligned} P_{\text{h1t0}} = t \cdot \Big(& 2 \cdot (1 - t) \cdot 0.5 \cdot 0.45 \\ & + t \cdot (1 - 2P_{\text{bunch}}) \cdot 0.45 \Big), \end{aligned} \tag{C.0.7}$$

$$P_{\text{h2t0}} = t^2 \cdot P_{\text{bunch}} \cdot 0.45^2. \tag{C.0.8}$$

For P_{h1t0} the first term in the parentheses represents the case where only one photon survives (which can happen in two ways), whereas the second term represents the case where both photons survive.

For the two bottom photons, we similarly can get contributions from three cases:

1. No photons arrive at the bottom input mode of the final beamsplitter, which we label P_{b0}.

2. One photon arrives at the bottom input mode of the final beamsplitter, which we label P_{b1}.

3. Two photons arrive at the bottom input mode of the final beamsplitter P_{b2}.

These three cases have probabilities

$$P_{\mathrm{b1}} = t \cdot \Big(2 \cdot (1-t) \cdot 0.5 \cdot 0.55 + t \cdot (P_{\mathrm{bunch}} \cdot P_{\mathrm{split}} + (1 - 2P_{\mathrm{bunch}}) \cdot 0.55)\Big) \tag{C.0.9}$$

$$P_{\mathrm{b2}} = t^2 P_{\mathrm{bunch}} \cdot 0.55^2, \tag{C.0.10}$$

$$P_{\mathrm{b0}} = 1 - P_{\mathrm{b1}} - P_{\mathrm{b2}}. \tag{C.0.11}$$

In the definition of P_{b1}, the first term in the parentheses represents the case where only one photon survives, whereas the second term represents the case where both photons survive at the start, at which point a single photon can reach the output either by the photons bunching at the first beamsplitter and splitting at the second, or by the two photons splitting at the first beamsplitter, after which one photon reaches the final beamsplitter.

Finally, there are four different input configurations at the final beamsplitter that can lead to a side-peak contribution:

1. One input photon in one of the input modes, no photons in the other, which we label $P_{\text{single input}}$.
2. One input photon in each input mode, which we label $P_{\text{split input}}$.
3. Two photons in one of the input modes, no photons in the other, which we label $P_{\text{bunched input}}$.
4. One photon in the top mode, two photons in the bottom mode, which we label $P_{\text{three photon input}}$.

We model the probabilities of these three cases as follows

$$P_{\text{single input}} = 0.5, \tag{C.0.12}$$

$$P_{\text{split input}} = 0.25 \cdot (3 - (V_{\mathrm{raw}} + V_{\mathrm{pure}})/2)\,, \tag{C.0.13}$$

$$P_{\text{bunched input}} = 0.75, \tag{C.0.14}$$

$$P_{\text{three photon input}} = 1 - 0.125\,(1 + 2V_{\mathrm{pure}})\,, \tag{C.0.15}$$

For the split input case, one of the photons has been purified, whereas the other has not (except for the case where both herald detectors click, which we will introduce separately). Therefore, we approximate the HOM visibility as the average between the pure and raw HOM visibility, and the expression is the expectation value that the two photons do not bunch on the bottom detector. In the three photon input case, all three photons have successfully been purified, so we use the pure HOM visibility. The probability is then the expectation value of the probability that all three photons do not bunch on the bottom detector.

Considering all combinations that can lead to a side-peak, we can write $P_{\text{1D,pure}}$ as

$$\begin{aligned} P_{\text{1D,pure}} = &(P_{\text{h1t0}} + P_{\text{h2t0}}) \cdot (P_{\text{b1}} \cdot P_{\text{single input}} + P_{\text{b2}} \cdot P_{\text{bunched input}}) \\ &+ P_{\text{h1t1}} \cdot (P_{\text{b0}} \cdot P_{\text{single input}} + P_{\text{b1}} \cdot P_{\text{split input}} + P_{\text{b2}} \cdot P_{\text{three photon input}}) \\ &- P_{\text{two-purified}} \cdot P_{\text{split input}} + P_{\text{two-purified}} \cdot 0.25 \cdot (3 - V_{\text{pure}}). \end{aligned} \tag{C.0.16}$$

The final line here represents a correction for the fact that part of $P_{\text{h1t1}} \cdot P_{\text{b1}} \cdot P_{\text{split input}}$ contains a contribution where both photons have been purified, such that the probability of the top detector clicking is $0.25 \cdot (3 - V_{\text{pure}})$. The term $P_{\text{two-purified}}$ is the probability of the state before the final beamsplitter that can lead to a coincidence click, i.e.

$$P_{\text{two-purified}} = t^4 \cdot P_{\text{bunch}}^2 \cdot P_{\text{split}}^2.$$

Noting that the repetition rate of the input was 10 MHz and that the integration time was 800s, the purified HOM visibility and system efficiency can be calculated by solving the following set of equations with the purified visibility V_{pure} and the efficiency of the setup t as the free variables.

$$10 * 10^6 \cdot 800 \cdot P_{\text{c,pure}} = \text{central-peak counts}, \tag{C.0.17}$$

$$10 * 10^6 \cdot 800 \cdot P_{\text{1D,pure}}^2 = \text{side-peak counts}. \tag{C.0.18}$$

We solve the equations numerically using the least squares method.

Bibliography

[1] Richard P Feynman. "Simulating physics with computers". In: *Feynman and computation*. cRc Press, 2018, pp. 133–153.

[2] Richard P Feynman. "Quantum mechanical computers." In: *Found. Phys.* 16.6 (1986), pp. 507–532.

[3] Samuel L Braunstein and Peter Van Loock. "Quantum information with continuous variables". In: *Reviews of modern physics* 77.2 (2005), pp. 513–577.

[4] Takao Aoki et al. "Quantum error correction beyond qubits". In: *Nature Physics* 5.8 (2009), pp. 541–546.

[5] Kasper Jensen et al. "Quantum memory for entangled continuous-variable states". In: *Nature Physics* 7.1 (2011), pp. 13–16.

[6] Mitsuyoshi Yukawa et al. "Generating superposition of up-to three photons for continuous variable quantum information processing". In: *Optics express* 21.5 (2013), pp. 5529–5535.

[7] Mikkel V Larsen et al. "Deterministic generation of a two-dimensional cluster state". In: *Science* 366.6463 (2019), pp. 369–372.

[8] David C Burnham and Donald L Weinberg. "Observation of simultaneity in parametric production of optical photon pairs". In: *Physical Review Letters* 25.2 (1970), p. 84.

[9] Shigeki Takeuchi. "Recent progress in single-photon and entangled-photon generation and applications". In: *Japanese Journal of Applied Physics* 53.3 (2014), p. 030101.

[10] Marcus W Doherty et al. "The nitrogen-vacancy colour centre in diamond". In: *Physics Reports* 528.1 (2013), pp. 1–45.

[11] Gang Zhang et al. "Material platforms for defect qubits and single-photon emitters". In: *Applied Physics Reviews* 7.3 (2020).

[12] Ghulam Murtaza et al. "Efficient room-temperature molecular single-photon sources for quantum key distribution". In: *Optics Express* 31.6 (2023), pp. 9437–9447.

[13] Martin Mücke et al. "Generation of single photons from an atom-cavity system". In: *Physical Review A* 87.6 (2013), p. 063805.

[14] Peter Lodahl, Sahand Mahmoodian, and Søren Stobbe. "Interfacing single photons and single quantum dots with photonic nanostructures". In: *Reviews of Modern Physics* 87.2 (2015), p. 347.

[15] Xing Ding et al. "On-demand single photons with high extraction efficiency and near-unity indistinguishability from a resonantly driven quantum dot in a micropillar". In: *Physical review letters* 116.2 (2016), p. 020401.

[16] Ravitej Uppu et al. "Scalable integrated single-photon source". In: *Science advances* 6.50 (2020), eabc8268.

[17] Ravitej Uppu et al. "Quantum-dot-based deterministic photon–emitter interfaces for scalable photonic quantum technology". In: *Nature nanotechnology* 16.12 (2021), pp. 1308–1317.

[18] Hui Wang et al. "Boson sampling with 20 input photons and a 60-mode interferometer in a 1 0 14-dimensional hilbert space". In: *Physical review letters* 123.25 (2019), p. 250503.

[19] H. Cao et al. "Photonic Source of Heralded Greenberger-Horne-Zeilinger States". In: *Phys. Rev. Lett.* 132 (13 Mar. 2024), p. 130604. DOI: 10.1103/PhysRevLett.132.130604. URL: https://link.aps.org/doi/10.1103/PhysRevLett.132.130604.

[20] Mujtaba Zahidy et al. "Quantum key distribution using deterministic single-photon sources over a field-installed fibre link". In: *npj Quantum Information* 10.1 (2024), p. 2.

[21] Mark A Reed. "Quantum dots". In: *Scientific American* 268.1 (1993), pp. 118–123.

[22] Xiaoyan Zhou, Liang Zhai, and Jin Liu. "Epitaxial quantum dots: a semiconductor launchpad for photonic quantum technologies". In: *Photonics Insights* 1.2 (2023), R07–R07.

[23] BA Joyce. "Molecular beam epitaxy". In: *Reports on Progress in Physics* 48.12 (1985), p. 1637.

[24] AJ Bennett et al. "Electric-field-induced coherent coupling of the exciton states in a single quantum dot". In: *Nature Physics* 6.12 (2010), pp. 947–950.

[25] Juan Marquez, Lutz Geelhaar, and Karl Jacobi. "Atomically resolved structure of InAs quantum dots". In: *Applied Physics Letters* 78.16 (2001), pp. 2309–2311.

[26] Freja Thilde Pedersen. "Deterministic Single and Multi-Photon Sources with Quantum Dots in Planar Nanostructures". PhD thesis. Niels Bohr Institute, University of Copenhagen, 2020. URL: https://nbi.ku.dk/english/theses/phd-theses/freja-thilde-pedersen/.

[27] Martin Hayhurst Appel. "A Quantum Dot Source of Time-Bin Multi-Photon Entanglement". PhD thesis. Niels Bohr Institute, University of Copenhagen, 2021. URL: `https://nbi.ku.dk/english/theses/phd-theses/martin-hayhurst-appel/`.

[28] Ming Lai Chan. "Spin-Photon Interface for Quantum Information Processing". PhD thesis. Niels Bohr Institute, University of Copenhagen, 2021. URL: `https://nbi.ku.dk/english/theses/phd-theses/ming-lai-chan/`.

[29] Peter Lodahl et al. "Controlling the dynamics of spontaneous emission from quantum dots by photonic crystals". In: *Nature* 430.7000 (2004), pp. 654–657.

[30] Michael Reck et al. "Experimental realization of any discrete unitary operator". In: *Physical review letters* 73.1 (1994), p. 58.

[31] Eva M González-Ruiz et al. "Violation of Bell's inequality with quantum-dot single-photon sources". In: *Physical Review A* 106.1 (2022), p. 012222.

[32] Carlos FD Faurby et al. "Purifying photon indistinguishability through quantum interference". In: *Physical review letters* 133.3 (2024), p. 033604.

[33] Stefan Scheel. "Permanents in linear optical networks". In: *arXiv preprint quant-ph/0406127* (2004).

[34] Malte C Tichy. "Sampling of partially distinguishable bosons and the relation to the multidimensional permanent". In: *Physical Review A* 91.2 (2015), p. 022316.

[35] Albert Einstein, Boris Podolsky, and Nathan Rosen. "Can quantum-mechanical description of physical reality be considered complete?" In: *Physical review* 47.10 (1935), p. 777.

[36] John S Bell. "On the einstein podolsky rosen paradox". In: *Physics Physique Fizika* 1.3 (1964), p. 195.

[37] Yijian Meng et al. "Deterministic photon source of genuine three-qubit entanglement". In: *Nature Communications* 15.1 (2024), p. 7774.

[38] Hanna Le Jeannic et al. "Dynamical photon–photon interaction mediated by a quantum emitter". In: *Nature Physics* 18.10 (2022), pp. 1191–1195.

[39] Emanuel Knill, Raymond Laflamme, and Gerald J Milburn. "A scheme for efficient quantum computation with linear optics". In: *nature* 409.6816 (2001), pp. 46–52.

[40] Mathias JR Staunstrup et al. "Direct observation of a few-photon phase shift induced by a single quantum emitter in a waveguide". In: *Nature Communications* 15.1 (2024), p. 7583.

[41] Kasper H Nielsen et al. "Programmable Nonlinear Quantum Photonic Circuits". In: *arXiv preprint arXiv:2405.17941* (2024).

[42] Yijian Meng et al. "Photonic fusion of entangled resource states from a quantum emitter". In: *arXiv preprint arXiv:2312.09070* (2023).

[43] Robert Raussendorf and Hans J Briegel. "A one-way quantum computer". In: *Physical review letters* 86.22 (2001), p. 5188.

[44] Robert Raussendorf, Jim Harrington, and Kovid Goyal. "A fault-tolerant one-way quantum computer". In: *Annals of physics* 321.9 (2006), pp. 2242–2270.

[45] Daniel E. Browne and Terry Rudolph. "Resource-Efficient Linear Optical Quantum Computation". In: *Phys. Rev. Lett.* 95 (1 June 2005), p. 010501. DOI: 10.1103/PhysRevLett.95.010501. URL: https://link.aps.org/doi/10.1103/PhysRevLett.95.010501.

[46] Mercedes Gimeno-Segovia et al. "From Three-Photon Greenberger-Horne-Zeilinger States to Ballistic Universal Quantum Computation". In: *Phys. Rev. Lett.* 115 (2 July 2015), p. 020502. DOI: 10.1103/PhysRevLett.115.020502. URL: https://link.aps.org/doi/10.1103/PhysRevLett.115.020502.

[47] Hans J Briegel and Robert Raussendorf. "Persistent entanglement in arrays of interacting particles". In: *Physical Review Letters* 86.5 (2001), p. 910.

[48] Sara Bartolucci et al. "Fusion-based quantum computation". In: *Nature Communications* 14.1 (2023), p. 912.

[49] Dan Cogan et al. "Deterministic generation of indistinguishable photons in a cluster state". In: *Nature Photon.* 17.4 (Apr. 2023), pp. 324–329. DOI: 10.1038/s41566-022-01152-2. URL: https://www.nature.com/articles/s41566-022-01152-2 (visited on 04/13/2023).

[50] N. Coste et al. "High-rate entanglement between a semiconductor spin and indistinguishable photons". In: *Nature Photon.* 17 (Apr. 2023), pp. 582–587. DOI: 10.1038/s41566-023-01186-0. URL: https://www.nature.com/articles/s41566-023-01186-0.

[51] Philip Thomas et al. "Efficient generation of entangled multiphoton graph states from a single atom". In: *Nature* 608.7924 (Aug. 2022), pp. 677–681. ISSN: 1476-4687. DOI: 10.1038/s41586-022-04987-5. URL: https://www.nature.com/articles/s41586-022-04987-5.

[52] DA Gangloff et al. "Quantum interface of an electron and a nuclear ensemble". In: *Science* 364.6435 (2019), pp. 62–66.

[53] Thomas J. Bell, Love A. Pettersson, and Stefano Paesani. "Optimizing Graph Codes for Measurement-Based Loss Tolerance". In: *PRX Quantum* 4 (2 May 2023), p. 020328. DOI: 10.1103/PRXQuantum.4.020328. URL: https://link.aps.org/doi/10.1103/PRXQuantum.4.020328.

[54] Kaavya Sahay, Jahan Claes, and Shruti Puri. "Tailoring Fusion-Based Error Correction for High Thresholds to Biased Fusion Failures". In: *Phys. Rev. Lett.* 131 (12 Sept. 2023), p. 120604. DOI: 10.1103/PhysRevLett.131.120604. URL: https://link.aps.org/doi/10.1103/PhysRevLett.131.120604.

[55] Stefano Paesani and Benjamin J. Brown. "High-Threshold Quantum Computing by Fusing One-Dimensional Cluster States". In: *Phys. Rev. Lett.* 131 (12 Sept. 2023), p. 120603. DOI: 10.1103/PhysRevLett.131.120603. URL: https://link.aps.org/doi/10.1103/PhysRevLett.131.120603.

[56] Hector Bombin et al. "Fault-tolerant complexes". In: *arXiv preprint arXiv:2308.07844* (2023).

[57] Hector Bombin et al. "Interleaving: Modular architectures for fault-tolerant photonic quantum computing". In: *arXiv preprint arXiv:2103.08612* (2021).

[58] Marta Arcari et al. "Near-unity coupling efficiency of a quantum emitter to a photonic crystal waveguide". In: *Phys. Rev. Lett.* 113.9 (2014), p. 093603. URL: https://link.aps.org/doi/10.1103/PhysRevLett.113.093603.

[59] Netanel H Lindner and Terry Rudolph. "Proposal for pulsed on-demand sources of photonic cluster state strings". In: *Physical review letters* 103.11 (2009), p. 113602.

[60] Konstantin Tiurev et al. "High-fidelity multiphoton-entangled cluster state with solid-state quantum emitters in photonic nanostructures". In: *Phys. Rev. A* 105 (3 Mar. 2022), p. L030601. DOI: 10.1103/PhysRevA.105.L030601. URL: https://link.aps.org/doi/10.1103/PhysRevA.105.L030601.

[61] Martin Hayhurst Appel. "A Quantum Dot Source of Time-Bin Multi-Photon Entanglement". PhD thesis. University of Copenhagen, 2023. URL: https://nbi.ku.dk/english/theses/phd-theses/martin-hayhurst-appel/.

[62] Daniel Gottesman. *Stabilizer codes and quantum error correction*. California Institute of Technology, 1997.

[63] Sara Bartolucci et al. "Fusion-based quantum computation". In: *Nature Commun.* 14.1 (2023), p. 912. DOI: https://doi.org/10.1038/s41467-023-36493-1. URL: https://doi.org/10.1038/s41467-023-36493-1.

[64] Ying Wang et al. "Deterministic photon source interfaced with a programmable silicon-nitride integrated circuit". In: *npj Quantum Information* 9.1 (2023), p. 94.

[65] Jasper De Witte et al. "SiN/GaAs quantum photonic platform with efficient fiber-coupling". In: *Quantum 2.0*. Optica Publishing Group. 2024, QW3A–15.

[66] Chong-Ki Hong, Zhe-Yu Ou, and Leonard Mandel. "Measurement of subpicosecond time intervals between two photons by interference". In: *Physical review letters* 59.18 (1987), p. 2044.

[67] Peter Lodahl, Arne Ludwig, and Richard J Warburton. "A deterministic source of single photons". In: *Physics Today* 75.3 (2022), pp. 44–50.

[68] Igor Aharonovich, Dirk Englund, and Milos Toth. "Solid-state single-photon emitters". In: *Nature photonics* 10.10 (2016), pp. 631–641.

[69] E. Knill, R. T Laflamme, and G. J. Milburn. "A scheme for efficient quantum computation with linear optics". In: *Nature* 409 (2001), pp. 46–52.

[70] Han-Sen Zhong et al. "Quantum computational advantage using photons". In: *Science* 370.6523 (2020), pp. 1460–1463.

[71] Lars S Madsen et al. "Quantum computational advantage with a programmable photonic processor". In: *Nature* 606.7912 (2022), pp. 75–81.

[72] Stewart E Miller. "Integrated optics: An introduction". In: *The Bell system technical journal* 48.7 (1969), pp. 2059–2069.

[73] Osamu Wada, T Sakurai, and T Nakagami. "Recent progress in optoelectric integrated circuits (OEIC's)". In: *IEEE journal of quantum electronics* 22.6 (1986), pp. 805–821.

[74] Thomas L Koch and Uziel Koren. "Semiconductor photonic integrated circuits". In: *IEEE Journal of Quantum Electronics* 27.3 (1991), pp. 641–653.

[75] Wim Bogaerts et al. "Basic structures for photonic integrated circuits in silicon-on-insulator". In: *Optics Express* 12.8 (2004), pp. 1583–1591.

[76] Center for Research and Education in Optics and Lasers (CREOL). *Integrated Photonics Course*. Accessed: 2024-11-05. 2023. URL: `https://photonics.creol.ucf.edu/op-tec-resources/op-tec-course-materials/`.

[77] Ashish Chanana et al. "Ultra-low loss quantum photonic circuits integrated with single quantum emitters". In: *Nature Communications* 13.1 (2022), pp. 1–10.

[78] Caterina Taballione et al. "8× 8 reconfigurable quantum photonic processor based on silicon nitride waveguides". In: *Optics express* 27.19 (2019), pp. 26842–26857.

[79] Juan M Arrazola et al. "Quantum circuits with many photons on a programmable nanophotonic chip". In: *Nature* 591.7848 (2021), pp. 54–60.

[80] George K Celler and Sorin Cristoloveanu. "Frontiers of silicon-on-insulator". In: *Journal of Applied Physics* 93.9 (2003), pp. 4955–4978.

[81] Marcelo Davanco et al. "Heterogeneous integration for on-chip quantum photonic circuits with single quantum dot devices". In: *Nature communications* 8.1 (2017), pp. 1–12.

[82] Atefeh Shadmani et al. "Integration of GaAs waveguides on a silicon substrate for quantum photonic circuits". In: *Optics Express* 30.21 (2022), pp. 37595–37602.

[83] Alto Osada et al. "Strongly coupled single-quantum-dot–cavity system integrated on a CMOS-processed silicon photonic chip". In: *Physical Review Applied* 11.2 (2019), p. 024071.

[84] Noel H Wan et al. "Large-scale integration of artificial atoms in hybrid photonic circuits". In: *Nature* 583.7815 (2020), pp. 226–231.

[85] Jeremy C Adcock et al. "Programmable four-photon graph states on a silicon chip". In: *Nature Communications* 10.1 (2019), pp. 1–6.

[86] Malte C. Tichy et al. "Stringent and Efficient Assessment of Boson-Sampling Devices". In: *Phys. Rev. Lett.* 113 (2 July 2014), p. 020502. DOI: 10.1103/PhysRevLett.113.020502. URL: https://link.aps.org/doi/10.1103/PhysRevLett.113.020502.

[87] Andrea Crespi et al. "Suppression law of quantum states in a 3D photonic fast Fourier transform chip". In: *Nature Communications* 7.1 (2016), pp. 1–8.

[88] Stefano Paesani et al. "Scheme for Universal High-Dimensional Quantum Computation with Linear Optics". In: *Phys. Rev. Lett.* 126 (23 June 2021), p. 230504. DOI: 10.1103/PhysRevLett.126.230504. URL: https://link.aps.org/doi/10.1103/PhysRevLett.126.230504.

[89] Davide Bacco et al. "Proposal for practical multidimensional quantum networks". In: *Physical Review A* 104.5 (2021), p. 052618.

[90] Jeffrey Marshall. "Distillation of Indistinguishable Photons". In: *Phys. Rev. Lett.* 129 (21 Nov. 2022), p. 213601. DOI: 10.1103/PhysRevLett.129.213601. URL: https://link.aps.org/doi/10.1103/PhysRevLett.129.213601.

[91] Thomas J Bell et al. "Protocol for generation of high-dimensional entanglement from an array of non-interacting photon emitters". In: *New Journal of Physics* 24.1 (2022), p. 013032.

[92] Arne Ludwig et al. "Ultra-low charge and spin noise in self-assembled quantum dots". In: *Journal of Crystal Growth* 477 (2017), pp. 193–196.

[93] Matthias C Löbl et al. "Excitons in InGaAs quantum dots without electron wetting layer states". In: *Communications Physics* 2.1 (2019), pp. 1–7.

[94] Alisa Javadi et al. "Numerical modeling of the coupling efficiency of single quantum emitters in photonic-crystal waveguides". In: *JOSA B* 35.3 (2018), pp. 514–522.

[95] Leonardo Midolo et al. "Soft-mask fabrication of gallium arsenide nanomembranes for integrated quantum photonics". In: *Nanotechnology* 26.48 (2015), p. 484002.

[96] Simon M Sze, Yiming Li, and Kwok K Ng. *Physics of semiconductor devices*. John wiley & sons, 2021.

[97] Anna Peczek et al. "Comparison of cut-back method and optical backscatter reflectometry for wafer level waveguide characterization". In: *2020 IEEE 33rd International Conference on Microelectronic Test Structures (ICMTS)*. 2020, pp. 1–3. DOI: 10.1109/ICMTS48187.2020.9107905.

[98] T. C. Ralph et al. "Linear optical controlled-NOT gate in the coincidence basis". In: *Phys. Rev. A* 65 (6 June 2002), p. 062324. DOI: 10.1103/PhysRevA.65.062324. URL: https://link.aps.org/doi/10.1103/PhysRevA.65.062324.

[99] Mathias Pont et al. "High-fidelity generation of four-photon GHZ states on-chip". In: *arXiv preprint. arXiv:2211.15626* (2022). DOI: 10.48550/ARXIV.2211.15626. URL: https://arxiv.org/abs/2211.15626.

[100] Andreas Fyrillas et al. "Certified randomness in tight space". In: *arXiv preprint arXiv:2301.03536* (2023).

[101] Daniel F. V. James et al. "Measurement of qubits". In: *Phys. Rev. A* 64 (5 Oct. 2001), p. 052312. DOI: 10.1103/PhysRevA.64.052312. URL: https://link.aps.org/doi/10.1103/PhysRevA.64.052312.

[102] Koen Alexander et al. "A manufacturable platform for photonic quantum computing". In: *arXiv preprint arXiv:2404.17570* (2024).

[103] Si Chen et al. "Heralded Three-Photon Entanglement from a Single-Photon Source on a Photonic Chip". In: *Phys. Rev. Lett.* 132 (13 Mar. 2024), p. 130603. DOI: 10.1103/PhysRevLett.132.130603. URL: https://link.aps.org/doi/10.1103/PhysRevLett.132.130603.

[104] Nicolas Maring et al. "A versatile single-photon-based quantum computing platform". In: *Nature Photonics* 18.6 (2024), pp. 603–609.

[105] Leonard Mandel. "Coherence and indistinguishability". In: *Optics letters* 16.23 (1991), pp. 1882–1883.

[106] Jeremy L O'brien. "Optical quantum computing". In: *Science* 318.5856 (2007), pp. 1567–1570.

[107] Andreas V Kuhlmann et al. "Charge noise and spin noise in a semiconductor quantum device". In: *Nature Physics* 9.9 (2013), pp. 570–575.

[108] Patrik I Sund et al. "High-speed thin-film lithium niobate quantum processor driven by a solid-state quantum emitter". In: *Science Advances* 9.19 (2023), eadg7268.

[109] Lorenzo Carosini et al. "Programmable multiphoton quantum interference in a single spatial mode". In: *Science Advances* 10.16 (2024), eadj0993. DOI: 10.1126/sciadv.adj0993. eprint: https://www.science.org/doi/pdf/10.1126/sciadv.adj0993. URL: https://www.science.org/doi/abs/10.1126/sciadv.adj0993.

[110] Patrik I. Sund et al. "Hardware requirements for realizing a quantum advantage with deterministic single-photon sources". In: *Phys. Rev. A* 109 (4 Apr. 2024), p. 042613. DOI: 10.1103/PhysRevA.109.042613. URL: https://link.aps.org/doi/10.1103/PhysRevA.109.042613.

[111] Petru Tighineanu et al. "Phonon decoherence of quantum dots in photonic structures: Broadening of the zero-phonon line and the role of dimensionality". In: *Physical Review Letters* 120.25 (2018), p. 257401.

[112] Christopher Sparrow. "Quantum interference in universal linear optical devices for quantum computation and simulation". In: *Ph.D. thesis, Imperial College London* (2017).

[113] Jeffrey Marshall. "Distillation of Indistinguishable Photons". In: *Physical Review Letters* 129.21 (2022), p. 213601.

[114] Charles H Bennett et al. "Purification of noisy entanglement and faithful teleportation via noisy channels". In: *Physical review letters* 76.5 (1996), p. 722.

[115] Sergey Bravyi and Alexei Kitaev. "Universal quantum computation with ideal Clifford gates and noisy ancillas". In: *Physical Review A* 71.2 (2005), p. 022316.

[116] Evan Meyer-Scott, Christine Silberhorn, and Alan Migdall. "Single-photon sources: Approaching the ideal through multiplexing". In: *Review of Scientific Instruments* 91.4 (2020), p. 041101.

[117] Andrew Villadsen. *Photon purification via interference*. `https://sid.erda.dk/share_redirect/aHpmpq3psC`. Bachelor thesis. 2023.

[118] Michal Vyvlecka et al. "Robust excitation of C-band quantum dots for quantum communication". In: *Applied Physics Letters* 123.17 (2023).

[119] H Ollivier et al. "Hong-Ou-Mandel interference with imperfect single photon sources". In: *Physical Review Letters* 126.6 (2021), p. 063602.

[120] Jason Saied et al. "General protocols for the efficient distillation of indistinguishable photons". In: *arXiv preprint arXiv:2404.14217* (2024).

[121] FHB Somhorst et al. "Photon distillation schemes with reduced resource costs based on multiphoton Fourier interference". In: *arXiv preprint arXiv:2404.14262* (2024).

[122] Freja T Pedersen et al. "Near transform-limited quantum dot linewidths in a broadband photonic crystal waveguide". In: *ACS Photonics* 7.9 (2020), pp. 2343–2349.

[123] Francesco Lenzini et al. "Active demultiplexing of single photons from a solid-state source". In: *Laser & Photonics Reviews* 11.3 (2017), p. 1600297.

[124] J Ignacio Cirac and Peter Zoller. "Goals and opportunities in quantum simulation". In: *Nature physics* 8.4 (2012), pp. 264–266.

[125] Ehud Altman et al. "Quantum simulators: Architectures and opportunities". In: *PRX quantum* 2.1 (2021), p. 017003.

[126] Ryan Babbush et al. "Exponential quantum speedup in simulating coupled classical oscillators". In: *Physical Review X* 13.4 (2023), p. 041041.

[127] Hidetoshi Nishimori. *Statistical physics of spin glasses and information processing: an introduction*. 111. Clarendon Press, 2001.

[128] Hubert Ramsauer et al. "Hopfield networks is all you need". In: *arXiv preprint arXiv:2008.02217* (2020).

[129] John A Hertz. *Introduction to the theory of neural computation*. Crc Press, 2018.

[130] Yunhong Ding et al. "Reconfigurable SDM switching using novel silicon photonic integrated circuit". In: *Scientific Reports* 6.1 (2016), p. 39058.

[131] William R Clements et al. "Optimal design for universal multiport interferometers". In: *Optica* 3.12 (2016), pp. 1460–1465.

[132] Beatrice Da Lio et al. "A pure and indistinguishable single-photon source at telecommunication wavelength". In: *Advanced Quantum Technologies* 5.5 (2022), p. 2200006.

[133] Carlos F.D. Faurby. "Frequency Conversion of Single Photons for Long Distance Quantum Communication". Accessed: 2024-11-05. MA thesis. Niels Bohr Institute, University of Copenhagen, 2021. URL: `https://nbi.ku.dk/english/theses/masters-theses/carlos-fernando-duarte-faurby/`.

[134] Love A Pettersson, Anders S Sørensen, and Stefano Paesani. "Deterministic generation of concatenated graph codes from quantum emitters". In: *arXiv preprint arXiv:2406.16684* (2024).

[135] Ming Lai Chan et al. "Tailoring fusion-based photonic quantum computing schemes to quantum emitters". In: *arXiv preprint arXiv:2410.06784* (2024).